TECHNISCHE
UNIVERSITÄT
WIEN
Vienna University of Technology

MEDIZINISCHE
UNIVERSITÄT
WIEN

DISSERTATION

Determination of the Total Retinal Blood Flow Using Fourier-Domain Optical Coherence Tomography and Fundus Imaging

ausgeführt zum Zwecke der Erlangung des akademischen Grades einer
Doktorin der technischen Wissenschaften
unter der Leitung von

Ao.Univ.-Prof. DI Dr. Martin Gröschl

E134 Institut für Angewandte Physik
Technische Universität Wien

und

Ao.Univ.-Prof. DI Dr. Leopold Schmetterer
Ass.-Prof. DI(FH) René Werkmeister, PhD

Zentrum für med. Physik und biomed. Technik
Medizinische Universität Wien

eingereicht an der
Technischen Universität Wien
Fakultät für Physik

von

Dipl.-Ing. Mag. Veronika Doblhoff-Dier

e0326076
Jägerstraße 69/1/12
A-1200 Wien

Wien, im Dezember 2014

Abstract

Optical coherence tomography (OCT) is an interferometric method for the analysis of refractive media. The expansion of this technique to *Doppler OCT* allows the measurement of velocities via the Doppler effect.

This work describes the development and application of a novel dual beam Doppler Fourier domain optical coherence tomography system for the measurement of the total retinal blood flow. Blood flow measurements are of interest for medical reasons: a number of ocular diseases can be correlated with changes of the retinal perfusion.

The presented system differs from previous systems in that it has two orthogonal detection planes, allowing to record the blood flow in vessels with arbitrary orientations. Moreover, a commercially available Dynamic Vessel Analyzer, yielding precise data on the vessel diameter, was included in the system. Thus, the blood flow can be measured in absolute values.

The absolute blood flow values reported in this work lie within the range of values reported in literature. Moreover, the results reported in this thesis show a high degree of conformity between the flow in the arteries and veins, which further corroborates the measurements' validity.

The system is capable of measuring the arterial as well as the venous flow in vessels with diameters down to about $30\,\mu m$. Thus, it is possible to measure the dependence of the flow on the vessel diameter for a very large range of values. For vessels with diameters of above $\sim 60\,\mu m$, these measurements yield a log-log correlation coefficient close to three, which would be expected according to Murray's law. For smaller diameters, however, a clear divergence from this relationship can be found.

Owing to the high measurement sensitivity, the large possible measurement range, and the reliable results, the system has a high potential to be of use in the investigation of ocular perfusion. Thus, it may further our understanding of ocular diseases which go hand in hand with changes in the retinal blood flow.

Kurzfassung

Optische Kohärenztomografie (OCT) ist ein interferometrisches Untersuchungsverfahren zur Messung streuender Medien. Die Erweiterung der Technik zur *Doppler optischen Kohärenztomografie* ermöglicht es, mithilfe des Dopplereffektes auch Geschwindigkeitsmessungen durchzuführen.

Die vorliegende Arbeit beschreibt die Entwicklung und Anwendung eines neuen, zweistrahligen Doppler OCT-Systems im Fourier-Regime zur Messung des totalen Blutflusses im menschlichen Auge. Dies ist von großem Interesse, da eine Reihe von Augenkrankheiten mit Veränderungen des Blutflusses einhergehen.

Das System weist im Vergleich zu bereits bekannten Systemen eine Reihe von Neuerungen auf: Zur Messung des Blutflusses in Gefäßen mit beliebiger Ausrichtung ist es mit zwei orthogonalen Detektionsebenen ausgestattet. Weiters ist in dem System ein kommerziell erhältliches Gerät zur dynamischen Gefäßerkennung integriert. Dieses ermöglicht die genaue Messung der Gefäßdurchmesser und erlaubt dadurch die Bestimmung absoluter Blutflusswerte.

Die Messergebnisse, die in dieser Arbeit präsentiert werden, liegen im Bereich bisher veröffentlichter Werte des okularen Gesamtblutflusses. Ein Indikator für die Korrektheit der Messungen ist weiters, dass das Gerät es erlaubt, Flusswerte sowohl in Venen als auch in Arterien zu bestimmen. Da das Auge ein Endorgan ist, muss der arterielle Fluss dem venösen Fluss entsprechen. Die gute Übereinstimmung der Flusswerte der beiden Gefäßarten deutet auf eine hohe Validität der Messungen hin.

Mit dem entwickelten Gerät ist es möglich, den Blutfluss in Gefäßen mit Durchmessern ab etwa 30 µm zu messen. Dieser große Messumfang erlaubt eine Analyse des Zusammenhanges von Blutfluss und Gefäßdurchmesser über einen weiten Bereich. Dies ermöglicht die Überprüfung des Gesetzes von Murray, das für den log-log Regressionskoeffizienten zwischen Fluss und Gefäßdurchmesser einen Wert von 3 vorhersagt. Für Gefäßdurchmesser über etwa 60 µm konnte eine gute Übereinstimmung der Werte mit den von Murrays Gesetz vorhergesagten Werten belegt werden. Für kleinere Gefäßdurchmesser wurde jedoch eine deutliche Abweichung von diesem Wert nachgewiesen.

Die hohe Messgenauigkeit, der große Messbereich und die vorliegenden Messdaten deuten auf ein hohes Potential des Systems zur Untersuchung des okularen Blutflusses im Allgemeinen sowie seiner krankhaften Veränderung im Speziellen hin. Der hier beschriebene Aufbau erscheint daher geeignet, um in Zukunft einen Beitrag zur Früherkennung und rechtzeitigen Behandlung von Augenerkrankungen zu leisten.

Acknowledgements

*It is what difference we have made
to the lives of others that will
determine the significance of the
life we lead.*

Nelson Mandela

In the years of working on this dissertation, a number of people made a difference to my life. Without them, these years would not have been the same and this work could not have been done. A heartfelt *thank you* goes to all who shared my path and helped me along. To some of you, I would like to extend special thanks:

First of all, I would like to express my sincere gratitude towards my two supervisors, Leopold Schmetterer and Martin Gröschl.

Dear Leo, I cannot thank you enough for all you have done: for offering me this position and becoming my supervisor; for allowing me to be part of your exciting, well-funded, interdisciplinary group of physicists and medical doctors that gives all our scientific work the practical grounding; for creating an organisational structure which ensures that we PhDs always had someone to turn to with our problems. We know that we owe all this to your constant and devoted work for the group. Thank you ever so much for letting me be part of this team and for all your advice and support!

Dear Martin, thank you for getting me started on this fantastic topic! Thank you for all the encouragement along the way, for all your help in organisational and practical matters and for the hilarious e-mails you sent on perfectly serious topics - you were a great help and also always ready to make us laugh. It was very reassuring to know you would support us in any way you could.

My sincerest thanks go to my supervising colleague, René Werkmeister.

Dear René, it is difficult to express the extent of my gratitude to you. Probably the closest to what I would like to express is: thank you for everything. I'm

quite sure you don't know *how* important you were and are for all of us PhDs. Whenever there was any problem we could not solve together, we could count on you to have an idea and point us in the right direction. In all on the years I worked on my PhD, you always found time for me when I needed it. I don't know how you manage to work so much, sleep so little and still be so great a colleague and co-supervisor, but you certainly are. I learned so much from you; without you, this thesis would never have been written. Thank you so much!

Many colleagues were an important part of my life and became close friends. Some of them I would like to thank personally. The first amongst these are my fellow PhDs and lab mates, Gerold Aschinger and Martin Vietauer.

Dear Gerold, thank you for sharing my system, my problems, my deliberations, my lunch breaks and everything else that we were able to do together after you had started your thesis on my – and now on our – system. The number of times that one of us helped the other with adjustments, calculations and measurements, improved the other's ideas and lent a helping hand where the own hands were not sufficient cannot be counted. Working with you was a pleasure. Your calm way, your pleasant attitude and your skills were indispensable. Thank you for sharing so many hours with me and becoming much more than a colleague: my friend.

Dear Martin, life would have been much more boring without you... You opened a whole new world of heavy metal, stupid comics and funny anecdotes for me. Furthermore, you were always there for fruitful discussions on our work: you offered your help whenever I needed it, and gratefully accepted ideas and advice when I could give any. Working with you was great fun and of great worth, thank you so much. And thank you, too, for sharing not only professional interests but also creating a stable friendship that will hopefully continue far into the future.

I made many friends at the institute. They were part of my life for these years and helped make them the wonderful experience which they were. Amongst others, these were Franz Felberer, Sophie Caujolle and Iris Schmidt, Jutta Hyee and Andi Hodul.

Dear Franz, thank you for agitated discussions on topics nobody knew anything about, and for solutions to saving the world in practically every lunch break. Thank you for all your advice and help with my work, too. I am glad to be your friend.

Chère Sophie, travailler avec toi, pratiquer le Français avec toi et partager ton étonnement et ta joie en découvrant la vie Viennoise avec ses bals, son Kaiserschmarrn et ses habitants était un vrai plaisir ! Merci pour tout !

Dear Andi, the workshop wouldn't be the same without you: thank you for manufacturing so many vital parts of my setup, for offering ideas on how to best solve constructional and practical problems, for lending me screwdrivers, bolts,

completely useless advice and whatever else was needed. Thank you for confiding in me, for all the chats and teasing, and for all your help.

Dear Jutta, thank you for all your patience and help with organisational matters, and for caring for our personal and cultural advancement by organising trips to theatres, baking cakes and being such a nice person.

Many others shared all or part of my way with me and were wonderful colleagues. Amongst them are the scientists Iris Schmidt, Daniel Fechtig, Bernhard Baumann, Michael Pircher, Michael Bronhagl, Jozsef Klaizer, Corinna Knopf, Robert Klaus, Valentin Aranha dos Santos, Teresa Torzicky and others; our medical team including Magdalena Wirth, Carina Baar, Reinhard Told, Agnes Boltz, Alexandra Rauch and Doreen Schmidl, the staff at the ZMPBMT, including Melitta Pichler, Sigi Gollubits, Harald Sattmann, Angela Taubeck and many more. Thank you all.

A thank you also goes to my 'lab humans' who lent me their time and eyes to test my setup.

Dear Reinhard, Agnes, Valentin and Martin, and all the others: a special thank you for your patience and collaboration! It is greatly valued.

I would also like to thank all of my 'pre-doc-friends', whom I have known for a long time:

Thank you all for patiently listening to me talking about my setup for hours on end, for spending time together and for being there whenever I need you (and also when I don't need you but just enjoy having you around). You are the best possible group of friends!

A special thank you goes to my family, especially to my parents Nicolette and Georg Doblhoff-Dier and my sister Katharina.

Dear Mami, dear Papa! You have made me what I am today, you shared my worries and my joys and loved me all my life. You were and are always proud of me, however small the occasion. So much of what is me today I owe to you: in a way, this thesis is also your achievement. Thank you for everything.

Dear Katharina, you are my very favourite sister; I couldn't imagine a better one. Thank you for all your advice and for deserving and returning the complete trust we place in each other.

Lastly, I want to thank Stefan Löffler:

Dear Stefan, you were at my side all along: you helped me with seemingly unsolvable computer and programming problems, took a real interest in my work and spent hours proofreading my thesis in the most minute detail. Besides, you are the star at my side, lighting the way. Thank you.

Contents

List of figures

List of tables

List of abbreviations

BD   beam displacer

BS   beam splitter

CCD   charge-coupled device (camera)

CRA   central retinal artery

CRV   central retinal vein

DOF   depth of focus

DSNU   dark signal non-uniformity

DVA   Dynamic Vessel Analyzer

dpt   diopters; $1\,\mathrm{dpt} = 1\,\mathrm{m}^{-1}$

FC   fiber collimator

FDOCT   Fourier domain optical coherence tomography

FFT   fast Fourier transform

FT   Fourier transform

LED   light emiting diode

LDV   laser Doppler velocimetry

MPE   maximum permissible exposure

OCT   optical coherence tomography

OD   oculus dexter, i.e. the right eye

ONH   optic nerve head

OF   oversampling factor

OI	optical isolator
PC	polarization controller
PBS	polarizing beam splitter
RBC	red blood cell
RIO	Reconfigurable I/O
ROI	region of interest
Sc	scanner
SLD	superluminescent diode
SNR	signal-to-noise ratio
TDOCT	time domain optical coherence tomography

Chapter 1

Introduction

A number of common ocular diseases causing blindness, such as diabetic retinopathy [1–3], macular degeneration [4, 5], and glaucoma [6, 7] also change the retinal perfusion, i.e. the blood flow in the eye. Likewise, cardiovascular diseases (including stroke) [8, 9], atherosclerosis [10], and a number of other medical conditions [11] may be associated with abnormalities in the blood flow. Chen and Zhang [12], for example, mention these problems and underline the necessity of research in this area:

> In ophthalmology, many ophthalmic diseases may involve disturbances in ocular blood flow, including diabetic retinopathy, low tension glaucoma, anterior ischemic optic neuritis, and macular degeneration. For example, in diabetic retinopathy, retinal blood flow is reduced and the normal autoregulatory capacity is deficient. Ocular hemodynamics is altered in patients with glaucoma, and severe loss of visual function has been associated with reduced macular blood flow. Simultaneous imaging of tissue structure and blood flow could provide critical information for early diagnosis of ocular diseases.

Thus, the recent years have seen increased attention devoted to the development of non-invasive blood flow quantification techniques. Due to the eye's light-transmitting properties (which are, of course, functionally necessary), optical methods lend themselves perfectly to this cause. Several different methods were proposed and widely used in the past, including laser Doppler velocimetry (e.g. [13–16]) and

15

fluorescein angiography (e.g. [17–19]). More recently, Doppler optical coherence tomography (OCT) has become increasingly prominent in ophthalmology. Basically, OCT is a technique for acquiring images of the structure of scattering media, based on the principle of interferometry. In the last few years, it has been established as a fast, non-invasive and reliable method to measure ocular blood flow [12].

The aim of this work was to build an OCT system to measure the *total* retinal blood flow. The measurement technique used to this end is dual beam Doppler Fourier domain optical coherence tomography. This technique will be explained in more detail in the following, but a short overview to motivate the thesis' long title shall be given here: the measurements were performed with a specific type of OCT system, namely a Fourier domain OCT (FDOCT), allowing a fast acquisition of OCT images using a broadband light source (see section 2.2). Velocities were measured via the Doppler effect (known to most people from the changing pitch of a passing fire engine horn), which explains the fact that the frequency of waves changes if the source is moving relative to the detector (see section 2.3). Additionally, *two* light beams were used simultaneously in the measurements (hence the term 'dual beam'). This fact allows eliminating one unknown parameter which has to be estimated when using only one beam (see section 2.3.2).

Clearly, this is only the briefest possible explanation of a very potent measurement technique. For further details, the reader is cordially invited to proceed to the main part of this thesis.

Chapter 2

Principles of optical coherence tomography

> *It's a theory and a theory can do no harm.*
>
> Peter Ackroyd

2.1 Basics of OCT

OCT is a contactless optical imaging modality used to measure depth profiles inside scattering media. Information from the inside of a sample (e.g. the human eye) can thus be acquired non-invasively.

2.1.1 The Michelson interferometer

The basis of OCT is the Michelson interferometer (Fig. 2.1): a beam from a light source is split into two by a semi-transparent mirror. One part enters the so-called 'sample arm' and is reflected from one or more layers at distances z_{S_n} in a sample, the other part is reflected from a mirror at a known reference position z_R in the 'reference arm'. Subsequently, the two beams are reunited back at the semi-transparent mirror and measured at a detector.

A more thorough mathematical description will be given in section 2.1.2, but the basic idea is this: if the optical path length difference between both arms is smaller than the coherence length of the beam, interference will take place, resulting in an
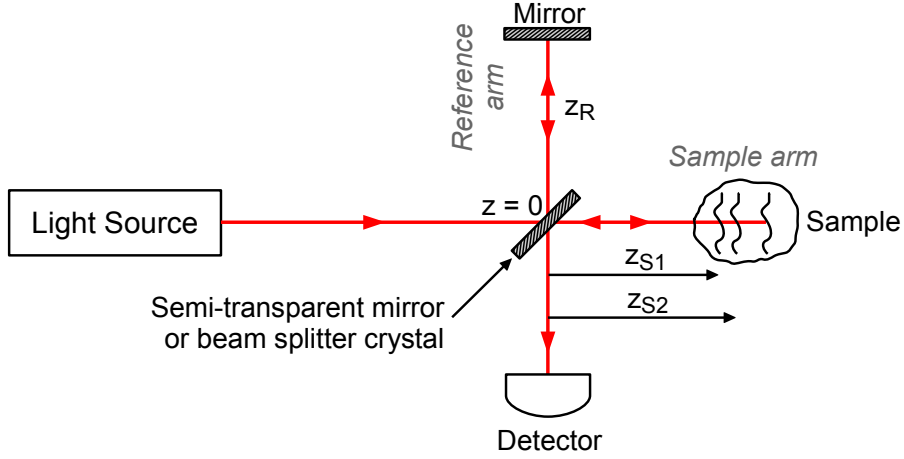
Figure 2.1: Schematic drawing of a Michelson interferometer (adapted from Izatt and Choma [20]).

intensity I_D at the detector given by

$$I_D \propto |E_R|^2 + |E_S|^2 + 2E_R E_S \cos(2k\Delta L). \tag{2.1}$$

Here, $|E_R|^2$ and $|E_S|^2$ are the intensities one would get *without* any interference from the reference arm and the sample arm, respectively; the last term is due to the interference of the two beams. As can be seen in Eq. 2.1, the interference term depends on the path length difference $\Delta L = 2z_R - 2z_S$ between sample arm and reference arm (the factor 2 is due to the light having to pass through the interferometer's arms twice, once on its way in and once its way out). If the length of the reference arm is known, measuring the interference allows inferring the distance of the reflecting layers in the sample arm.

2.1.2 Mathematical description of OCT

A mathematical discussion of OCT can be found in Izatt and Choma [20] – an explanation of the basic concept along those lines will be given in the following.

Consider the Michelson interferometer shown in Fig. 2.2: the incident beam has an electric field E_i

$$E_i = s(k,\omega)\mathrm{e}^{i(kz-\omega t)}, \tag{2.2}$$

with an amplitude $s(k,\omega)$ and a phase $(kz - \omega t)$, where k is the wave vector, z is the spacial coordinate, ω is the angular frequency and t is the temporal coordinate. The beam's intensity, which can be measured, is the square of the absolute value of the electric field:

$$I(k,\omega) = |E_i|^2. \tag{2.3}$$
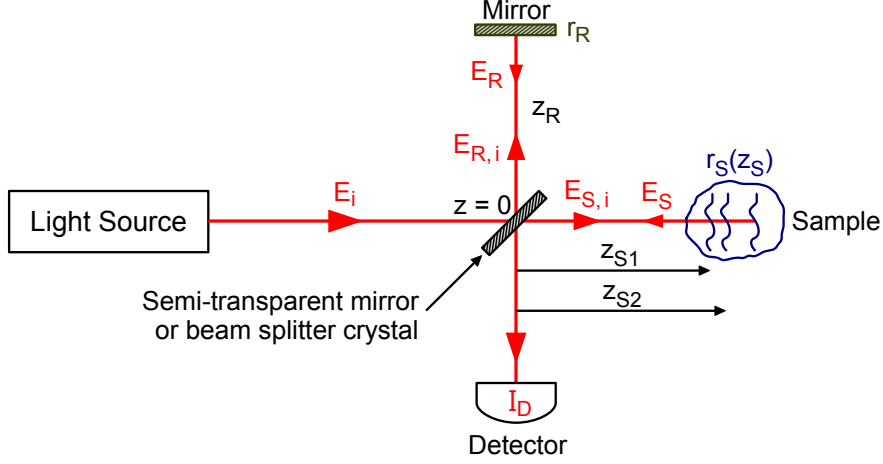
Figure 2.2: Electric fields in the Michelson interferometer (adapted from [20]). Definitions of the variables are given in the text.

When it reaches the semi-transparent mirror at $z = 0$, the beam is split into two parts, both with an intensity of $I(k, \omega)/2 = |E_i/\sqrt{2}|^2$. The electric fields of the beams entering each of the interferometer's arms can thus be written as

$$E_{R,i} = E_{S,i} = \frac{s(k, \omega)}{\sqrt{2}} e^{i(kz - \omega t)}. \tag{2.4}$$

The beam in the reference arm is reflected from the reference mirror at a distance z_R, which has a reflectivity of r_R. For the field E_R of the reflected beam (moving in direction $-k$), one can make the ansatz

$$E_R = \frac{s(k, \omega)}{\sqrt{2}} \cdot r_R \cdot e^{i(-kz - \omega t + \phi_R)}. \tag{2.5}$$

Thereby, ϕ_R is the additional phase accumulated by the beam on its way through the reference arm (i.e. on its way to the mirror, during the reflection and back from the mirror). To determine the phase ϕ_R, one can make use of the fact that the incident wave and the reflected wave have to be identical at the mirror except for an additional phase π (as the reflection at the reference mirror is a reflection at a fixed boundary) and the factor r_R by which the reflected beam's amplitude is lowered. Hence,

$$E_{R,i}(z_R) = \frac{E_R(z_R) \cdot e^{i\pi}}{r_R}$$
$$e^{i(kz_R - \omega t)} = e^{i(-kz_R - \omega t + \phi_R + \pi)} \tag{2.6}$$
$$\phi_R = 2kz_R - \pi.$$

Thus, the field of the reflected reference beam is

$$E_R = \frac{s(k, \omega)}{\sqrt{2}} \cdot r_R \cdot e^{i(-kz - \omega t + 2kz_R - \pi)}. \tag{2.7}$$

19

A similar relation holds true for the sample arm, except that the beam is, in this case, not reflected at a mirror but at the sample. For the sake of simplicity, the sample is assumed to contain several discrete reflecting layers[i] at depths z_{S_n}. The sample's reflectivity is thus $r_S(z_S) = \sum_n r_{S_n}\delta(z_S - z_{S_n})$. In analogy to Eq. 2.7, the field of the reflected sample arm beam is

$$
\begin{aligned}
E_S &= \frac{s(k,\omega)}{\sqrt{2}}\int r_S(z_S) \cdot \mathrm{e}^{i(-kz-\omega t+2kz_S-\pi)}\mathrm{d}z_S \\
&= \frac{s(k,\omega)}{\sqrt{2}}\sum_n r_{S_n}\mathrm{e}^{i(-kz-\omega t+2kz_{S_n}-\pi)}.
\end{aligned}
\tag{2.8}
$$

The beams from the sample arm and the reference arm are reunited at the semi-transparent mirror; *half* of the intensity is transmitted through the mirror in direction of the detector. The detector response will be termed ρ. As the rate of detection is, for any practical detector, much smaller than the frequency ω,[ii] the detector effectively gives a time-average; this will be denoted by $\langle\ \rangle$. The intensity measured at the detector is thus

$$
I_D(k,\omega) = \frac{\rho}{2}\langle|E_R + E_S|^2\rangle.
\tag{2.9}
$$

With Eq. 2.7 and Eq. 2.8, this results in

$$
\begin{aligned}
I_D(k,\omega) &= \frac{\rho}{2}\langle|E_R + E_S|^2\rangle \\
&= \frac{\rho}{2}\left\langle\left|\frac{s(k,\omega)}{\sqrt{2}}r_R\mathrm{e}^{i(-kz-\omega t+2kz_R-\pi)} + \frac{s(k,\omega)}{\sqrt{2}}\sum_n r_{S_n}\mathrm{e}^{i(-kz-\omega t+2kz_{S_n}-\pi)}\right|^2\right\rangle.
\end{aligned}
\tag{2.10}
$$

Considering that $|a\cdot b|^2 = |a|^2 \cdot |b|^2$, the equation can be rearranged to

$$
I_D(k,\omega) = \frac{\rho}{2}\left\langle\left|\frac{s(k,\omega)}{\sqrt{2}}\right|^2 \cdot \left|\mathrm{e}^{i(-kz-\omega t-\pi)}\right|^2 \cdot \left|r_R\mathrm{e}^{2ikz_R} + \sum_n r_{S_n}\mathrm{e}^{2ikz_{S_n}}\right|^2\right\rangle.
\tag{2.11}
$$

As $|\mathrm{e}^{ix}|^2 = \mathrm{e}^{ix} \cdot \mathrm{e}^{-ix} = 1$, this equation can be simplified to

$$
I_D(k,\omega) = \frac{\rho}{2}\left\langle\left|\frac{s(k,\omega)}{\sqrt{2}}\right|^2 \cdot \left|r_R\mathrm{e}^{2ikz_R} + \sum_n r_{S_n}\mathrm{e}^{2ikz_{S_n}}\right|^2\right\rangle.
\tag{2.12}
$$

The last term of Eq. 2.12 is time-independent. Consequently, it can be excluded from the time average:

$$
I_D(k,\omega) = \frac{\rho}{2}\left\langle\left|\frac{s(k,\omega)}{\sqrt{2}}\right|^2\right\rangle \cdot \left|r_R\mathrm{e}^{2ikz_R} + \sum_n r_{S_n}\mathrm{e}^{2ikz_{S_n}}\right|^2.
\tag{2.13}
$$

---

[i]The layers are assumed to be weakly scattering and absorption is neglected, so that the incident field can be approximated as $E_{S,i}$ for all of the layers.

[ii]In this work, for example, the rate of detection was in the range of µs, while the light's oscillation period was only several femtoseconds.

The time-averaged squared amplitude $S(k) = \langle |s(k,\omega)|^2 \rangle$ is called *light source spectrum*. Thus, the equation can be rewritten as

$$I_D(k) = \frac{\rho}{4} \, S(k) \cdot \left| r_R \mathrm{e}^{2ikz_R} + \sum_n r_{S_n} \mathrm{e}^{2ikz_{S_n}} \right|^2, \tag{2.14}$$

or

$$I_D(k) = \frac{\rho}{4} \, S(k) \cdot \left[\left(r_R \mathrm{e}^{2ikz_R} + \sum_n r_{S_n} \mathrm{e}^{2ikz_{S_n}} \right) \cdot \left(r_R \mathrm{e}^{-2ikz_R} + \sum_n r_{S_n} \mathrm{e}^{-2ikz_{S_n}} \right) \right]. \tag{2.15}$$

Expanding the multiplication yields

$$I_D(k) = \frac{\rho}{4} \, S(k) \cdot \left[r_R{}^2 + \sum_n r_R r_{S_n} \mathrm{e}^{2ik(z_R - z_{S_n})} + \sum_n r_R r_{S_n} \mathrm{e}^{2ik(z_{S_n} - z_R)} + \right.$$
$$\left. + \sum_n \sum_m r_{S_n} r_{S_m} \mathrm{e}^{2ik(z_{S_n} - z_{S_m})} \right]. \tag{2.16}$$

The double sum over n and m can be split into one part containing only the summands for which $n = m$, one for which $n < m$, and one for which $n > m$. This leads to

$$I_D(k) = \frac{\rho}{4} \, S(k) \cdot \left[r_R{}^2 + \sum_n r_R r_{S_n} \left(\mathrm{e}^{2ik(z_R - z_{S_n})} + \mathrm{e}^{-2ik(z_R - z_{S_n})} \right) + \right.$$
$$\left. + \sum_n r_{S_n}{}^2 + \sum_{n<m} r_{S_n} r_{S_m} \mathrm{e}^{2ik(z_{S_n} - z_{S_m})} + \sum_{n>m} r_{S_n} r_{S_m} \mathrm{e}^{2ik(z_{S_n} - z_{S_m})} \right]. \tag{2.17}$$

Considering that

$$\sum_{n>m} \mathrm{e}^{2ik(z_{S_n} - z_{S_m})} = \sum_{n<m} \mathrm{e}^{-2ik(z_{S_n} - z_{S_m})} \; \forall n, m, \tag{2.18}$$

and using the power reflectivity $R = |r|^2$, $I_D(k)$ can be written as

$$I_D(k) = \frac{\rho}{4} \, S(k) \cdot \left[\left(R_R + \sum_n R_{S_n} \right) + \right.$$
$$+ \sum_n \sqrt{R_R R_{S_n}} \left(\mathrm{e}^{2ik(z_R - z_{S_n})} + \mathrm{e}^{-2ik(z_R - z_{S_n})} \right) +$$
$$\left. + \sum_{n<m} \sqrt{R_{S_n} R_{S_m}} \left(\mathrm{e}^{2ik(z_{S_n} - z_{S_m})} + \mathrm{e}^{-2ik(z_{S_n} - z_{S_m})} \right) \right]. \tag{2.19}$$

With the decomposition

$$\cos x = \frac{\mathrm{e}^{ix} + \mathrm{e}^{-ix}}{2} \qquad \Leftrightarrow \qquad \mathrm{e}^{ix} + \mathrm{e}^{-ix} = 2\cos x \tag{2.20}$$

the detected intensity $I_D(k)$ can be written as

$$I_D(k) = \frac{\rho}{4}S(k) \cdot \left(R_R + \sum_n R_{S_n}\right) +$$
$$+ \frac{\rho}{4}S(k) \cdot 2 \cdot \sum_n \sqrt{R_R R_{S_n}} \cdot \cos\left(2k(z_R - z_{S_n})\right) + \tag{2.21}$$
$$+ \frac{\rho}{4}S(k) \cdot 2 \cdot \sum_{n<m} \sqrt{R_{S_n} R_{S_m}} \cdot \cos\left(2k(z_{S_n} - z_{S_m})\right).$$

Making use of the relation

$$\sum_{n<m} A_{nm} = \frac{1}{2} \sum_{n \neq m} A_{nm} \quad \text{for } A_{nm} = A_{mn} \; \forall n, m, \tag{2.22}$$

$I_D(k)$ can be expressed by

$$I_D(k) = \frac{\rho}{4}S(k) \cdot \left(R_R + \sum_n R_{S_n}\right) +$$
$$+ \frac{\rho}{2}S(k) \cdot \sum_n \sqrt{R_R R_{S_n}} \cdot \cos\left(2k(z_R - z_{S_n})\right) + \tag{2.23}$$
$$+ \frac{\rho}{2}S(k) \cdot \frac{1}{2} \cdot \sum_{n \neq m} \sqrt{R_{S_n} R_{S_m}} \cdot \cos\left(2k(z_{S_n} - z_{S_m})\right),$$

which finally yields

$$I_D(k) = \frac{\rho}{4}S(k) \cdot \left(R_R + \sum_n R_{S_n}\right) +$$
$$+ \frac{\rho}{2}S(k) \cdot \sum_n \sqrt{R_R R_{S_n}} \cdot \cos\left(2k(z_R - z_{S_n})\right) + \tag{2.24}$$
$$+ \frac{\rho}{4}S(k) \cdot \sum_{n \neq m} \sqrt{R_{S_n} R_{S_m}} \cdot \cos\left(2k(z_{S_n} - z_{S_m})\right).$$

In 2.24, the terms in the first line are called *DC-terms*, the ones in the second line are the *cross-correlation terms* and the ones in the last line are the *auto-correlation terms*. Izatt and Choma [20] explain the three terms as follows:

1. *DC-terms*: a path length-independent offset to the detector current, scaled by the light source wavenumber spectrum and with [an] amplitude proportional to the power reflectivity of the reference mirror plus the sum of the sample reflectivities. This term is often referred to as "constant" or "DC" component. This is the largest component of the detector current if the reference reflectivity dominates the sample reflectivity.

2. *Cross-correlation terms*: a "cross-correlation" component for each sample reflector, which depends upon both light source wavenumber and the path length difference between the reference arm and sample reflectors. This is the *desired component* for OCT imaging. Since these components are proportional to the square root of the sample reflectivities, they are typically smaller than the DC component. However, the square root dependence represents an important logarithmic gain factor over direct detection of sample reflections.

3. *Auto-correlation terms*: "auto-correlation" terms representing interference occurring between the different sample reflectors appear as artefacts in typical OCT system designs [...]. Since the autocorrelation terms depend linearly upon the power reflectivity of the sample reflections, a primary tool for decreasing autocorrelation artefacts is selection of the proper reference reflectivity so that the autocorrelation terms are small compared to the DC and interferometric terms. (Izatt and Choma [20])

For a single reflector, a schematic of $I_D(k)$ can be seen in Fig. 2.3: a DC term of the height proportional to $\frac{R_R + R_{S1}}{2}$ is modulated by a cosinusoidal cross-correlation term (height proportional to $\sqrt{R_R R_{S_1}}$, maxima at $k = \frac{\pi}{z_R - z_{S_1}}$). For only one reflector, there are no more cross correlation and no auto-correlation terms; these would only be seen for samples with more reflectors.
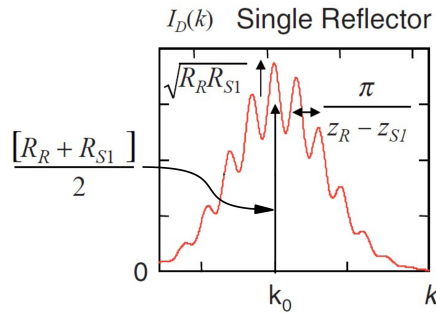
Figure 2.3: $I_D(k)$ for a single reflector [20] (variables explained in the text).

In the case of more than one reflecting layer in the sample, the DC-term would be modulated by several cosinusoidal cross-correlation and auto-correlation functions, the former scaled according to $\sqrt{R_R R_{S_n}}$, the latter according to $\sqrt{R_{S_n} R_{S_m}}$. The auto-correlation terms, which are undesired, are typically small. This is due to the fact that the sample reflectivities (in this case the reflectivities of layers in the background of the eye) are usually many orders of magnitude smaller than the reference reflectivity (namely the reflectivity of a mirror), i.e. $\sqrt{R_R R_{S_n}} > \sqrt{R_{S_n} R_{S_m}}$.

Furthermore, the distances between the reflectors in the sample tend to be small compared to the distance between the sample and the reference reflector, so the frequencies of the modulations due to autocorrelation are usually smaller than those of the cross-correlation terms.

2.2 Fourier Domain OCT

In practice, there are two different approaches to measuring the position of the sample layers with OCT, namely time domain optical coherence tomography (TDOCT) and Fourier domain optical coherence tomography (FDOCT). Both of them will be mentioned in the following.

2.2.1 Imaging depth: from TDOCT to FDOCT

Knowing how an interferometer works, TDOCT is probably the more intuitive method. In this case, the length of the reference arm is varied over time. Simultaneously, the intensity I_D at the detector is recorded. When the length of the reference arm coincides with the distance of one of the layers in the sample arm, constructive interference occurs. By detecting this interference, the position of the sample layers can be inferred from the reference arm length. The drawback of this method is that the variation of the reference arm's length is time costly. This problem can be overcome by using FDOCT.
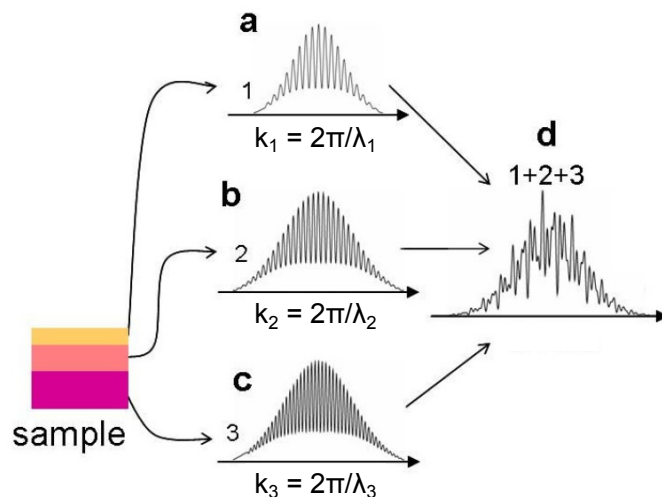
Figure 2.4: The detected spectral interferogram (d) is the combination of interferograms from reflectors at different depths in the sample (a)-(c). Larger depths of the reflecting layers lead to spectra with higher frequencies (adapted from [21]).

In FDOCT, the beam leaving the interferometer is transmitted through a diffraction grating. The grating disperses the beam according to its wavelengths and thus (due to $\lambda = \frac{c}{f}$) according to its frequency components, which are detected by a line camera. Hence, not simply the intensity of the beam leaving the interferometer, but rather its frequency components are measured. As can already be seen from Eq. 2.1, larger differences ΔL in the path length lead to a faster oscillation of the interference term (see also Fig. 2.4). Thus, layers in different depths result in different interference frequencies. The spectrum recorded behind the grating includes all the frequencies corresponding to the depth of the reflecting layers (see Fig. 2.5a). A Fourier transform (FT) yields peaks at each of the contained frequencies (Fig. 2.5b). In FDOCT, the position of the sample layers is thus inferred from the position of the spectrum's frequency components.
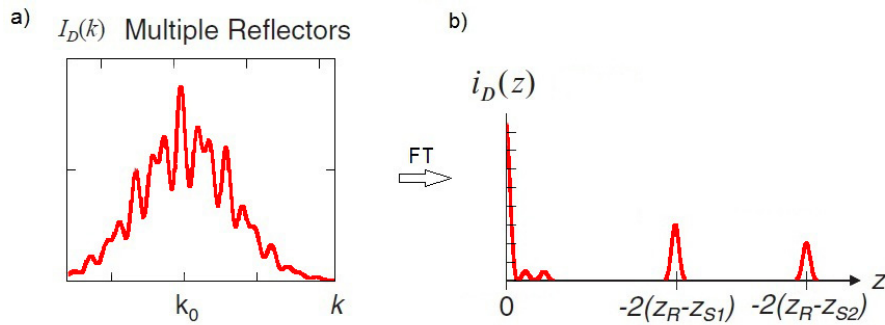
Figure 2.5: a) Measured frequency spectrum from a sample with reflectors in different depths z_{S_n}; b) real part of the Fourier transformed spectrum with peaks corresponding to the different depths of reflectors in the sample [20].

As mentioned above, the big disadvantage of TDOCT is that the the reference arm length has to be varied to get information from different depths. In FDOCT, on the other hand, the whole depth information is contained in one single measurement. This makes FDOCT much faster than TDOCT.

2.2.2 Mathematical description of FDOCT

Again, a thorough mathematical derivation can be found in Izatt and Choma [20], some of which will be explained in the following.

In Fourier domain OCT, the wavenumber-dependent detector current $I_D(k)$[iii] is measured and then Fourier-transformed to extract the encoded depth information

---

[iii]Recording $I_D(k)$ can either be done by sweeping a narrowband source over a wavenumber-region ('swept source OCT') or, as mentioned above, by using a broadband source and a diffraction grating ('Fourier domain OCT'). In the latter method, a grating is needed to disperse the light according to its different wavelengths λ and, thus, its different wavenumbers (as $k = \frac{2\pi}{\lambda}$).

$i_D(z)$, i.e.

$$i_D(z) = \mathcal{F}\big(I_D(k)\big). \tag{2.25}$$

The Fourier transform $\mathcal{F}$ of a function $f(k)$, which is used in this equation, can be defined as

$$\mathcal{F}(z) = \int_{-\infty}^{\infty} f(k) \cdot e^{-ikz} dk. \tag{2.26}$$

To perform the calculation of $i_D(z)$, the Fourier transform of $S(k)$ will be termed $\gamma(z)$:

$$S(k) \quad \overset{\mathcal{F}}{\longleftrightarrow} \quad \gamma(z), \tag{2.27}$$

and it helps to know the Fourier transform pairs

$$\cos kz_0 \quad \overset{\mathcal{F}}{\longleftrightarrow} \quad \frac{1}{2}\left[\delta(z + z_0) + \delta(z - z_0)\right] \tag{2.28}$$

$$X(k) \cdot Y(k) \quad \overset{\mathcal{F}}{\longleftrightarrow} \quad x(z) \otimes y(z). \tag{2.29}$$

Hereby, $\otimes$ denotes the convolution:

$$(f \otimes g)(z) = \int_{-\infty}^{\infty} f(\tilde{z})g(z - \tilde{z})\, d\tilde{z}. \tag{2.30}$$

The Fourier transformation of $I_D(k)$, which yields the space-resolved detector current $i_D(z)$ (cf. Eq. 2.25), can now be written as

$$
\begin{aligned}
i_D(z) ={} & \frac{\rho}{4}\gamma(z) \cdot \Big(R_R + \sum_n R_{S_n}\Big)+ \\
& + \frac{\rho}{4}\gamma(z) \otimes \sum_n \sqrt{R_R R_{S_n}} \left[\delta\big(z + 2(z_R - z_{S_n})\big) + \delta\big(z - 2(z_R - z_{S_n})\big)\right] + \\
& + \frac{\rho}{8}\gamma(z) \otimes \sum_{n \neq m} \sqrt{R_{S_n} R_{S_m}} \left[\delta\big(z + 2(z_{S_n} - z_{S_m})\big) + \delta\big(z - 2(z_{S_n} - z_{S_m})\big)\right].
\end{aligned}
\tag{2.31}
$$

Remembering that, with $\delta(-x) = \delta(x)$ and the definition of the convolution in Eq. 2.30,

$$
\begin{aligned}
f(t) \otimes \delta(t - T) &= \int_{-\infty}^{\infty} f(\tau)\delta(t - T - \tau)\, d\tau = \\
&= \int_{-\infty}^{\infty} f(\tau)\delta(\tau - (t - T))\, d\tau \\
&= f(t - T),
\end{aligned}
\tag{2.32}
$$

the convolutions with the δ-functions in the last two terms of Eq. 2.31 can be carried

out, and Eq. 2.31 becomes

$$i_D(z) = \frac{\rho}{4}\gamma(z) \cdot \left(R_R + \sum_n R_{S_n}\right) +$$
$$+ \frac{\rho}{4} \sum_n \sqrt{R_R R_{S_n}} \left[\gamma\big(z + 2(z_R - z_{S_n})\big) + \gamma\big(z - 2(z_R - z_{S_n})\big)\right] + \qquad (2.33)$$
$$+ \frac{\rho}{8} \sum_{n \neq m} \sqrt{R_{S_n} R_{S_m}} \left[\gamma\big(z + 2(z_{S_n} - z_{S_m})\big) + \gamma\big(z - 2(z_{S_n} - z_{S_m})\big)\right].$$

This equation consists of three parts which are equivalent to the parts of Eq. 2.24, namely the DC-term (1st line), the cross-correlation terms (2nd line) and the auto-correlation terms (3rd line).
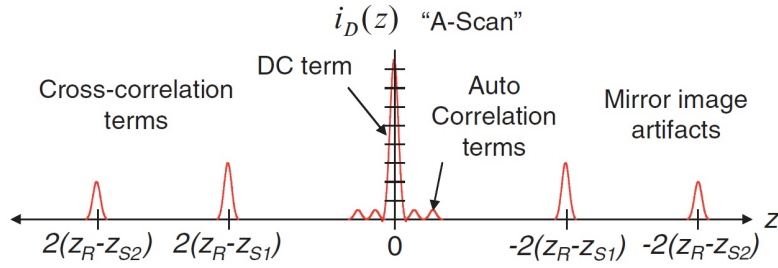
Figure 2.6: Example of space resolved detector current i_D (i.e. the depth information) for a sample with reflecting layers at z_{S_n} and a reference mirror at the position z_R [20].

An example of the calculated intensity i_D is shown in Fig. 2.6. The cross-correlation terms and the auto-correlation peaks are all centred around the DC-peak at $z = 0$: as can be seen in Fig. 2.6 and also in Eq. 2.33, both the cross-correlation terms and the auto-correlation terms have so-called mirror-images (i.e. a peak at a depth $2(z_R - z)$ has a corresponding peak at $-2(z_R - z)$). These mirror images can be problematic, as will be explained in the following.

The desired information in 2.33 are the locations z_{S_n} of the reflectors, which are inherent in the cross-correlation peaks. However, these locations are not always as obvious as in Fig. 2.6. Firstly, they can be superimposed by the auto-correlation terms, as the latter can be located in the same positions. Moreover, the mirror terms and the desired terms are only on separate sides of the DC peak if the distances z_{S_n} of *all* of the reflectors are either larger or smaller than the distance z_R of the reference mirror. Otherwise, terms and mirror terms will be mixed, making it difficult to distinguish 'true' peaks due to reflecting layers from those of the mirror terms.

There are several methods to eliminate the DC term, the auto-correlation terms, and the mirror-terms, so that only the desired cross-correlation terms are left. Descriptions of these methods can be found e.g. in Wojtkowski et al. [22] or Leitgeb et al. [23]. In the course of this work, however, the mirror terms and the DC-term were simply avoided by adjusting the reference arm length until all of the sample

layers were on the same side of and far enough away from the DC-peak. The autocorrelation terms could also be disregarded: the distance between the layers of the sample were so small that the autocorrelation terms lay very close to zero and blended into the DC-term.

2.3 Doppler-OCT

Doppler-OCT is a combination of the Doppler-principle and the OCT-method described above. It is, thus, a method to measure blood flow and tissue structure at the same time. As explained in the introduction, measuring tissue structures and blood flow simultaneously may provide critical information regarding ocular diseases [12], which explains the importance attributed to advances in Doppler-OCT by ophthalmologists and researchers alike.

2.3.1 Single beam Doppler-OCT

Mathematical descriptions of Doppler-OCT can be found e.g. in Werkmeister [24] or Chen and Zhang [12]. A concise explanation is given in the following.

The Doppler effect is well known, also to physical laymen, from the change in pitch in the sound of a passing emergency vehicle's horn. It applies not only to sound, but also to light: if a light beam is emitted from a source moving with the velocity v_S or detected by an receiver moving with v_R, the original frequency f_0 is Doppler shifted to a frequency f_D:

$$f_D = f_0 \cdot \frac{c \pm v_R}{c \mp v_S}, \tag{2.34}$$

where c is the velocity of light. The upper sign applies if source and receiver move towards each other, and the lower sign is to be used if they move away from each other. In vector form, this equation can be expressed as[iv]

$$f_D = f_0 \cdot \frac{c - \hat{k} \cdot \vec{v}_R}{c - \hat{k} \cdot \vec{v}_S}, \tag{2.35}$$

where $\hat{k} = \vec{k}/|\vec{k}|$ is the unit vector of the beam.

If a beam with the frequency f_0 is emitted from a stationary source in the direction $\hat{k}$ and falls onto a red blood cell (RBC) moving with a velocity $\vec{v}$ (see Fig. 2.7), then

---

[iv]The signs can be explained as follows: assume the beam travels from the source to the receiver in the positive x-direction, i.e. $\hat{k} = \hat{x}$. If the source moves towards the receiver, i.e. in x-direction ($\hat{k} \cdot \vec{v}_S > 0$), the frequency rises (the denominator decreases). The same is the case if the receiver moves towards the source, i.e. in $(-x)$-direction ($\hat{k} \cdot \vec{v}_R < 0$; the numerator increases).

the blood cell 'observes' the Doppler shifted frequency

$$f_D^{\text{RBC}} = f_0 \cdot \frac{c - \hat{k} \cdot \vec{v}}{c}. \tag{2.36}$$

If this light with the frequency f_{RBC} is now reflected from the moving RBC (which is thus now a moving source) and observed at a stationary detector positioned in the direction $-\hat{k}$, the detected frequency f_D will be

$$f_D = f_D^{\text{RBC}} \cdot \frac{c}{c - (-\hat{k}) \cdot \vec{v}}. \tag{2.37}$$

Inserting Eq. 2.36 yields

$$f_D = f_0 \cdot \frac{c - \hat{k} \cdot \vec{v}}{c} \cdot \frac{c}{c - (-\hat{k}) \cdot \vec{v}} = f_0 \cdot \frac{c - \hat{k} \cdot \vec{v}}{c + \hat{k} \cdot \vec{v}}. \tag{2.38}$$

The Doppler shift can be calculated as

$$\Delta f_D = f_0 - f_D = f_0 \cdot \left(1 - \frac{c - \hat{k} \cdot \vec{v}}{c + \hat{k} \cdot \vec{v}} \right) = f_0 \cdot \left(\frac{2\hat{k} \cdot \vec{v}}{c + \hat{k} \cdot \vec{v}} \right). \tag{2.39}$$

As $|\vec{v}| \ll c$, the term $\hat{k} \cdot \vec{v}$ can be neglected in the denominator, i.e.

$$\Delta f_D = f_0 \cdot \frac{2\hat{k} \cdot \vec{v}}{c}. \tag{2.40}$$

With

$$\omega = c|\vec{k}| = 2\pi f_0 \quad \Rightarrow \quad \hat{k} = \frac{\vec{k}}{|\vec{k}|} = \frac{c\vec{k}}{2\pi f_0}, \tag{2.41}$$

the Doppler shift can be written as

$$\Delta f_D = f_0 \cdot \frac{2c\vec{k} \cdot \vec{v}}{2\pi f_0 c} = \frac{\vec{k} \cdot \vec{v}}{\pi}. \tag{2.42}$$

The relation between $\vec{k}$ and $\vec{v}$ depends on the Doppler angle δ and is shown in Fig. 2.7.

The relation between the wavenumber k and the wavelength λ is

$$k = \frac{2\pi}{\lambda}. \tag{2.43}$$

As can be seen from Fig. 2.7,

$$\vec{k} \cdot \vec{v} = kv \cos \delta = \frac{2\pi}{\lambda} v \cos \delta, \tag{2.44}$$
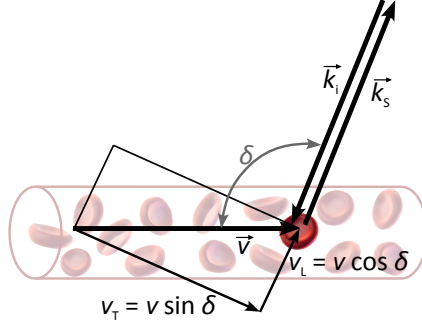
Figure 2.7: Red blood cell in a vessel moving with the velocity $\vec{v}$ and wave vectors $\vec{k}_i$, $\vec{k}_s$ of the incident and scattered measurement beam, respectively (adapted from Werkmeister [24], Chen and Zhang [12]).

so that Eq. 2.42 becomes

$$\Delta f_D = v \cdot \frac{2\cos\delta}{\lambda}. \tag{2.45}$$

The velocity is, thus, linearly related to the Doppler frequency shift. Hence, the question arises how Eq. 2.24 for the intensity measured at the detector and Eq. 2.33 for the encoded depth information change when considering a Doppler shift, and how this Doppler shift can be retrieved from the measured data.

The first task is thus to extend the mathematical description of OCT (see section 2.1.2) to include the Doppler shift. As in section 2.1.2, the electric field $E_{R,i}$ of the incident beam in the reference arm can be written as

$$E_{R,i} = \frac{s(k,\omega)}{\sqrt{2}} e^{i(kz-\omega t)}, \tag{2.46}$$

(cf. Eq. 2.4), which results in the same reflected reference beam's field as in Eq. 2.7:

$$E_R = \frac{s(k,\omega)}{\sqrt{2}} \cdot r_R \cdot e^{i(-kz-\omega t+2kz_R-\pi)}. \tag{2.47}$$

Assuming that the sample arm comprises moving surfaces (e.g. blood cells in a vessel), the beam reflected from the n-th layer in the sample arm will be Doppler shifted by an angular frequency of $\Delta\omega_n$. To obtain interference with the field exiting the reference arm with a wave vector k and an angular frequency ω, the field of the beam exiting the sample arm must have the same wave vector and angular frequency; one must thus consider an incident field $E_{S,i}$ with a *different* wave vector $(k + \Delta k_n)$ and a *different* angular frequency $(\omega + \Delta\omega_n)$,

$$E_{S,i} = \frac{s(k,\omega)}{\sqrt{2}} e^{i[(k+\Delta k_n)z-(\omega+\Delta\omega_n)t]}, \tag{2.48}$$

which, when reflected from the n-th, moving surface with a reflectivity of r_{S_n} at a certain depth z_{S_n}, will be Doppler shifted to match the reference arm's wave vector k and angular frequency ω:

$$E_{S_n} = \frac{s(k,\omega)}{\sqrt{2}} r_{S_n} e^{i(-kz-\omega t+\phi_S)}. \tag{2.49}$$

The additional phase ϕ_S of the beam from the sample arm can, as was done in section 2.1.2, be calculated using the fact that the incident and reflected beam's fields at the reflecting sample layer in the depth z_{S_n} must be identical but for the factor r_{S_n} and the phase shift π which is due to the reflection at the layer (cf. Eq. 2.6):

$$E_{S,i}(z_{S_n}) = \frac{E_{S_n}(z_{S_n}) \cdot e^{i\pi}}{r_{S_n}}$$

$$e^{i[(k+\Delta k_n)z_{S_n}-(\omega+\Delta\omega_n)t]} = e^{i(-kz_{S_n}-\omega t+\phi_S+\pi)} \tag{2.50}$$

$$\phi_S = 2kz_{S_n} + \Delta k_n z_{S_n} - \Delta\omega_n t - \pi.$$

Consequently, the electric field of the beam reflected back from the n-th layer in the sample is

$$E_{S_n} = \frac{s(k,\omega)}{\sqrt{2}} r_{S_n} e^{i(-kz-\omega t+2kz_{S_n}+\Delta k_n z_{S_n}-\Delta\omega_n t-\pi)} \tag{2.51}$$

and the total field exiting the sample arm is

$$E_S = \frac{s(k,\omega)}{\sqrt{2}} \sum_n r_{S_n} e^{i(-kz-\omega t+2kz_{S_n}+\Delta k_n z_{S_n}-\Delta\omega_n t-\pi)}. \tag{2.52}$$

In accordance with Eq. 2.9, the detected intensity is $I_D(k,\omega) = \frac{\rho}{2}\langle|E_R + E_S|^2\rangle$, i.e.

$$I_D(k,\omega) = \frac{\rho}{2}\left\langle\left|\frac{s(k,\omega)}{\sqrt{2}} \cdot r_R \cdot e^{i(-kz-\omega t+2kz_R-\pi)}\right.\right.$$

$$\left.\left. + \sum_n \frac{s(k,\omega)}{\sqrt{2}} r_{S_n} e^{i(-kz-\omega t+2kz_{S_n}+\Delta k_n z_{S_n}-\Delta\omega_n t-\pi)}\right|^2\right\rangle. \tag{2.53}$$

As in section 2.1.2, using the light source spectrum $S(k) = \langle|s(k,\omega)|^2\rangle$ and the relation $|e^{ix}|^2 = e^{ix} \cdot e^{-ix} = 1$, the equation can be simplified and one arrives at

$$I_D(k) = \frac{\rho}{4} S(k) \cdot \left\langle\left|r_R e^{2ikz_R} + \sum_n r_{S_n} e^{i(2kz_{S_n}+\Delta k_n z_{S_n}-\Delta\omega_n t)}\right|^2\right\rangle. \tag{2.54}$$

Expanding the square of the absolute value, using the power reflectivity $R = |r|^2$,

and following the same mathematical steps as in Eq. 2.16 to Eq. 2.18, $I_D(k)$ becomes

$$
\begin{aligned}
I_D(k) = \frac{\rho}{4}\, S(k) \cdot &\left\langle \left(R_R + \sum_n R_{S_n} \right) + \right. \\
&+ \sum_n \sqrt{R_R R_{S_n}} \left(e^{i(2k(z_R - z_{S_n}) - \Delta k_n z_{S_n} + \Delta \omega_n t)} + \text{c.c.} \right) + \\
&\left. + \sum_{n<m} \sqrt{R_{S_n} R_{S_m}} \left(e^{i(2k(z_{S_n} - z_{S_m}) + \Delta k_n z_{S_n} - \Delta k_m z_{S_m} + (\Delta \omega_n - \Delta \omega_m)t)} + \text{c.c.} \right) \right\rangle.
\end{aligned}
$$
(2.55)

Here, c.c. stands for the complex conjugate. With $e^{ix} + e^{-ix} = 2\cos x$ and Eq. 2.22, this equation can be rewritten:

$$
\begin{aligned}
I_D(k) = \frac{\rho}{4}\, S(k) \cdot &\left(R_R + \sum_n R_{S_n} \right) + \\
&+ \frac{\rho}{2}\, S(k) \sum_n \sqrt{R_R R_{S_n}} \cdot \left\langle \cos\left(2k(z_R - z_{S_n}) - \Delta k_n z_{S_n} + \Delta \omega_n t\right) \right\rangle + \\
&+ \frac{\rho}{4}\, S(k) \sum_{n \neq m} \sqrt{R_{S_n} R_{S_m}} \cdot \\
&\left\langle \cos(2k(z_{S_n} - z_{S_m}) + \Delta k_n z_{S_n} - \Delta k_m z_{S_m} + (\Delta \omega_n - \Delta \omega_m)t) \right\rangle.
\end{aligned}
$$
(2.56)

Just as in Eq. 2.24, the terms in the first row are the DC-terms (which are time-independent, so that the time average can be omitted there), the ones in the second row are the cross-correlation terms and the remaining terms are the auto-correlation terms. As mentioned in section 2.1.2, the relevant terms for OCT imaging are the cross-correlation terms in the second row. Comparing these to the cross-correlation terms without Doppler effect in Eq. 2.24, one finds that the first part is the same: once again, there is a cosinusoidal dependence on the path length difference $(z_R - z_{S_n})$ between the reference arm and the sample arm. However, one now finds additional terms: a constant offset of the phase, which depends on the shift Δk_n of the wave vector and the depth z_{S_n} of the reflecting layer, as well as a component depending on the shift $\Delta \omega$ of the angular frequency which changes with time.

Unlike in Eq. 2.24, the cosine terms in Eq. 2.56 depend on time. Hence, the time average cannot simply be omitted. In Doppler OCT measurements, the data are recorded during the exposure time τ of the camera. As the cosine terms in Eq. 2.56 are of the form $(a + bt)$, the time average for an exposure starting at t_0 and lasting

for a duration τ can be calculated using

$$
\frac{1}{\tau} \int_{t_0}^{t_0+\tau} \cos(a + bt) \, \mathrm{d}t = \left. \frac{\sin(a + bt)}{b\tau} \right|_{t_0}^{t_0+\tau}
$$
$$
= \frac{\sin(a + bt_0 + b\tau) - \sin(a + bt_0)}{b\tau}
$$
$$
= \frac{\sin\left[\left(a + bt_0 + \frac{b\tau}{2}\right) + \frac{b\tau}{2}\right] - \sin\left[\left(a + bt_0 + \frac{b\tau}{2}\right) - \frac{b\tau}{2}\right]}{b\tau}.
$$
(2.57)

In the last line, a mathematical 'trick' was employed to yield a function of the form $\sin(c + d) - \sin(c - d)$. Using the equivalence relation

$$
\sin(c \pm d) = \sin c \cos d \pm \cos c \sin d, \tag{2.58}
$$

Eq. 2.57 can be rewritten to

$$
\frac{1}{\tau} \int_{t_0}^{t_0+\tau} \cos(a + bt) \, \mathrm{d}t = \frac{1}{b\tau} \left[\sin\left(a + bt_0 + \frac{b\tau}{2}\right) \cos\left(\frac{b\tau}{2}\right) \right.
$$
$$
+ \cos\left(a + bt_0 + \frac{b\tau}{2}\right) \sin\left(\frac{b\tau}{2}\right)
$$
$$
- \sin\left(a + bt_0 + \frac{b\tau}{2}\right) \cos\left(-\frac{b\tau}{2}\right)
$$
$$
\left. - \cos\left(a + bt_0 + \frac{b\tau}{2}\right) \sin\left(-\frac{b\tau}{2}\right) \right].
$$
(2.59)

As $\cos(-a) = \cos(a)$ and $\sin(-a) = -\sin(a)$, the first and the third term cancel out and the second and fourth term are identical, leaving

$$
\frac{1}{\tau} \int_{t_0}^{t_0+\tau} \cos(a + bt) \, \mathrm{d}t = \frac{2}{b\tau} \cos\left(a + bt_0 + \frac{b\tau}{2}\right) \sin\left(\frac{b\tau}{2}\right). \tag{2.60}
$$

The integral of the detected current in Eq. 2.56 over a camera exposure starting at the time t_0 and lasting for a time τ can thus be written as

$$
I_D(k, t_0) = \frac{\rho}{4} S(k) \cdot \left(R_R + \sum_n R_{S_n} \right) +
$$
$$
+ \frac{\rho}{2} S(k) \sum_n \sqrt{R_R R_{S_n}} \cdot \frac{2}{\Delta\omega_n \tau} \sin\left(\frac{\Delta\omega_n \tau}{2}\right) \cdot
$$
$$
\cos\left(2k(z_R - z_{S_n}) - \Delta k_n z_{S_n} + \Delta\omega_n t_0 + \frac{\Delta\omega_n \tau}{2}\right) +
$$
$$
+ \frac{\rho}{4} S(k) \sum_{n \neq m} \sqrt{R_{S_n} R_{S_m}} \cdot \frac{2}{(\Delta\omega_n - \Delta\omega_m)\tau} \sin\left(\frac{(\Delta\omega_n - \Delta\omega_m)\tau}{2}\right) \cdot
$$
$$
\cos\left(2k(z_{S_n} - z_{S_m}) + \Delta k_n z_{S_n} - \Delta k_m z_{S_m} + (\Delta\omega_n - \Delta\omega_m)t_0 + \frac{(\Delta\omega_n - \Delta\omega_m)\tau}{2}\right).
$$
(2.61)

As can be seen, the general form of Eq. 2.24 and Eq. 2.61 are the same. However, the amplitude of the cross-correlation and the auto-correlation terms are weighted with a prefactor in Eq. 2.61 and the cosine terms contain a number of additional phase terms. One of these phase terms depends on starting time t_0 of the measurement – this is the one from which the Doppler shift and, subsequently, the velocity, will be extracted in the following.

It is worth noting that, for small phase shifts (i.e. small velocities) $\sin\left(\frac{\Delta\omega_n\tau}{2}\right) \approx \frac{\Delta\omega_n\tau}{2}$ and cancels out with $\frac{2}{\Delta\omega_n\tau}$ (the analogous relation holds true for the auto-correlation terms). Therefore, Eq. 2.24 and Eq. 2.61 are identical in the limit of vanishing Doppler shifts.

In order to determine the encoded depth information, Eq. 2.61 must be Fourier-transformed using the identities given in section 2.2.2 and

$$\cos(kz_0 + \psi) \quad \overset{\mathcal{F}}{\longleftrightarrow} \quad \frac{1}{2}\left[e^{-i\psi}\delta(z + z_0) + e^{i\psi}\delta(z - z_0)\right]. \tag{2.62}$$

Consequently, $i_D(z, t_0)$ can be written as

$$
\begin{aligned}
i_D(z, t_0) ={}& \frac{\rho}{4} \cdot \gamma(z) \cdot \left(R_R + \sum_n R_{S_n}\right) + \\
&+ \frac{\rho}{4} \cdot \sum_n \sqrt{R_R R_{S_n}} \cdot \frac{2}{\Delta\omega_n\tau} \sin\left(\frac{\Delta\omega_n\tau}{2}\right) \cdot \\
&\quad \cdot \left[\gamma\big(z + 2(z_R - z_{S_n})\big) \cdot e^{-i\left(-\Delta k_n z_{S_n} + \Delta\omega_n t_0 + \frac{\Delta\omega_n\tau}{2}\right)} + \right.\\
&\quad\left. + \gamma\big(z - 2(z_R - z_{S_n})\big) \cdot e^{i\left(-\Delta k_n z_{S_n} + \Delta\omega_n t_0 + \frac{\Delta\omega_n\tau}{2}\right)}\right] + \\
&+ \frac{\rho}{8} \cdot \sum_{n \neq m} \sqrt{R_{S_n} R_{S_m}} \cdot \frac{2}{(\Delta\omega_n - \Delta\omega_m)\tau} \sin\left(\frac{(\Delta\omega_n - \Delta\omega_m)\tau}{2}\right) \cdot \\
&\quad \cdot \left[\gamma\big(z + 2(z_{S_n} - z_{S_m})\big) \cdot e^{-i\left(\Delta k_n z_{S_n} - \Delta k_m z_{S_m} + (\Delta\omega_n - \Delta\omega_m)t_0 + \frac{(\Delta\omega_n - \Delta\omega_m)\tau}{2}\right)} + \right.\\
&\quad\left. + \gamma\big(z - 2(z_{S_n} - z_{S_m})\big) \cdot e^{i\left(\Delta k_n z_{S_n} - \Delta k_m z_{S_m} + (\Delta\omega_n - \Delta\omega_m)t_0 + \frac{(\Delta\omega_n - \Delta\omega_m)\tau}{2}\right)}\right].
\end{aligned}
\tag{2.63}
$$

As mentioned in section 2.2.2, the DC-term, the auto-correlation terms and the cross-correlation's mirror terms can be disregarded. The relevant information is contained in the 'true' cross-correlation terms $i^{\text{cross}}(z, t_0)$

$$
\begin{aligned}
i^{\text{cross}}(z, t_0) ={}& \frac{\rho}{4} \cdot \sum_n \sqrt{R_R R_{S_n}} \cdot \frac{2}{\Delta\omega_n\tau} \sin\left(\frac{\Delta\omega_n\tau}{2}\right) \cdot \\
&\cdot \gamma\big(z - 2(z_R - z_{S_n})\big) \cdot e^{i\left(-\Delta k_n z_{S_n} + \Delta\omega_n t_0 + \frac{\Delta\omega_n\tau}{2}\right)}. \tag{2.64}
\end{aligned}
$$

The cross-correlation term $i_n^{\text{cross}}(t_0)$ corresponding to the n-th layer is chosen by setting $z = 2(z_R - z_{S_n})$ (see Fig. 2.6):[v]

$$i_n^{\text{cross}}(t_0) = \frac{\rho}{4} \cdot \sqrt{R_R R_{S_n}} \cdot \frac{2}{\Delta\omega_n\tau} \sin\left(\frac{\Delta\omega_n\tau}{2}\right) \cdot \gamma(0) \cdot e^{i\left(-\Delta k_n z_{S_n} + \Delta\omega_n t_0 + \frac{\Delta\omega_n\tau}{2}\right)}. \quad (2.65)$$

A measurement started at a different time point $t_0 + \tau$ yields

$$i_n^{\text{cross}}(t_0 + \tau) = \frac{\rho}{4} \cdot \sqrt{R_R R_{S_n}} \cdot \frac{2}{\Delta\omega_n\tau} \sin\left(\frac{\Delta\omega_n\tau}{2}\right) \cdot \gamma(0) \cdot e^{i\left(-\Delta k_n z_{S_n} + \Delta\omega_n (t_0+\tau) + \frac{\Delta\omega_n\tau}{2}\right)}. \quad (2.66)$$

The quotient of the two measurements (assuming that both are $\neq 0$) takes the form

$$\frac{i_n^{\text{cross}}(t_0 + \tau)}{i_n^{\text{cross}}(t_0)} = e^{i\Delta\omega_n\tau}. \quad (2.67)$$

The phase difference $\Delta\phi_D$ between two consecutive measurements thus depends on the Doppler shift $\Delta\omega_n$, whereby

$$\Delta\phi_D = \Delta\omega_n \cdot \tau = 2\pi\Delta f_D \cdot \tau. \quad (2.68)$$

According to Eq. 2.45,

$$\Delta\phi_D = 2\pi v \cdot \frac{2\cos\delta}{\lambda} \cdot \tau. \quad (2.69)$$

Consequently,[vi]

$$v = \Delta\phi_D \cdot \frac{\lambda}{4\pi\tau \cdot \cos\delta}. \quad (2.70)$$

Considering that, in a medium,

$$\lambda = \frac{\lambda_0}{n}, \quad (2.71)$$

λ_0 being the wavelength in vacuum and n being the refractive index of the medium, this equation becomes

$$v = \Delta\phi_D \cdot \frac{\lambda_0}{4\pi\tau n \cdot \cos\delta}. \quad (2.72)$$

2.3.2 Dual beam bidirectional Doppler-OCT

One problem with determining the velocity from 2.72 is that this formula contains the Doppler angle δ, i.e. the angle between the beam and the vessel. In ophthalmology, this angle is usually unknown, as the axial inclination of a vessel is not visible

---

[v]Hereby, one assumes that γ is sufficiently narrow to distinguish separate layers.

[vi]Due to the fact that all phase values $\phi + 2n\pi$, $n \in \mathbb{Z}$, describe the same physical state, phase values are inherently ambiguous. In order to determine velocities which cause phase shifts exceeding $[0, 2\pi)$, the phase values must be unwrapped (see section 5.5.4).

in the *en-face* fundus images. This problem can be addressed in several different ways, one of which is the *dual beam* method. This detection scheme was first devised by Riva et al. [25] for a laser Doppler velocimetry (LDV) system. It was extended to *dual beam bidirectional Doppler-OCT* by Werkmeister [24], who illuminated the sample using two beams with different polarization states. If the angle between the two beams is known and under the assumption that the light is backscattered under this same angle, the Doppler angle is no longer necessary to determine the flow velocity of the measured particles.

The mathematical description of dual beam OCT (cf. [24, 25]) will be elaborated in the following.
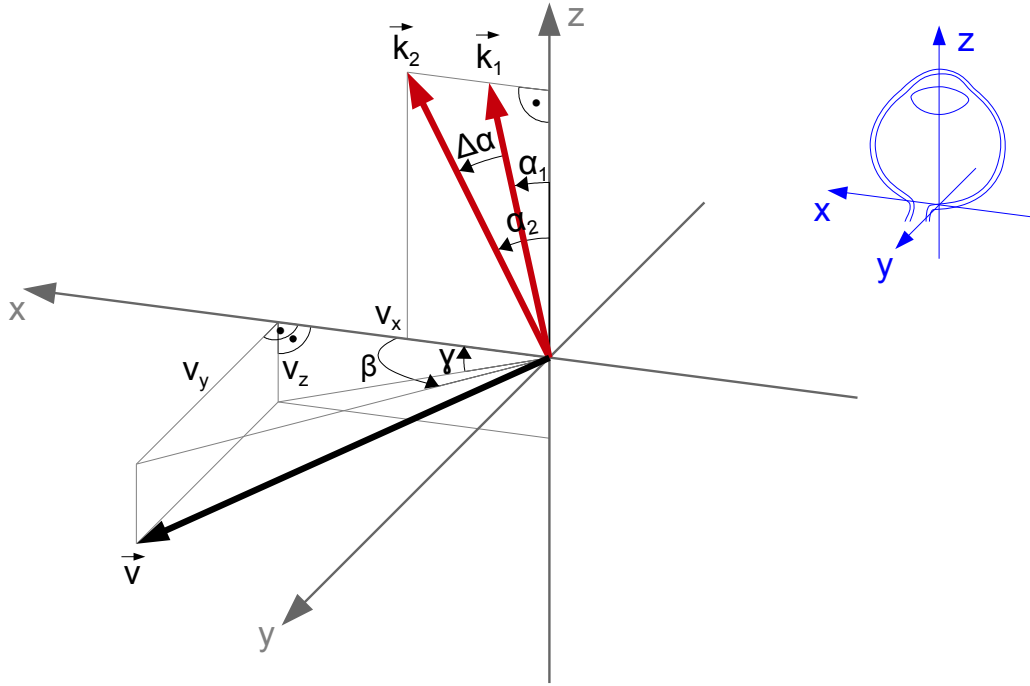
Figure 2.8: Sketch of the vectors in the dual beam method (adapted from Werkmeister [24] and Riva et al. [25]).

For the calculation, the x-z-plane is chosen such that the incident beams lie within it (see Fig. 2.8). The wave vector of the nth measurement beam ($n = 1, 2$) is thus given by

$$k_{n_x} = k \cdot \sin \alpha_n \tag{2.73}$$

$$k_{n_z} = k \cdot \cos \alpha_n, \tag{2.74}$$

whereas $k_{n_y} = 0$. The angles α_1 and α_2 used in the following lie between the z-axis and the beam (and not, as δ in section 2.3.1, between the vessel and the beam).

The velocity vector $\vec{v}$ is a vector in $\mathbb{R}^3$, determined by the angles β and γ as indicated

in Fig. 2.8. The components of v can be expressed starting from the relation

$$v = \sqrt{v_x^2 + v_y^2 + v_z^2}, \tag{2.75}$$

whereby

$$v_y = v_x \cdot \tan \beta \tag{2.76}$$
$$v_z = v_x \cdot \tan \gamma. \tag{2.77}$$

Combining these equations yields

$$v = \sqrt{v_x^2 + v_x^2 \tan^2 \beta + v_x^2 \tan^2 \gamma}. \tag{2.78}$$

Using the relation

$$\tan a = \frac{\sin a}{\cos a}, \tag{2.79}$$

v can be written as

$$
\begin{aligned}
v &= \sqrt{v_x^2 + v_x^2 \cdot \frac{\sin^2 \beta}{\cos^2 \beta} + v_x^2 \cdot \frac{\sin^2 \gamma}{\cos^2 \gamma}} \\
&= \frac{v_x}{\cos \beta \cos \gamma} \sqrt{\cos^2 \beta \cos^2 \gamma + \sin^2 \beta \cos^2 \gamma + \sin^2 \gamma \cos^2 \beta} \\
&= \frac{v_x}{\cos \beta \cos \gamma} \sqrt{\cos^2 \beta (\sin^2 \gamma + \cos^2 \gamma) + \sin^2 \beta \cos^2 \gamma}.
\end{aligned} \tag{2.80}
$$

As $(\sin^2 a + \cos^2 a) = 1$, this is equivalent to

$$v = \frac{v_x}{\cos \beta \cos \gamma} \sqrt{\cos^2 \beta + \sin^2 \beta \cos^2 \gamma}. \tag{2.81}$$

The velocity's x-component v_x can thus be expressed as

$$v_x = \frac{v \cos \beta \cos \gamma}{\sqrt{\cos^2 \beta + \sin^2 \beta \cos^2 \gamma}}. \tag{2.82}$$

Using the relations given in Eq. 2.77 and Eq. 2.79, the z-component v_z becomes

$$
\begin{aligned}
v_z &= \frac{v \cos \beta \cos \gamma}{\sqrt{\cos^2 \beta + \sin^2 \beta \cos^2 \gamma}} \cdot \frac{\sin \gamma}{\cos \gamma} \\
&= \frac{v \cos \beta \sin \gamma}{\sqrt{\cos^2 \beta + \sin^2 \beta \cos^2 \gamma}}.
\end{aligned} \tag{2.83}
$$

Using Eq. 2.42 and remembering the assumption made above that $k_{n_y} = 0$, the Doppler shift for beam n is

$$\Delta f_{D_n} = \frac{\vec{k}_n \cdot \vec{v}}{\pi} = \frac{1}{\pi} \left(k_{n_x} v_x + k_{n_z} v_z \right) \tag{2.84}$$

which, with $\Delta\phi_{D_n} = 2\pi\Delta f_{D_n} \cdot \tau$ (cf. Eq. 2.68), becomes

$$\Delta\phi_{D_n} = 2\tau \left(k_{n_x} v_x + k_{n_z} v_z \right). \tag{2.85}$$

Thus, the difference $\Delta\phi$ between the Doppler shifts of beam 1 and beam 2 can be written as

$$
\begin{aligned}
\Delta\phi &= \Delta\phi_{D_1} - \Delta\phi_{D_2} \\
&= 2\tau \left(\vec{v} \cdot \vec{k}_1 - \vec{v} \cdot \vec{k}_2 \right) = 2\tau \left(v_x k_{1x} + v_z k_{1z} - (v_x k_{2x} + v_z k_{2z}) \right).
\end{aligned}
$$

Inserting the equations for the vector-components derived above, this becomes

$$\Delta\phi = 2\tau k \frac{v \cos\beta}{\sqrt{\cos^2\beta + \sin^2\beta \cos^2\gamma}} \cdot$$
$$(\cos\gamma \sin\alpha_1 + \sin\gamma \cos\alpha_1 - (\cos\gamma \sin\alpha_2 + \sin\gamma \cos\alpha_2)). \tag{2.86}$$

As $(\cos a \sin b + \sin a \cos b) = \sin(a + b)$, this can be simplified to

$$\Delta\phi = 2\tau k \frac{v \cos\beta}{\sqrt{\cos^2\beta + \sin^2\beta \cos^2\gamma}} \cdot \left(\sin(\gamma + \alpha_1) - \sin(\gamma + \alpha_2) \right). \tag{2.87}$$

The inclination γ of retinal vessels is limited by the thickness of the retina; for vessels close to the eye's posterior pole[vii], $\gamma \approx 0$. Considering this and noting, once again, that $(\sin^2 a + \cos^2 a) = 1$,

$$
\begin{aligned}
\Delta\phi &\approx 2\tau k \frac{v \cos\beta}{\sqrt{\cos^2\beta + \sin^2\beta \cos^2 0}} \cdot \left(\sin(\alpha_1) - \sin(\alpha_2) \right) \\
&= 2\tau k \frac{v \cos\beta}{\sqrt{\cos^2\beta + \sin^2\beta}} \cdot \left(\sin(\alpha_1) - \sin(\alpha_2) \right) \\
&= 2\tau k v \cos\beta \cdot \left(\sin(\alpha_1) - \sin(\alpha_2) \right).
\end{aligned}
\tag{2.88}
$$

As regards the angles α_1 and α_2, one has to keep in mind that both beams have to be transmitted through the iris to reach the retina. The angles α_1 and α_2 are, therefore, small. As

$$a \text{ small} \quad \Rightarrow \quad \sin a \approx a, \tag{2.89}$$

the phase shift is approximately

$$\Delta\phi \approx 2\tau k v \cos\beta \cdot \left(\alpha_1 - \alpha_2 \right). \tag{2.90}$$

Using Eq. 2.43 and 2.71 results in

$$\Delta\phi \approx 2\tau \cdot \frac{2\pi n}{\lambda_0} \cdot v \cos\beta \left(\alpha_1 - \alpha_2 \right) = \frac{4\pi n\tau \cdot v \cos\beta}{\lambda_0} \left(\alpha_1 - \alpha_2 \right). \tag{2.91}$$

[vii]The posterior pole is the point where the optical axis intersects the retina. This is not equivalent to the position of the optic nerve head (cf. Fig. 5.1).

Thus, the velocity of the particles measured with the dual beam method is

$$v = \Delta\phi \cdot \frac{\lambda_0}{4\pi n\tau \cdot \cos\beta \cdot \Delta\alpha}, \tag{2.92}$$

where β is the angle of the vessel projected into the x-z-plane, which can be measured in a fundus view, and $\Delta\alpha = \alpha_1 - \alpha_2$ is the angle in radians between the beams which is known from the experimental setup. The velocity measured with the dual beam method is, thus, no longer dependent on the unknown angles γ, α_1, and α_2.

2.3.3 Limitations of dual beam bidirectional Doppler-OCT

As explained in section 2.3.2, dual beam Doppler OCT allows determining the absolute blood flow velocity in the eye directly from the measurable values. Nevertheless, the method has limitations, which should not go unmentioned.

First, the range of velocities that can be measured with dual beam Doppler OCT is restricted in practice. The upper limit v_{max}, being the highest unambiguously detectable (i.e. without unwrapping, cf. section 5.5.4) velocity, is inherent to the system: as all phase values $\phi + 2n\pi$ with $n \in \mathbb{Z}$ describe the same physical state, phase values can only be determined unambiguously if their range does not exceed 2π.[viii] The phase shift induced for a certain velocity is smallest (namely zero) when the angle of incidence of the beam on the vessel is perpendicular. Thus, high velocities can still be measured unambiguously if only the beam's angle of incidence is close enough to 90°. However, the two beams in the dual beam method cannot both impinge perpendicularly, as they are separated by a fixed angle $\Delta\alpha$. The highest unambiguously measurable velocity can thus be achieved if the two beams impinge on the vessel with their axis of symmetry perpendicular to the vessel.

The value of v_{max} can be calculated using Eq. 2.92 and inserting the maximal unambiguous phase shift difference $\Delta\phi_{\mathrm{max}} = 2\pi$; for the sake of comparability, v_{max} is customarily calculated at an angle $\beta = 0°$. With the setup's central wavelength of 838.8 nm, the camera's shortest line period of $\tau = 14.2\,\mu\mathrm{s}$, and the angle $\Delta\alpha = 0.096\,62\,\mathrm{rad}$ (see chapter 3.1) the maximal velocity can be calculated to be

$$v_{\mathrm{max}} = 2\pi \cdot \frac{838.8\,\mathrm{nm}}{4\pi \cdot 14.2\,\mu\mathrm{s} \cdot \cos 0 \cdot 0.096\,62\,\mathrm{rad}} = 306\,\mathrm{mm/s}. \tag{2.93}$$

In practice, however, this value will never be reached: in vivo, the situation that the beam's axis of symmetry is perpendicular to the velocity vector will practically never occur, as can be inferred from section 5.4.1 describing the scanning pattern. Moreover, for the vast majority of vessels, the angle β is not exactly zero. Furthermore, the line rate of the camera will not be set to its minimal value, as this

---

[viii]Else, the phase values must be unwrapped (see section 5.5.4).

would entail that slower velocities would not be measured accurately. Consequently, the highest actually measurable, unambiguous velocity v_{max} lies around $20\,\text{mm/s}$ to $30\,\text{mm/s}$.

The lowest measurable velocity value v_{min} is determined by the phase noise $\Delta\phi_{\text{err}}$. Using the full width at half maximum of the phase distribution measured in a static tissue region as an estimate for the phase noise (as suggested by Schmoll et al. [26]), the value $\Delta\phi_{\text{err}} \approx 0.4\,\text{rad}$ was found for the system described in this thesis for typical B-scans, recorded with a line period of $27\,\mu\text{s}$. With $\beta = 0°$ and a refractive index of tissue of about 1.35, the minimum velocity is

$$v_{\text{min}} = 0.4 \cdot \frac{838.8\,\text{nm}}{4\pi \cdot 1.35 \cdot 27\,\mu\text{s} \cdot \cos 0 \cdot 0.096\,62\,\text{rad}} = 7.6\,\text{mm/s}. \qquad (2.94)$$

However, this value is calculated for the phase noise of one pixel. Averaging over the whole vessel with N pixels will improve the SNR by a factor of $\sqrt{N}$.

A second limitation of dual beam OCT is that the *en-face* angle β at the measurement position must be determined (see section 5.5.8), because it is necessary to calculate the velocity. As this must be done manually and at the exact position of the measurement, this step is always subject to uncertainty.

Thirdly, a problem arises in the case of high velocity components transversal to the measurement beams. In this case, as shown by Koch et al. [27], the phase shift is no longer proportional to the velocity, and can even become independent of the velocity. Regarding the measurement geometry and velocities measured in this work, this effect is not yet problematic; nevertheless, one should be aware of the limitation when planning measurements.

Additionally, a number of non-system-inherent factors can limit the measurement accuracy. These include movements and small pupil sizes of the measured subjects (the latter preventing the unobstructed passage of both beams into the eye), inexact focussing of the beams onto the measured vessels (thus changing the measurement geometry, so that Eq. 2.92 is no longer applicable) and bends or bifurcations which distort the flow profiles [28], which would have to be taken into account in the evaluation of the data; bends in the axial z-direction are not be visible in the en-face fundus images that are used for the planning of the measurement positions, and can therefore not be avoided (whereas bifurcations and bends in the x-y-plane *can* be avoided by an appropriate choice of measurement positions).

In spite of the limitations, however, dual beam OCT is a well-suited method for measuring the retinal blood flow – hence the large number of publications on this topic. An awareness of the limitations of dual beam OCT will only further the reliable assessment of the method's capabilities and accuracy.

Chapter 3

Experimental setup

3.1 Setup of the OCT system

As mentioned in chapter 2, the basis of an OCT system is an interferometer. The interferometer in the system described in this thesis is basically the same as the simple setup depicted in Fig. 2.1, but it incorporates a number of additions. A schematic drawing of the system is given in Fig. 3.1. The following sections will explain the setup and its components in more detail.

3.1.1 Light source

The most commonly used light sources in OCT systems, also used in the system described in this work, are superluminescent diodes (SLDs). SLDs could be described as laser diodes without a resonator: they are optoelectronic semiconductor devices, made e.g. of GaAs, with a pn-junction. The pn-junction is manufactured such that it has a number of possible states at different energy levels. By applying a forward current to the junction (resulting in a population inversion), amplified spontaneous emission (also called *superluminescence*) can thus generate a wide wavelength spectrum. Lacking a resonator, SLDs do not exhibit any lasing action, but have
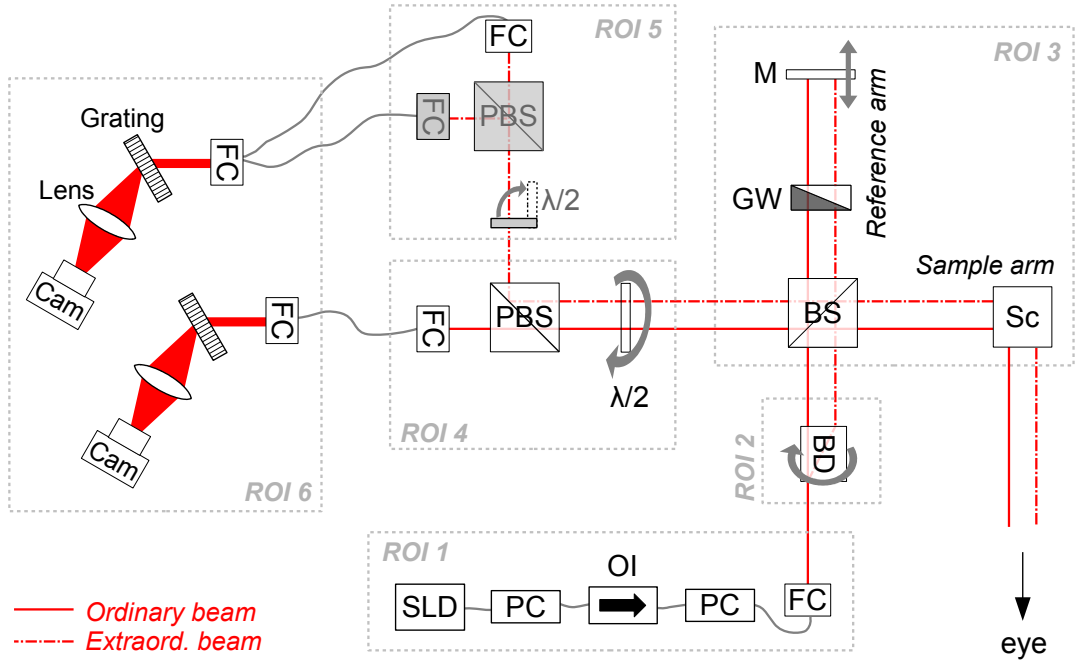
Figure 3.1: Schematic drawing of the OCT setup with regions of interest (ROI). BD = beam displacer, Cam = camera, FC = fiber collimator, GW = grey wedge, $\lambda/2$ = halfwave-plate, M = mirror, OI = optical isolator, (P)BS = (polarizing) beam splitter, PC = polarization controller, Sc = scanner, SLD = superluminescent diode.

a sufficiently high single-pass amplification to generate the necessary spontaneous emission.

The SLD used here was produced by Superlum (SLD-371-HP1-DIL-SM-PD); it has a central wavelength of 838.8 nm and a spectral bandwidth of 54 nm. The SLD is fiber pigtailed, which means that the light is emitted into an attached fiber rather than into free space.

Behind the SLD, several additional components are needed before the beam enters the interferometer: an optical isolator, two polarization controllers, and a collimator are included in the system (see ROI 1 in Fig. 3.1). The reasons for integrating these additional parts are given in the following.

Adding an optical isolator (OI, Thorlabs, IO-F-SLD100-840) is necessary to protect the diode from light reflected back in its direction. The basic principle on which OIs operate is the rotation of the light's polarization; a detailed explanation of their mode of operation can be found in appendix A.1.

The reason for adding polarization controllers (PCs) is, of course, to control the polarization direction of the beam: the first of the PCs is added because the optical isolator is not completely polarisation insensitive (which, actually, it would be

supposed to be). The amount of light transmitted through the isolator can thus be maximised by adjusting the polarisation. The second polarisation controller defines the polarisation direction of the light entering the system, which must be inclined towards the beam displacer's axes by 45° (see section 3.1.2).

There are different kinds of PCs; the ones used in this setup (Thorlabs, FPC030) consist of three paddles with a circular groove into which an optical fiber can be looped. These polarization controllers make use of the fact that stresses induce birefringence in the fibers; the amount of birefringence achieved depends on the fiber cladding diameter, the spool diameter, the number of fiber loops per spool, and the wavelength of the light. The fast axis of the fiber is in the plane of the spool. Depending on the amount of loops of the fibers in a certain paddle, these can be made to act as quarter-wave plates or half-wave plates. With the three paddles, any polarization state can be achieved, as an arbitrary incoming state can be transformed to a linear polarization (the first paddle acting as quarter-wave plate), rotated (second paddle = half-wave plate) and re-transformed to the arbitrary polarization state required (third paddle = quarter-wave plate).

As mentioned above, the light moves in a fiber from the SLD until after the second polarization controller. To ensure that the light exits this fiber as *collimated* beam, it passes a fiber collimator (FC, TE Lintelo Systems, HPUCO-23-840-S-6.2AS). This component couples the fiber to free space, passing the beam through a collimating lens.

3.1.2   Rotating beam displacer

Dual beam bidirectional Doppler OCT needs two beams (cf. section 2.3.2). Hence, the light exiting the collimator is split up into two orthogonally polarized, parallel output beams with a displacement of 2.7 mm using a beam displacer (BD, see ROI 2 in Fig. 3.1). A beam displacer (BD) is simply a birefringent crystal (in this case calcite), which has different refractive indices for different polarization directions. The so-called "ordinary beam" (portion of the incident beam with a certain polarization direction) is transmitted according to the law of refraction, whereas the "extraordinary beam" (portion of the incident beam with a polarization perpendicular to that of the ordinary beam) is transmitted with a different angle, thus splitting a beam into its polarization components.

To guarantee that both beams behind the beam displacer are of equal intensity, the incident beam's polarization state has to be inclined by exactly 45° towards the beam displacer's axes of ordinary and extraordinary transmission. This can be achieved by adjusting the polarization with the second polarization controller mentioned in section 3.1.1.
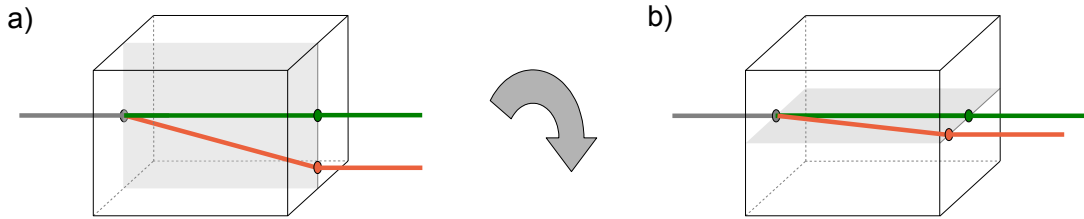
Figure 3.2: Beam displacer with ordinary (green) and extraordinary (orange) beams. Rotating the beam displacer by 90° moves the beams from a position above each other (a) to a position beside each other (b).

In the setup described in this thesis, the beam displacer (Thorlabs, BD27) is mounted in a rotation stage (Thorabs, PRM1/MZ8), which can be controlled via a computer. Via a 90°-rotation of the beam displacer, the extraordinary beam can be moved from a position below the ordinary beam (see Fig. 3.2a) to a position beside the latter (Fig. 3.2b).

Being able to align the beams vertically or horizontally to each other is necessary in order to measure vessels with all orientations. This will be illustrated using the example of a horizontally oriented vessel (such as the one depicted by the black arrow in Fig. 3.3). If the beams are vertically aligned when they impinge on the vessel, as in Fig. 3.3a, then the vessel's velocity vector does not have a component in direction of the plane spanned by the beams (visualized as transparent red plane in Fig. 3.3). In consequence, the beams will not be Doppler shifted and the vessel's velocity cannot be determined.[i] Rotating the beams to a horizontal position (Fig. 3.3b) will align the detection plane with the vessel's velocity vector ($\beta = 0°$): a Doppler shift will occur in the beams, from which the velocity in the vessel can be deduced. Summarizing, horizontal velocity vectors can only be measured with a horizontally aligned detection plane (and, likewise, vertical ones can only be measured with a vertical detection plane).

Rotating the beams by means of the BD's rotation has the disadvantage that the beams' polarization changes as well. This, however, can be reversed by a half-wave plate, as will be discussed in section 3.1.4.

3.1.3   Interferometer

After the beam is split into two perpendicularly polarized, laterally separated beams by the BD, these two beams enter the interferometer (ROI 3 in Fig. 3.1). Here, the

---

[i]Mathematically, the problem becomes obvious from Eq. 2.92: if the angle β between the vessel and the plane spanned by the beams approaches 90° (as in Fig. 3.3a), then the denominator of Eq. 2.92 approaches zero and the equation can no longer be solved.
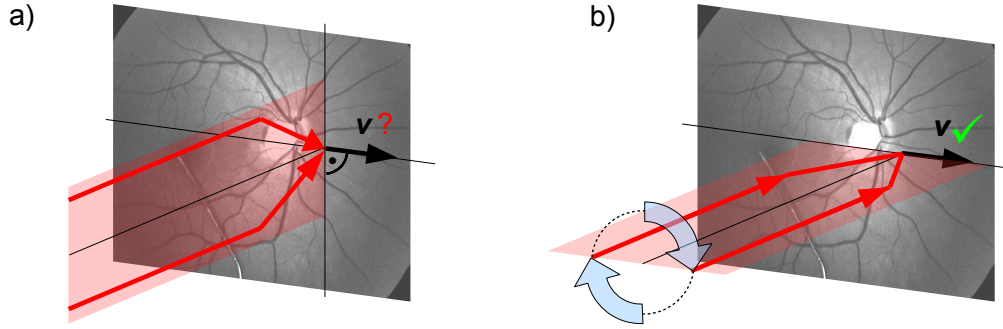
Figure 3.3: Rationale for rotating the detection plane (visualized as red transparent area) spanned by the OCT beams (red arrows) to measure a vessel's velocity vector (black arrow). a) If the vessel's velocity vector is perpendicular to the beams' plane, it does not induce a Doppler shift in the beams. Thus, the velocity cannot be determined. b) Rotating the beams aligns them with the velocity vector; a Doppler shift can occur – the velocities can be measured.

beams first fall onto a non-polarizing beam splitter (BS, Thorlabs, BS017). Half of each of the two beams is transmitted through the beam splitter (BS) into the interferometer's reference arm, the other half is reflected into the sample arm. Parts of both beams are reflected back from both the sample and from the reference mirror. These parts of each of the two beams are reunited at the beam splitter and pass on in direction of the cameras. Before going into detail on the system's components behind the interferometer, however, the sample- and the reference arm will be explained in more detail.

Reference arm

The reference arm consists of the reference mirror, a dispersion compensating glass block and a grey wedge (GW). The glass block actually consists of two glass prisms which are joined with an index-matching fluid to minimize reflection losses at the prisms' interface. Shifting the prisms relatively to each other allows changing the block's geometric length, and thus also their optical length (i.e. their length multiplied by their refractive index). By choosing an optical length that is equivalent to that of the lenses and the ocular media in the sample arm, the dispersion in both arms can be matched.

The grey wedge in the reference arm is required to attenuate the beam so as not to exceed the maximum power the cameras can handle. This is necessary in the reference arm only, as the proportion of light reflected by the reference mirror is very high (higher by far than the proportion reflected back from the eye's fundus in the sample arm). Naturally, the grey wedge must be rotatable as well, so that both beams will be attenuated equally, no matter what their orientation.
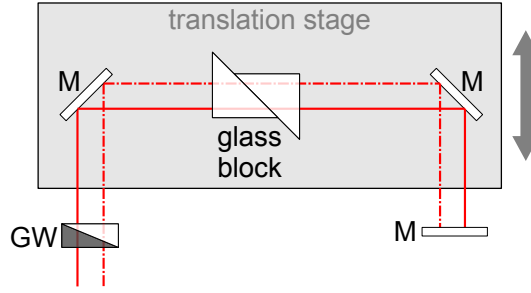
Figure 3.4: Reference arm: the beam path is folded with two mirrors in 45°. A translation stage allows changing the arm's length. Two prisms forming a glass block are used to match the dispersion of the beams in the sample arm.

Due to spatial restrictions, the beam path in the reference arm is not straight, as depicted in Fig. 3.1, but folded via two gold mirrors (Thorlabs, PF10-03-P01), as shown in Fig. 3.4. Moreover, it is not the reference mirror that can be shifted to change the reference arm's length, but a translation stage. This stage moves both the gold mirrors and thus changes the reference arm's length by twice its translation.

Sample arm

The sample arm incorporates a galvo-scanner (Sc), a lens system (not shown in Fig. 3.1), and the sample. The lens system is necessary to define the position of the beams upon entering the eye and will be discussed in detail in section 3.2.5.

The scanner (Cambridge Technology, 6220H) consists of two orthogonal mirrors, mounted at a right angle to each other. Turning the mirrors deflects the beams vertically and horizontally (see Fig. 3.5a and Fig. 3.5b, respectively), thus scanning them across the sample.

As explained in section 3.1.2, the alignment of the beams must correspond to the direction of the velocity vector to be measured: to measure horizontal velocities, the beams must be displaced horizontally. However, not only the alignment of the beams depends on the vessel's orientation. The scanning direction must also be chosen according to the vessel geometry: To measure the velocity profile in a horizontally oriented vessel, the measurement beams must be scanned over the vessel's cross-section, i.e. vertically. This scanning layout is shown in Fig. 3.5a: the y-mirror will move fast, scanning the beams vertically across the sample, while the x-mirror's position will be constant, determining the lateral scanning position. Vice versa, the cross-section of a vertically oriented vessel is recorded by scanning the vertically aligned beams *horizontally* over the vessel's cross-section (see Fig. 3.5b): the x-mirror will be moving fast, while the y-mirror remains static.

46
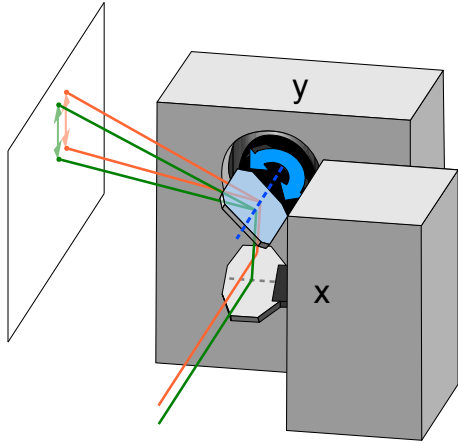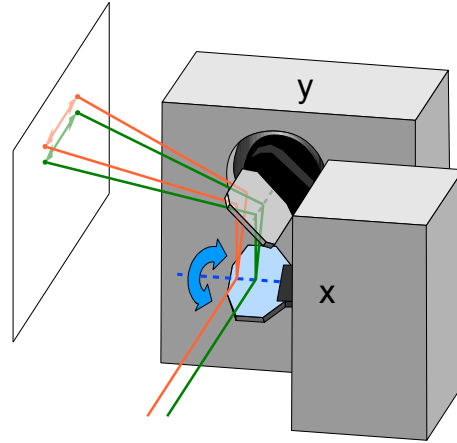
Figure 3.5: Alignment of the ordinary beam (green) and the extraordinary beam (orange) on the scanner when scanning in (a) vertical and (b) horizontal direction. The mirror's pivot axes are indicated by dashed lines; the movement of the fast scanning mirror (blue) is indicated by a blue arrow.

If the measurement beams are, on their way to the sample, reflected from a moving object, then an unwanted Doppler shift will be induced in the beams. This shift will overlay the Doppler shifts from moving particles in the sample. So as to avoid such unwanted Doppler shifts induced by the movement of the scanner's fast-moving mirror, the alignment of the beams on the mirrors is very important: both beams must fall onto the pivot axis of the fast mirror. Thus, when scanning in vertical direction, both beams must fall onto the y-mirror's pivot axis (dashed blue line in Fig. 3.5a); when scanning in horizontal direction, the beams must fall onto the x-mirror's pivot axis (dashed blue line in Fig. 3.5b). As explained in section 3.1.2, the ordinary beam's position is constant while the extraordinary beam can be rotated around it. Hence, the ordinary beam must fall on *both* mirror's pivot axes at all times. The extraordinary beam's position as well as the scanning direction depend on the orientation of the vessel to be measured, but their alignment will always be such that the beam falls onto the respective fast-moving mirror's pivot axis. This is depicted in Fig. 3.5: the ordinary beam (green) falls on both mirror's axes, independent of which one is the fast scanning one. The extraordinary beam (orange) falls only onto the fast-moving mirror's pivot axis, and hits the other, static mirror at some point off the pivot axis.

3.1.4   Beam separation

Once the reference and the sample parts of each beam are reunited after passing the interferometer, it is necessary to measure their spectra to extract the interference

signals (i.e. the information on the sample). To this end, each beam has to be coupled into an FC to transmit it into the fiber that passes it on to its respective spectrometer. However, the FCs have outer diameters of around 3 cm, but the beams are only a few millimetres apart. Consequently, the beams' spatial separation must be increased significantly so that each one can be passed into its respective FC. To achieve this goal, one makes use of the fact that the two beams have perpendicular polarization states (as explained above, the original SLD-beam was split according to its two polarization components). Thus, the separation can be achieved by using a polarizing beam splitter (PBS, Thorlabs, PBS252). The polarizing beam splitter (PBS) is set into the beam path in such a way that it transmits the ordinary beam and deflects the extraordinary one (cf. Fig. 3.1, ROI 4).
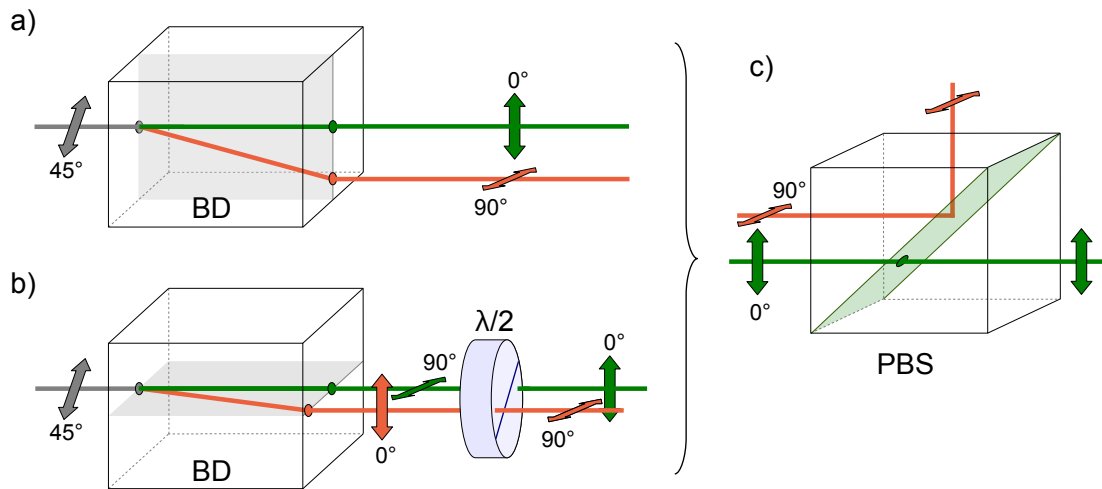
Figure 3.6: Depending on the orientation of the beam displacer (BD), the polarization states of the ordinary beam (green) and the extraordinary beam (orange) are exchanged. A half-wave plate ($\lambda/2$) counteracts this exchange, ensuring the correct transmission and reflection behaviour at the PBS.

A slight problem in separating the beams by their polarization components arises when changing the beam's relative position by rotating the beam displacer (cf. section 3.1.2), as the BD's rotation exchanges the polarization of the beams. If, before the rotation, the ordinary beam passed straight through the PBS and the extraordinary beam was deflected, the opposite will be the case after the rotation: undesirably, the extraordinary beam would be transmitted and the ordinary one deflected. The problem hereby is the alignment of the FCs which should couple a beam into a fiber: the beam can only enter the FC if it is aligned perfectly with the FC's centre (which would not be the case if the extraordinary beam were to impinge on the FC aligned with the ordinary beam). It is thus necessary to ensure that the ordinary beam is always transmitted and the extraordinary beam always reflected by the PBS. This is possible when including a rotatable half-wave plate ($\lambda/2$, Thorlabs, AHWP05M-980) into the setup (termed $\lambda/2$ in ROI 4 in Fig. 3.1). The situation is graphically represented in Fig. 3.6, assuming that the PBS will transmit a beam

polarized at 0°, while a beam polarized at 90° will be deflected (see Fig. 3.6c). If the BD is in its original position (Fig. 3.6a), then the ordinary beam is polarized at 0° and transmitted, and the extraordinary beam is polarized at 90° and deflected. If, however, the BD is turned to change the beam's relative position from vertical to horizontal (Fig. 3.6b), then the ordinary beam is polarized at 90° and would be deflected, while the extraordinary one, with a polarization of 0°, would be transmitted. In this latter case, inserting the half-wave plate restores the original polarization states, thereby re-establishing the transmission of the ordinary beam and the deflection of the extraordinary one.
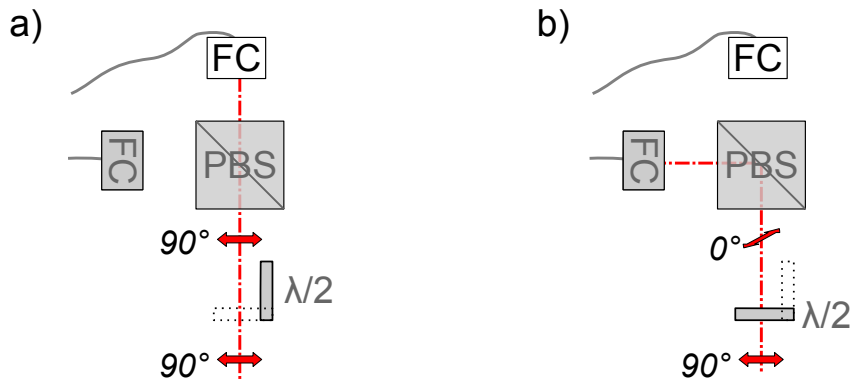
Figure 3.7: Extraordinary beam's path when vertically (a) or horizontally (b) displaced relative to the ordinary beam.

The one problem that remains now is that the extraordinary beam can be in two different positions (i.e. either vertically or horizontally displaced relative to the ordinary beam). As mentioned above, coupling beams into fibers is dependent on the correct alignment of beam and FC. This means that one FC is not sufficient to cater for both possible positions of the extraordinary beam. The simple solution is to use two FCs - one for each beam position. As before, however, the two possible positions of the beam are too close together to be coupled into two FCs which stand side by side. To resolve this issue, a second half-wave plate, a second PBS and an additional FC were introduced into the system (depicted in grey in ROI 5 of Fig. 3.1): if the extraordinary beam is *vertically* displaced to the ordinary one, the grey half-wave plate is flipped out of the beam path and the extraordinary beam's polarization remains at 90°. The beam thus passes the grey PBS unimpeded and enters the *white* FC centrally (Fig. 3.7a). If, on the other hand, the extraordinary beam is *horizontally* displaced from the ordinary one, the grey half-wave plate is moved into the beam path using a motorized filter flipper (Thorlabs, MFF001/M). In consequence, the beam's polarization is rotated back to 0°, so that the beam is deflected by the grey PBS and falls centrally onto the *grey* FC in ROI 5 of Fig. 3.1 (cf. Fig. 3.7b). Depending on the orientation of the beams, either the white or the grey FC is connected to the spectrometer.

A potential problem when measuring with more than one measurement beam is the cross-talk, i.e. the amount of light from one beam scattered into the detection channel of another beam. In this setup, cross-talk is minimized both by the spatial separation of the beams as well as by the separation according to polarizations: as discussed in this section, the two beams have different polarization directions and are separated accordingly using polarization-dependent optics. Although the polarization of the beams could be influenced by the retinal layers that do not maintain the polarization (e.g. birefringence in the cornea [29], birefringence in the nerve fibre layer and depolarization in the retinal pigment epithelium [30]), the influence seems to be small enough to be negligible: measurements in which one beam was covered were performed at different position in the retina (amongst others at the macula and optic nerve head); in all of the measurements, the amounts of intensity were below noise level in the covered beam's detection channel, effectively proving that cross-talk was not a problem in the current setup.

3.1.5   Spectrometer
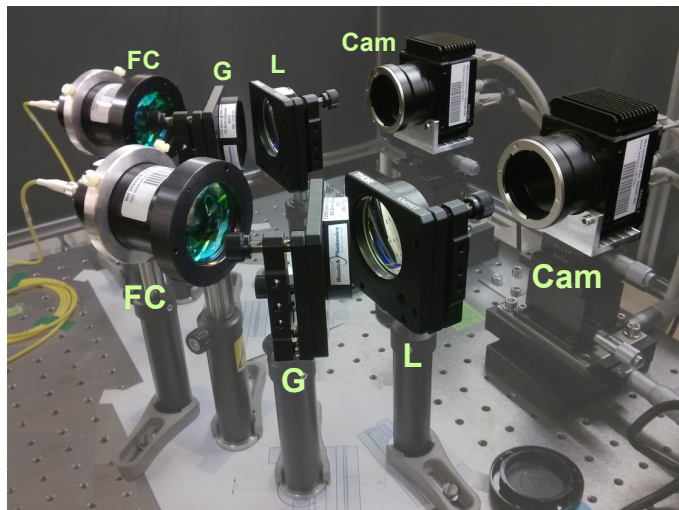
Figure 3.8: Photograph of the two spectrometers, each with its fiber collimator (FC), grating (G), lens (L) and camera (Cam).

As mentioned in section 2.2, FDOCT necessitates measuring the beams' frequency components. This is achieved by using two spectrometers (ROI 6 of Fig. 3.6), one for each beam, which are depicted schematically in ROI 6 in Fig. 3.1. A photograph of the spectrometers can be seen in Fig. 3.8: the spectrometers consist of a collimator (TE Lintelo Systems, HPUCO-23-800/1000-S-100AC-SP), a transmission grating (Wasatch Photonics, 1200 l/mm @ 830nm), a lens (Thorlabs, AC508-150-B-ML) and a line camera (Basler, spL-4096-140km) each. The collimator parallelizes the beam coupled into it from the fiber and directs the beam onto the grating. There, the beam is diffracted according to its wavelength components, and positive and

50
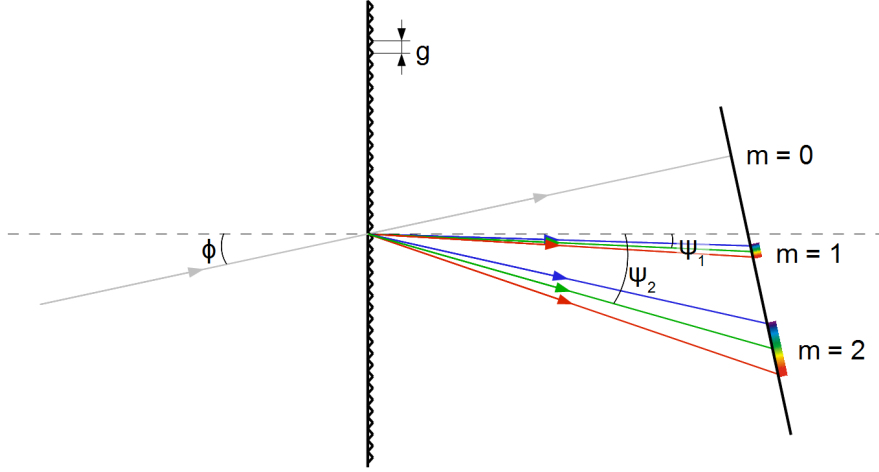
Figure 3.9: Schematic drawing of the dispersion of light falling through a grating.

negative interference will occur. The maxima in the interference pattern occur at angles ψ_m (measured from the surface normal) according to the grating equation,

$$m\lambda = g \cdot (\sin \phi \pm \sin \psi_m), \qquad (3.1)$$

where $m = 0, 1, 2, ...$ is the order of diffraction, λ is the wavelength, g is the grating's line width and ϕ is the angle of the incident beam (see Fig. 3.9).

The lens then focuses the light from the grating onto the CCD-array of the camera. Due to the spectrometers' geometry, the distribution of wavelengths on the cameras' arrays is not entirely equidistant. This can be compensated by rescaling the spectra in the data processing, as will be explained in section A.4.1.

In OCT applications, the first order of diffraction ($m = 1$) is generally used. With the central wavelength of 838.8 nm, the grating with 1200 lines per mm, and the incident angle of $\phi = 30°$, the focussing lens in this system had to be placed at an angle of

$$\psi_1 = \sin^{-1}\left(\frac{\lambda}{g} - \sin \phi\right) = \sin^{-1}\left(\frac{838.8\,\mathrm{nm}}{\frac{1}{1200}\mathrm{mm}} - \sin 30°\right) = 30.4°. \qquad (3.2)$$

3.1.6 System parameters

Several parameters define the system's accuracy and performance. These will be given in the following subsections.

Image resolution

As explained in chapter 2.1.2 and illustrated in Eq. 2.24, the detected intensity I_D depends upon the difference Δz between reference arm length and sample arm length[ii], as

$$I_D(k) \propto \cos(k \cdot 2\Delta z). \tag{3.3}$$

Larger path length differences Δz thus result in faster oscillations of the measured intensity.

The largest path length difference Δz_{max} that an OCT system can record is, consequently, limited by the camera's capacity to resolve high frequencies. As shown in Fig. 3.10, the highest recordable frequency, i.e. the smallest recordable wave vector δk, is reached if the distance between two pixels equals half a wavelength, i.e. if

$$\delta k \cdot 2\Delta z_{\mathrm{max}} = \pi; \tag{3.4}$$

any higher frequencies would be undersampled.
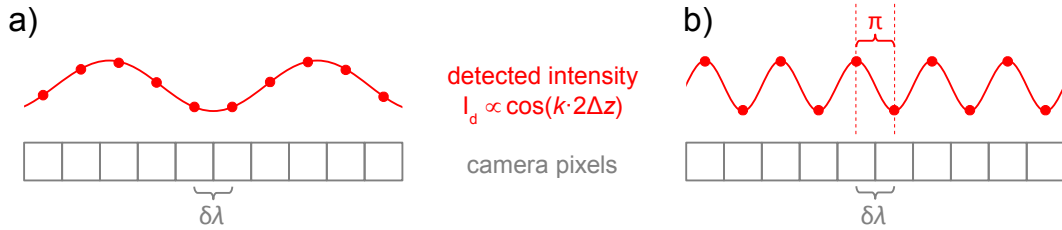
Figure 3.10: Detected intensity on the camera for an arbitrarily chosen path length difference Δz (a) and the largest detectable path length difference Δz_{max} (b).

Differentiating the relation $k = 2\pi/\lambda$ (Eq. 2.43) between wavenumber and wavelength, the smallest recordable wave vector can be calculated as

$$\delta k = -2\pi \frac{\delta\lambda}{\lambda_0{}^2} \quad \Rightarrow \quad |\delta k| = 2\pi \frac{\delta\lambda}{\lambda_0{}^2} \,, \tag{3.5}$$

λ_0 being the system's central wavelength and $\delta\lambda$ being the smallest recordable wavelength difference (i.e. the wavelength difference between two pixels, cf. Fig. 3.10). Combining Eqs. 3.4 and 3.5 then yields (cf. Lee et al. [31])

$$\Delta z_{\mathrm{max}} = \frac{\pi}{2} \cdot \frac{1}{\delta k} = \frac{\pi}{2} \cdot \frac{\lambda_0{}^2}{2\pi \; \delta\lambda} = \frac{\lambda_0{}^2}{4 \; \delta\lambda}. \tag{3.6}$$

However, this equation is only applicable in vacuum. In a medium, the refractive index n has to be taken into account: instead of geometric lengths L, optical lengths

---

[ii]The factor 2 is due to the light having to pass through the interferometer's arms twice, on its way in and its way out.

L/n have to be taken into account. The largest depth range is thus becomes

$$\Delta z_{\text{max}}^{\text{medium}} = \frac{1}{n} \cdot \frac{\lambda_0{}^2}{4\,\delta\lambda}. \tag{3.7}$$

In the system described in this work, the central wavelength λ_0 is 838.8 nm. To calculate the wavelength difference $\delta\lambda$ between two pixels $\delta\lambda$ it is necessary to know that the cameras have 4096 pixels, the maximal wavelength that can be recorded on the camera is 927.13 nm (cf. Eq A.21), and the minimal wavelength can be calculated to be 731.88 nm. $\delta\lambda$ is thus

$$\delta\lambda = \frac{\lambda_{\text{max}} - \lambda_{\text{min}}}{\text{No. of CCD pixels}} = 0.0477\,\text{nm}. \tag{3.8}$$

With the refractive index of blood[iii], $n = 1.37$, the maximal depth range that can be recorded is then

$$\Delta z_{\text{max}}^{\text{blood}} = \frac{1}{1.37} \cdot \frac{838.8\,\text{nm}^2}{4 \cdot 0.0477\,\text{nm}} = 2.69\,\text{mm}. \tag{3.9}$$

With this information, one can express the correspondence between pixels and µm in depth direction of the A-scans: each A-scan has 2048 pixels in depth direction (half of the camera's 4096 pixels, as the Fourier transform is symmetrical around 0 and half of the pixels are thus redundant). As the maximal depth range is 2.69 mm,

$$1\text{px} \mathrel{\hat{=}} \frac{2.69\,\text{mm}}{2048} = 1.3\,\text{µm}. \tag{3.10}$$

However, this is only the *image* resolution in axial direction. The *actual* axial resolution of the system is limited by the physical resolution and will be detailed in the next section.

Axial resolution

In OCT (as opposed to e.g. light microscopy), the axial resolution is decoupled from the transversal resolution. In consequence, a high axial resolution can be achieved, independently of the beam's spot size on the retina.

The axial resolution in low-coherence tomography is given by half the coherence length (the factor $\frac{1}{2}$ being due to the beam travelling the length of the arms twice). It is thus inversely proportional to the bandwidth of the light source source. For a Gaussian spectrum, the axial resolution is given by

$$\delta z = \frac{l_c}{2} = \frac{2\ln 2}{\pi} \frac{\lambda_0^2}{\Delta\lambda}, \tag{3.11}$$

[iii]The refractive indices of the lenses, vitreous humour etc. should be compensated by the dispersion compensating glass block, see section 3.1.3.

where l_c is the coherence length, λ_0 is the central wavelength of the spectrum and $\Delta\lambda$ is the spectral bandwidth (cf. Fujimoto and Drexler [32]).

In the case of the system explained in this work, the central wavelength is 838.8 nm and the bandwidth is 54.0 nm. The axial resolution in vacuum would thus be

$$\delta z_{\text{vac}} = \frac{2\ln 2}{\pi} \cdot \frac{(838.8\,\text{nm})^2}{54.0\,\text{nm}} = 5.8\,\mu\text{m}; \tag{3.12}$$

with a refractive index of blood/tissue of about 1.37, (where, once again, optical and not geometric lengths must be used) the axial resolution becomes

$$\delta z = \delta z_{\text{vac}} \cdot \frac{1}{1.37} = 4.2\,\mu\text{m}. \tag{3.13}$$

Transverse resolution
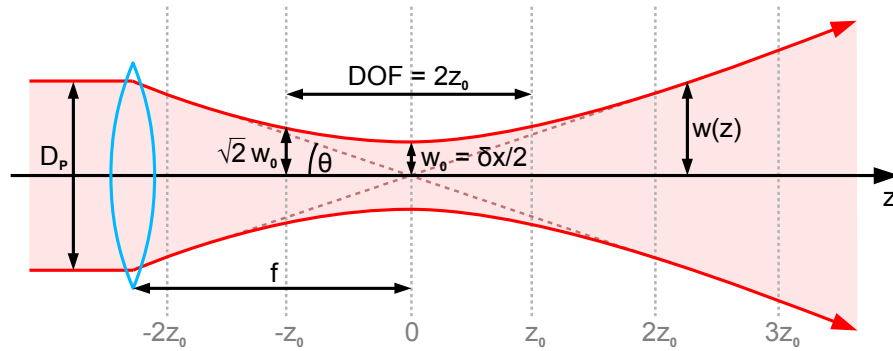
Figure 3.11: Parameters of a Gaussian beam focussed by a lens with focal length f: diameter D_P of the incoming beam, width $w(z)$ of the focussed beam, depth of focus (DOF) and beam waist radius w_0.

For a Gaussian beam, the beam waist w is defined as the distance of the $\frac{1}{e^2}$ drop of the beam's intensity, corresponding to a $\frac{1}{e}$ drop of the beam's amplitude. The transverse resolution δx is determined by the spot size: for a Gaussian beam, δx is defined as twice the minimal beam waist radius w_0:

$$\delta x = 2w_0 = \frac{2\lambda_0}{\pi\theta}, \tag{3.14}$$

where $\tan\theta = D_P/(2f)$ is the divergence of the beam, defined by the beam's collimation diameter D_P and the focal length f of the collimating lens, cf. Fig. 3.11.

To calculate the transverse resolution of the setup described here, it is thus necessary to know the beam's collimation diameter at the pupil: the beam is guided to the system via a fiber (Thorlabs, SM800-5.6-125) with numerical aperture of $NA = 0.12$. To transmit the beam from the fiber into the free-space (i.e. wireless) system, it then

passes a collimator. The one used in the setup described here (TE Lintelo Systems, HPUCO-23-840-S-6.2AS) has a focal length of $f_{\text{coll}} = 6.2\,\text{mm}$. The radius r_{coll} of the collimated beam can be calculated to be

$$r_{\text{coll}} = f_{\text{coll}} \cdot NA = 6.2\,\text{mm} \cdot 0.12 = 0.744\,\text{mm}. \tag{3.15}$$

To reach the pupil, the beam then has to pass the lens system in the setup's sample arm, explained in more detail in section 3.2.5. Using the matrix method (see section A.3), the radius r_P of the beam at the pupil can be calculated:

$$
\begin{aligned}
\begin{pmatrix} r_P \\ \theta_P \end{pmatrix} &= T_{L1,P} \cdot M_{L1} \cdot T_{L2,L1} \cdot M_{L2} \cdot T_{L3,L2} \cdot M_{L3} \begin{pmatrix} r_{\text{coll}} \\ \theta_{\text{coll}} \end{pmatrix} = \\
&= \begin{pmatrix} 1 & 59.87 \\ 0 & 1 \end{pmatrix} \cdot \begin{pmatrix} 1 & 0 \\ -\frac{1}{41.76} & 1 \end{pmatrix} \cdot \begin{pmatrix} 1 & 238.06 \\ 0 & 1 \end{pmatrix} \cdot \\
&\quad \begin{pmatrix} 1 & 0 \\ -\frac{1}{100} & 1 \end{pmatrix} \cdot \begin{pmatrix} 1 & 253.84 \\ 0 & 1 \end{pmatrix} \cdot \begin{pmatrix} 1 & 0 \\ -\frac{1}{50} & 1 \end{pmatrix} \cdot \begin{pmatrix} 0.744 \\ 0 \end{pmatrix} = \begin{pmatrix} 0.645 \\ 0 \end{pmatrix}.
\end{aligned}
\tag{3.16}
$$

The beam's radius at the pupil is thus $r_P = 0.645\,\text{mm}$, making the diameter at the pupil $D_P = 2 \cdot r_P = 1.29\,\text{mm}$. Using Eq. 3.14 with a standard eye length of 24.2 mm, the transversal resolution δx can be calculated to be

$$\delta x = \frac{2\lambda_0}{\pi \arctan \frac{D_P}{2f}} = \frac{2 \cdot 838.8\,\text{nm}}{\pi \arctan \frac{1.29\,\text{mm}}{2 \cdot 24.2\,\text{mm}}} = 20.0\,\text{µm}. \tag{3.17}$$

Depth of focus

The depth of focus (DOF) is defined as twice the distance in which the beam widens from its beam waist radius w_0 to $\sqrt{2}w_0$ (see Fig. 3.11). The DOF can be calculated with the expression [33]

$$\text{DOF} = k \cdot w_0{}^2 = \frac{2\pi \cdot w_0{}^2}{\lambda_0}. \tag{3.18}$$

With Eq. 3.14, this can be written as

$$\text{DOF} = \frac{2\pi \cdot (\delta x/2)^2}{\lambda_0} = \frac{\pi \cdot \delta x^2}{2\lambda_0}, \tag{3.19}$$

which, with Eq. 3.17, yields

$$\text{DOF} = 0.75\,\text{mm}. \tag{3.20}$$

Oversampling factor

As mentioned in section 2.3, the velocity in Doppler OCT measurements is calculated from the phase shift between two successive measurements. In practice, when

recording cross-sectional images, these two measurements are not recorded at the same sample point, but at adjacent points. If the distance between the two adjacent points is too high, the signals from the two points will be decorrelated – random phase variations will thus occur, which will overlay any phase differences induced by movements in the sample. Consequently, it is important to maintain a high degree of lateral oversampling [34]. On the other hand, especially when measuring in vivo, too high oversampling will result in overly long measurement times. It is thus necessary to find the best trade-off between measurement time and decorrelation.

According to Singh et al. [35], the oversampling factor (OF) of a tomogram can be defined as

$$OF = \frac{\delta x \cdot N}{D},$$

(3.21)

where δx is the spot size, N the number of sampling points and D the geometric width of the tomogram. With the spot size of $20.0\,\mu m$ calculated in Eq. 3.17, the 3000 sampling points used in most of the measurements presented here and a geometric width of approximately $3900\,\mu m$, the oversampling factor can be calculated to be

$$OF \approx \frac{20.0\,\mu m \cdot 3000}{3900\,\mu m} \approx 15.$$

(3.22)

This means that the lateral distance between two imaged sample points is 1/15 of the beam width. According to Park et al. [36], the standard deviation of the phase differences for this sampling ratio lies below $0.3\,rad$, which is certainly low enough to be neglected.

3.2 Integration of the DVA into the setup

3.2.1 Motivation

Using Doppler OCT, one can determine the velocity of blood flowing in the eye's vessels. To determine the flow Q, however, the velocity alone is not enough: it is also necessary to know the diameter D of the vessels at the time of the measurement. The exact determination of the diameter is of high importance, as the vessel diameter enters quadratically into the calculation of the flow:

$$Q = \frac{vD^2\pi}{4}.$$

(3.23)

A frequently used approach to determine the diameter is via the OCT images: as explained in section 3.1.6, the OCT's maximal depth range z_{max} depends only on the

spectrometer's central wavelength, its wavelength resolution, and the medium's index of refraction. For images with 2048 pixels, one pixel then corresponds to 1.3 µm depth.[iv] It is thus possible to determine the vessel diameters from the OCT images. However, axial resolution limits the possible accuracy of the diameter determination. Moreover, the high absorption by the blood cells result in shadowing effects behind the vessels, obscuring the rear vessel walls' positions and multiple scattering will obscure the vessel's rear wall even further. These effects may lead to an underestimation of the vessel diameter. Furthermore, the parabolic flow velocities decrease rapidly close to the vessels' walls. At some point, the phase values are no longer distinguishable from the background noise, rendering the exact determination of the diameter difficult. In addition, the cell-depleted layer which forms along the walls of vessels [37] does not show on OCT images, and may thus lead to a further underestimation of the vessel diameter. One way to avoid this underestimation is using fundus photos instead of the OCT images to determine the diameters, as was done in a number of earlier studies [1, 16, 38–40]. Significantly more exact results, however, can be achieved by using a DVA [41]. This instrument will be described in more detail in the following.

3.2.2 The Dynamic Vessel Analyzer

The Dynamic Vessel Analyzer is a device that allows measuring vessel diameters. As opposed to static vessel analysis systems, it can measure the diameters not only as a function of place, but also as a function of time in a live or recorded video.

The DVA is a product of the company Imedos Systems UG (Jena, Germany) and consists of a modified fundus camera (FF450, Carl Zeiss Meditec AG, Jena, Germany), a CCD-camera (CF 8/5 MX, Kappa optronics GmbH, Gleichen, Germany) for recording high-quality fundus images, and software (Visualis, Imedos Systems UG, Jena, Germany) using complex algorithms to determine the vessel diameters very precisely. Fig. 3.12 shows a photograph of a DVA system.

3.2.3 Coupling of the optical paths

To integrate the DVA into the OCT system, one can make use of the fact that the DVA uses visible light for measuring, while the OCT uses near infrared light. A hot mirror (Edmund Optics, NT64-471), which reflects infrared and transmits visible light, can thus be used to couple the OCT beam into the DVA. The most obvious position for the hot mirror would be to place it between the DVA's ophthalmoscope lens and the eye. However, the space between lens and eye is too small to allow this.

[iv]As mentioned above, this is only the image resolution; the actual axial resolution of the system is limited by the physical resolution, which is 4.2 µm (cf. Eq. 3.13).

Figure 3.12: Photograph of a DVA system with fundus camera and evaluation hard- and software components (image provided by Imedos systems UG).

The hot mirror, consequently, has to be placed *before* the DVA's ophthalmoscope lens (i.e. inside the DVA's housing, see Fig. 3.13); this entails that the lens system of the OCT setup has to be designed to integrate this DVA lens. The calculations necessary to determine the lens requirements for such a combined system are given in the following.
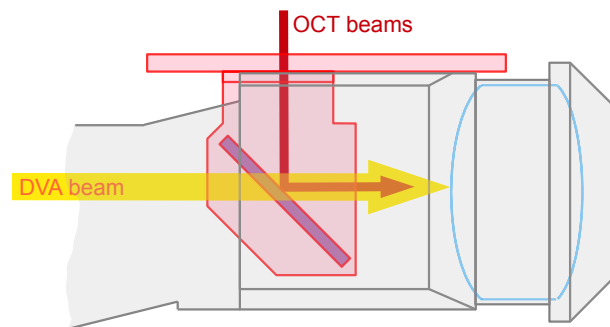
Figure 3.13: DVA in side view (grey) with its ophthalmoscope lens (blue) and the hot mirror (purple) in a specifically designed mirror holder (red). The DVA beam (visible light; yellow arrow) passes the hot mirror unimpeded while the OCT beam (infrared light, red arrow) is reflected.

3.2.4 Properties of the DVA's lens

The front lens, or ophthalmoscope lens, of the DVA's fundus camera is a thick aspheric lens consisting of several cemented lenses. Hence, the equations used for ideally thin lenses are not applicable. Nevertheless, it is necessary to be able to include the lens in the calculations of the optical system, as it has to be integrated into the OCT's lens system (cf. section 3.2.3). This can be accomplished by using the equations for tick lenses, explained in section A.2.

Setup and distances of the fundus camera

The setup of the FF450, the DVA's fundus camera, with the distances between the different planes is depicted in Fig. 3.14. Here, F and F' denote fundus planes. P and P' denote pupil planes. $L1$ is the lens with its principal planes H_1 and H_2 and its vertices S_1 and S_2 (cf. section A.2). The distances h_1 and h_2 are those between a principal plane and its respective vertex.
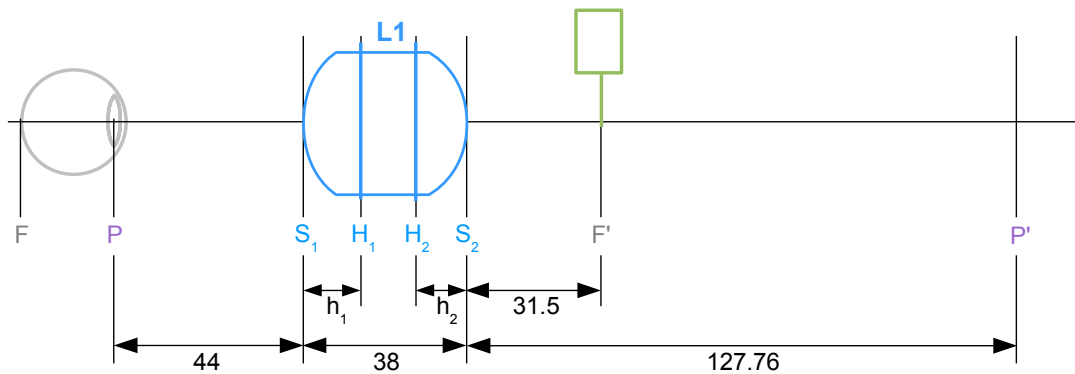
Figure 3.14: Distances between the fundus planes (F, F'), pupil planes (P, P') and the ophthalmoscope lens's principal planes (H_1, H_2) and vertices (S_1, S_2) in the fundus camera FF450. All lengths given in mm.

Shown in green in Fig. 3.14 is the fixation target. It consists of a red LED and a light conductor, mounted so that it can be moved by the DVA's operator. The pointed end of the light conductor lies in the fundus plane F', so that it is focussed on the eye's fundus. By asking the measured subjects to fixate the fixation target and moving it around, the intended measurement position on the subjects' fundus can be brought into the DVA's field of view.

Ophthalmoscope lens: principal plane distance h_2

To be able to include the ophthalmoscope lens in the lens system, it's principal planes must be known. These can be calculated, as the focal points of the lens are known from the setup of the DVA and the thickness of the lens was measured using a sliding calliper.

Objects in the focal plane F' (such as the fixation target) must also be focussed on the eye's fundus. The ophthalmoscope lens must thus parallelize beams from F', so that they will be focussed by the eye's lens. Parallel beams arise if the object distance is infinite. The equation linking object distance, image distance and focal lengths for thick lenses is explained in appendix A.2. For an infinite object distance, $a = \infty$, the thick lens equation (Eq. A.2) can be simplified to

$$\frac{1}{f} = \frac{1}{b} \quad \Rightarrow \quad f = b, \tag{3.24}$$

with

$$b = \overline{H_2 F'} = \overline{H_2 S_2} + \overline{S_2 F'} = h_2 + \overline{S_2 F'}. \tag{3.25}$$

The distance h_2 of the principal plane H_2 form the vertex S_2 of the lens is thus

$$h_2 = b - \overline{S_2 F'} = f - \overline{S_2 F'}. \tag{3.26}$$

In this setup, $\overline{S_2 F'} = 31.5\,\text{mm}$ and $f = 41.76\,\text{mm}$. It follows that

$$h_2 = 41.76\,\text{mm} - 31.5\,\text{mm} = 10.26\,\text{mm}. \tag{3.27}$$

Ophthalmoscope lens: principal plane distance h_1

For the image of an object to lie in P', the object must lie in P. With $\overline{PS_1} = 44\,\text{mm}$, the object distance a is

$$a = \overline{PH_1} = \overline{PS_1} + \overline{S_1 H_1} = 44\,\text{mm} + h_1, \tag{3.28}$$

and, with $\overline{S_2 P'} = 127.76\,\text{mm}$ and Eq. (3.27), the image distance b is

$$b = 127.76\,\text{mm} + h_2 = 127.76\,\text{mm} + 10.26\,\text{mm} = 138.02\,\text{mm}. \tag{3.29}$$

Rewriting Eq. A.2 for a and equating it with (3.28) gives

$$a = \frac{b \cdot f}{b - f} = 44\,\text{mm} + h_1 \quad \Rightarrow \quad h_1 = \frac{b \cdot f}{b - f} - 44\,\text{mm}. \tag{3.30}$$

Inserting b from Eq. (3.29) and setting $f = 41.76\,\text{mm}$ yields

$$h_1 = 15.87\,\text{mm}. \tag{3.31}$$

Ophthalmoscope lens: thin lens equivalent

With the distances of the principal planes, it is possible to find the thin lens equivalent for the thick ophthalmoscope lens. As mentioned in section A.2, this is done by adjusting the distances (i.e. by adding h_1 and h_2 to the respective lengths) and disregarding the distance $\overline{H_1 H_2}$ between the principal planes. The resulting parameters are given in Fig. 3.15.
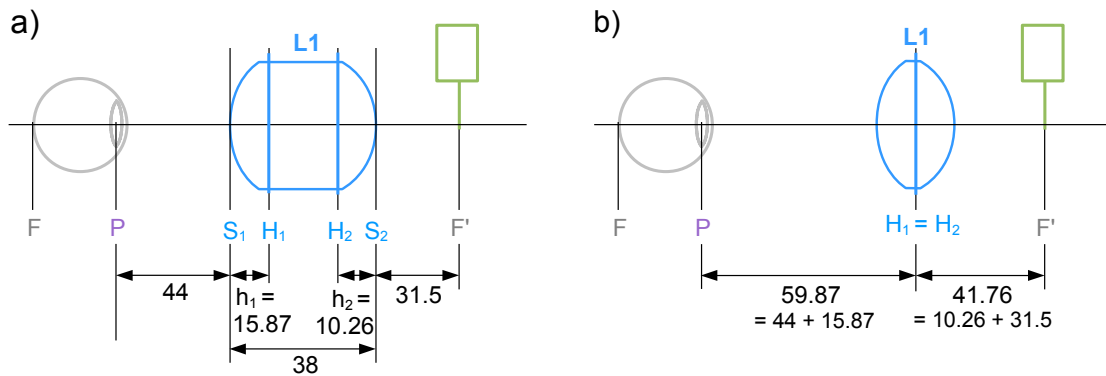
Figure 3.15: Distances for the ophthalmoscope lens (a) and its thin lens equivalent (b) with fundus planes (F, F'), pupil plane (P), the ophthalmoscope lens ($L1$), and its principal planes (H_1, H_2) and vertices (S_1, S_2). All distances are given in mm.

3.2.5   Lens system

Prerequisites

To combine the OCT system with the DVA, lens L1 is not enough. This is due to the fact that in the OCT system, the two beams exit the scanner parallelly and have to reach the eye parallelly: only then will they be focused on the fundus by the eye's optical system. Furthermore, the scanner has to be in one of the pupil planes, so that the beams enter the narrow pupil at all times, independently of the scanning position (see Fig. 3.16a). If the scanner is not positioned in a pupil plane, the turning point of the beams will not lie in the pupil and only central rays will be able to enter, as is shown in Fig. 3.16b.

There are thus two prerequisites the lens system has to fulfil:

- Prerequisite 1: the beams must be parallel at the scanner *and* at the pupil.

- Prerequisite 2: the scanner must be in a pupil plane.

61
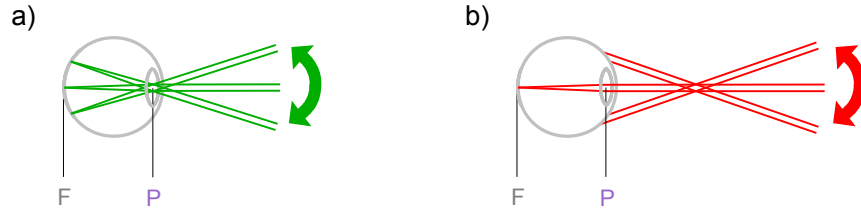
Figure 3.16: Path of rays depending on the scanner position: a) if the scanner is in a pupil plane, all rays are transmitted through the eye's pupil in the plane P and reach the fundus in the plane F; b) if the scanner is not in a pupil plane, scanning will result in some rays being cut off.

For a better understanding, the two points are explained graphically: Fig. 3.17a illustrates the first prerequisite, namely that the OCT beams (red) coming from the scanner (labelled "Sc") are parallel to each other, pass a lens or lens system (labelled with the question mark, as it is yet to be determined) and reach the eye still being parallel to each other. Fig. 3.17b illustrates the second prerequisite, i.e. that the scanner has to be in a pupil plane. To visualize the pupil planes, an auxiliary construction is used: auxiliary beams coming from the pupil (shown in purple in Fig. 3.17) are drawn; their crossings mark the pupil planes (i.e. P, P', and P'').

The easiest way to place the scanner in a pupil plane (where, according to prerequisite 2, it must be) would have been to place it in the plane P', dispensing of any additional lenses. However, the first prerequisite requires the beams to be parallel at the scanner; as can be seen in Fig. 3.17a, this is not the case in P'. Consequently, an additional lens or lens system had to be included into the system.
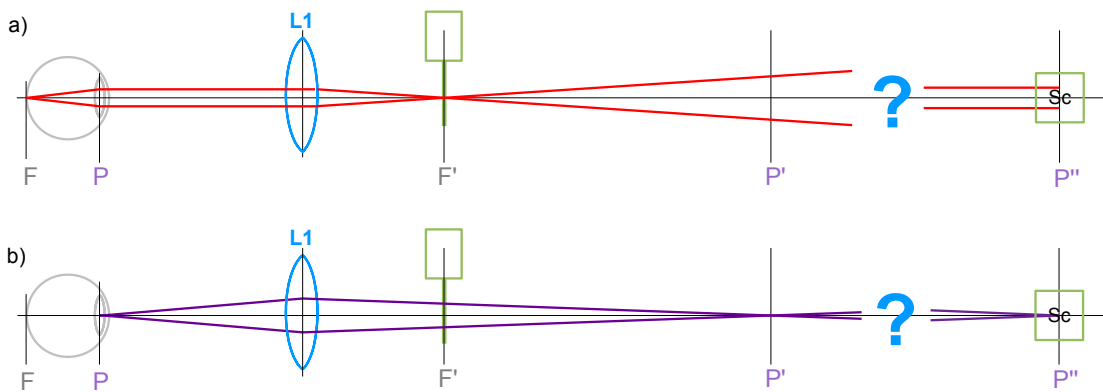
Figure 3.17: Prerequisites for combining OCT with a DVA: beams must exit the scanner and reach the eye parallelly (a) and the scanner must be located in a pupil plane (b).

62

Calculation of the lens system with two additional lenses

As one additional lens is not sufficient to fulfil the prerequisites mentioned earlier,[v] a *lens system* has to be introduced. The easiest lens system is made up of two lenses; this is sufficient for solving the problem at hand, as will be shown in the following.

A schematic image of the problem, including the lengths determined for the thin lens equivalent of the ophthalmoscope lens in section 3.2.4 and the lengths A, b and C in the lens system (which are yet to be calculated) are shown in Fig. 3.18.
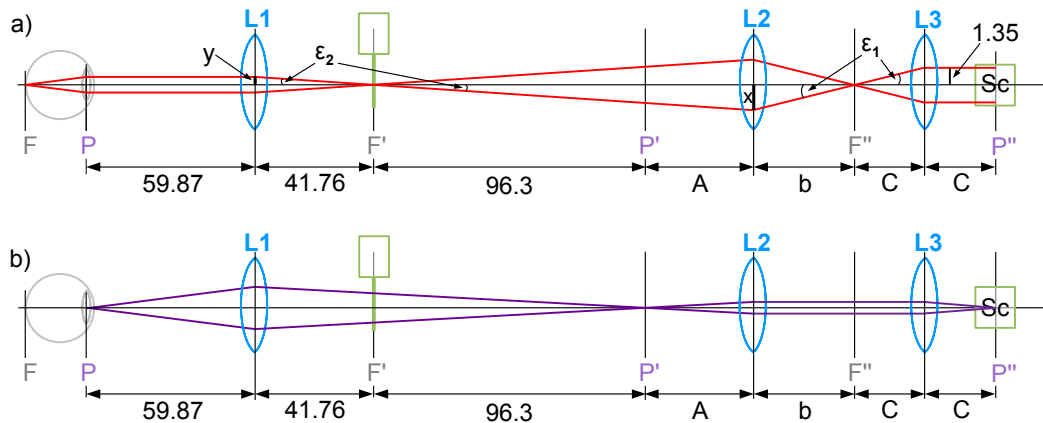
Figure 3.18: Necessary distances in the lens system due to the prerequisites for a) fundus beams; b) auxiliary construction: pupil beams. All lengths are given in mm.

A range of new variables is introduced in Fig. 3.18:

A, C	...	focal lengths of $L2$ and $L3$, respectively
b	...	distance between lens $L2$ and focal plane F''
ε_1	...	angle of the fundus beams to the optical axis between $L2$ and $L3$
ε_2	...	angle of the fundus beams to the optical axis between $L1$ and $L2$
x	...	distance of the fundus beams from the optical axis in $L2$
y	...	distance of the fundus beams from the optical axis in $L1$

---

[v]To fulfil both prerequisites with one additional lens, the scanner could be positioned in the pupil plane P' and the lens between F' and P'. The focal length of the lens would then have to equal its distance to F' for it to focus the parallel beams from the scanner at F' (cf. Fig. 3.17a). However, this would move the pupil plane P' so close to the lens that it would no longer be possible to position the scanner there.

The other possibility would be to place the scanner in P'' and the lens between the pupil planes P' and P''. The focal length of the lens would still have to equal its distance to F' (to focus the parallel beams from the scanner). However, this would place P' inside the focal length; the diverging auxiliary beams (see Fig. 3.17b) from P' could thus not be focussed at P''. Consequently, one additional lens alone is not enough to solve the problem.

The focal lengths A and C of the lenses $L2$ and $L3$, respectively, have to be chosen such that they induce the desired magnification of the beam displacement: coming from the scanner, the beams are displaced by $2.7\,\mathrm{mm}$; the distance of each beam from the optical axis is thus $1.35\,\mathrm{mm}$ (see Fig. 3.18). The displacement at the eye should be between two and three millimetres; for each beams' distance from the optical axis, y, this yields

$$2\,\mathrm{mm} < 2y < 3\,\mathrm{mm} \quad \Rightarrow \quad 1\,\mathrm{mm} < y < 1.5\,\mathrm{mm}. \tag{3.32}$$

Expressing y in terms of A and C and taking into account Eq. (3.32) enables choosing the correct lenses $L2$ and $L3$. This will be done in the following.

The distance b between the lens $L2$ and the focal plane F'' can be calculated from the equation for thin lenses,

$$\frac{1}{f} = \frac{1}{g} + \frac{1}{b}, \tag{3.33}$$

where f is the focal length of the lens, g is the object distance, and b is the image distance. The focal length of $L2$ being $f = A$ and the distance of the object (namely the focal plane F') being $g = 96.3\,\mathrm{mm} + A$, this results in

$$b = \frac{g \cdot f}{g - f} = \frac{(96.3\,\mathrm{mm} + A) \cdot A}{(96.3\,\mathrm{mm} + A) - A} = \frac{(96.3\,\mathrm{mm} + A) \cdot A}{96.3\,\mathrm{mm}}. \tag{3.34}$$

The length x, i.e. the distance of the beams from the optical axis in lens $L2$, can be calculated from the two equations

$$\tan \varepsilon_1 = \frac{x}{b} \quad \Rightarrow \quad x = b \cdot \tan \varepsilon_1 \tag{3.35}$$

$$\tan \varepsilon_1 = \frac{1.35}{C} \tag{3.36}$$

to yield

$$x = b \cdot \frac{1.35}{C}. \tag{3.37}$$

Finally, to arrive at an equation for the distance y between the optical axis and the beam, one needs the following relations:

$$\tan \varepsilon_2 = \frac{y}{41.76} \quad \Rightarrow \quad y = 41.76 \cdot \tan \varepsilon_2 \tag{3.38}$$

$$\tan \varepsilon_2 = \frac{x}{96.3 + A}. \tag{3.39}$$

The distance y can thus be written as

$$y = 41.76 \cdot \frac{x}{96.3 + A}. \tag{3.40}$$

Combining this equation with Eqs. (3.34) and (3.37) yields

$$y = 41.76 \cdot \frac{b \cdot \frac{1.35}{C}}{96.3 + A} =$$

$$= 41.76 \cdot \frac{\frac{(96.3+A) \cdot A}{96.3} \cdot \frac{1.35}{C}}{96.3 + A} =$$

$$= \frac{41.76 \cdot 1.35}{96.3} \cdot \frac{A}{C} =$$

$$= 0.58542 \cdot \frac{A}{C} . \tag{3.41}$$

The remaining difficulty now is to find values for A and C that match commercially available lenses and fulfil the condition stated in Eq. (3.32), namely that the value of y is between 1 and 1.5 mm. A number of values for A and C fulfil these prerequisites. However, there is a further condition for A and C, concerning not the sample arm itself, but the reference arm: in the OCT system, the complete sample arm length l_S has to be equal to the reference arm length l_R:

$$l_R = l_S. \tag{3.42}$$

The complete sample arm length is the distance between the eye's fundus and the beam splitter that separates sample-beam and reference-beam. What is meant here is the *actual* (optical) length in space; thus, one cannot disregard the thickness of the lens $L1$ or replace it by the distance to its principal planes, as was done above (cf. Fig. 3.15). Instead, one has to use the distance to the lens' first vertex S_1, the real value of thickness d_{L1} (which is 38 mm, as can be seen from Fig. 3.14) multiplied with the refractive index n of the lens to yield the optical thickness of the lens, and the distance from the second vertex S_2 to the beamsplitter.[vi] A complete drawing of the sample arm with correct true distances is given in Fig. 3.19.
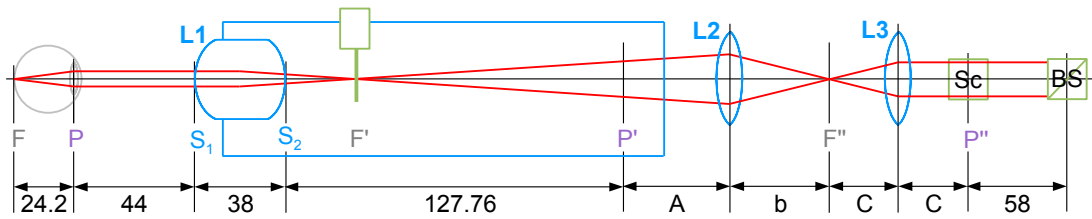
Figure 3.19: Actual distances in the sample arm (distance between principal planes included). All lengths are given in mm.

[vi]If one wanted to be precise, one would also have to include the optical thickness of the two thinner lenses $L2$ and $L3$, which were disregarded in this approximation.

Given		Resulting	
A	C	y	l_R
100	50	1.17	726
75	40	1.09	609
75	35	1.25	599
60	35	1.00	547

Table 3.1: Possible values for the focal lengths A and C and the resulting distance y from the beams to the optical axis and reference arm length l_R. All values are given in mm.

As the length of the sample arm must be equal to the length of the reference arm (cf. Eq. (3.42)), the length of the arms is

$$l_R = l_S = l_{Eye} + l_{Eye-S_1} + d_{L1} \cdot n + l_{S_2-P'} + A + b + 2 \cdot C + l_{Sc-BS}, \qquad (3.43)$$

where l_R is the reference arm length and l_S is the sample arm length; l_{Eye} is the eye length (24.2 mm in the Gullstrand eye model [42]); l_{Eye-S1} is the distance to the front surface vertex S_1 of the first lens $L1$, which was measured to be about 44 mm in the FF450; $d_{L1} = 38$ mm is the thickness of lens $L1$; n is the refractive index of the lens, assumed to be 1.7[vii]; $l_{S_2-P'} = 127.76$ mm is the distance from S_2, the rear surface vertex of $L1$, to the image of the pupil plane; A and C are the distances which are to be determined; b can be calculated with Eq. 3.34; $l_{Sc-BS} = 58$ mm is the distance the light travels from entering the scanner to reaching the centre of the beam splitter (i.e. 11 mm between the two mirrors of the scanner and about 47 mm from the second mirror to the beam splitter). Eq. 3.43 can thus be written as

$$l_R = l_S = 24.2 + 44 + 38 \cdot 1.7 + 127.76 + A + b + 2C + 58. \qquad (3.44)$$

The reference arm of the presented setup in its current state can be extended to around 730 mm, i.e. $l_R \leqslant 730$ mm. Possible combinations of A and C fulfilling all the conditions explained above are e.g. the ones given in Table 3.1.

The values finally chosen were

$$A = 100 \, \text{mm} \qquad (3.45)$$
$$C = 50 \, \text{mm}. \qquad (3.46)$$

[vii]The exact data of the lens were not available, as the fundus camera is a commercially available product underlying trade secrets. 1.7 was assumed as it is a plausible value for achromatic glass lenses.

3.2.6 Spatial considerations – scanning

Not only do the distances and focal lengths need to be considered, but also the beams' path during scanning: in every scanning position, the beams need to pass through all the lenses and other spatially restricting components. To ensure that this is the case with the chosen focal lengths for the lenses $L2$ and $L3$ and the given lens $L1$, the matrix method (see section A.3) was used to calculate the paths of the rays.

Application of the matrix method

In the system sketched in Fig. 3.18, the beam exits the scanner (Sc) with a distance of $r_1 = 1.35\,\text{mm}$ from the optical axis and an angle θ depending on the position of scanning. It then covers the distance C and passes through the lens $L3$, covers the distance $b+C$ and passes through $L2$, covers the distance $A+96.3\,\text{mm}+41.76\,\text{mm} = A + 138.06\,\text{mm}$ and passes through $L1$, then covers the distance $59.87\,\text{mm}$ and passes through the eye's lens, and finally it covers the diameter of the eye (about $24.2\,\text{mm}$ [42]) and reaches the fundus. Consequently, the equation for this system is

$$\begin{pmatrix} r_2 \\ \theta_2 \end{pmatrix} = T_{eye}\, M_{eye}\, T_{L1,L_{eye}}\, M_{L1}\, T_{L2,L1}\, M_{L2}\, T_{L3,L2}\, M_{L3}\, T_{Sc,L3} \begin{pmatrix} r_1 \\ \theta_1 \end{pmatrix}, \qquad (3.47)$$

with $r_1 = 1.35\,\text{mm}$ and

$$
\begin{aligned}
T_{eye} &= \begin{pmatrix} 1 & 24.2 \\ 0 & 1 \end{pmatrix} & M_{eye} &= \begin{pmatrix} 1 & 0 \\ -\frac{1}{24.2} & 1 \end{pmatrix} \\[2mm]
T_{L1,L_{eye}} &= \begin{pmatrix} 1 & 59.87 \\ 0 & 1 \end{pmatrix} & M_{L1} &= \begin{pmatrix} 1 & 0 \\ -\frac{1}{41.76} & 1 \end{pmatrix} \\[2mm]
T_{L2,L1} &= \begin{pmatrix} 1 & 138.06 + A \\ 0 & 1 \end{pmatrix} & M_{L2} &= \begin{pmatrix} 1 & 0 \\ -\frac{1}{A} & 1 \end{pmatrix} \\[2mm]
T_{L3,L2} &= \begin{pmatrix} 1 & b+C \\ 0 & 1 \end{pmatrix} & M_{L3} &= \begin{pmatrix} 1 & 0 \\ -\frac{1}{C} & 1 \end{pmatrix} \\[2mm]
T_{Sc,L3} &= \begin{pmatrix} 1 & C \\ 0 & 1 \end{pmatrix}.
\end{aligned}
\qquad (3.48)
$$

As mentioned in Eqs. (3.45) and (3.46), the focal lengths A and C of the lenses $L2$ and $L3$, respectively, were chosen to be

$$A = 100\,\text{mm}\ ,\ C = 50\,\text{mm}.$$

Therefore, Eq. (3.34) yields

$$b = \frac{(96.3 + A) \cdot A}{96.3} = 203.84 \, \text{mm}. \tag{3.49}$$

It is now possible to determine the angle θ_1 for a certain distance r_2 from the optical axis on the fundus of the eye, i.e. for a certain size of the region of interest in the eye. If this region of interest is, e.g., a square of $6 \, \text{mm} \times 6 \, \text{mm}$, then $r_2 = 6/2 = 3 \, \text{mm}$. Inserting this value into Eq. (3.47) and solving for θ_1 gives

$$\begin{pmatrix} 3 \\ \theta_2 \end{pmatrix} = T_{eye} \, M_{eye} \, \dots \, T_{Sc,L3} \begin{pmatrix} 1.35 \\ \theta_1 \end{pmatrix} \quad \Rightarrow \quad \theta_1 = 6.16° \tag{3.50}$$

after converting the value for θ_1, which is given in radians in the equation, to degrees.

Using a certain value for θ_1 and evaluating Eq. (3.47) up to a certain point gives the beam's angle and distance from the optical axis at this point. Thus, the complete path of the beam can be calculated. This is exactly what we had set out to do at the beginning of this section, as it enables us to determine whether the beam path exceeds the spatial restrictions of the system. The position of the beam path was calculated for the angle found in Eq. st(3.50), i.e. $\theta_1 = 6.16°$ and for $A = 100 \, \text{mm}$, $b = 203.84 \, \text{mm}$ and $C = 50 \, \text{mm}$, and then plotted. The result is shown in Fig. 3.20 with a tenfold enlargement of the scale of the y-scale compared to the x-scale, to make the details more easily visible.
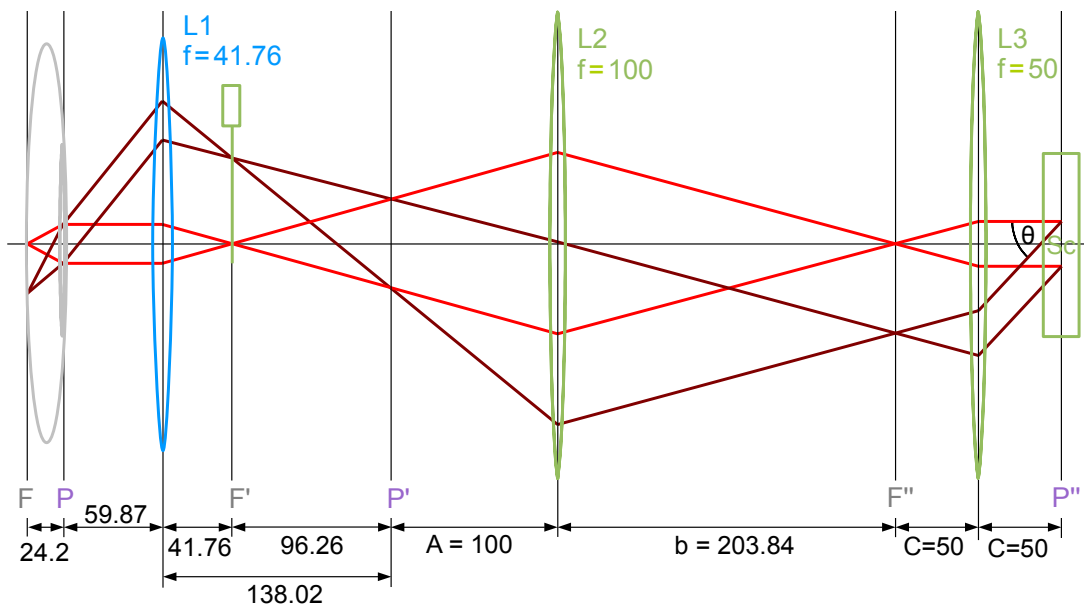
Figure 3.20: Beams without deflection (red) and with an incident deflection of 6.16° (brown). All values are given in mm; the lenses are larger than the depicted area and thus not to scale.

Possible spatial restrictions for the beam would follow from the diameters of the optical components in the beam; however, the dimensions of components and housings and were found to be sufficient in all places of the beam path.

3.3   Complete experimental setup

The complete setup includes the components of the OCT (cf. section 3.1 and Fig. 3.1) as well as the DVA (cf. section 3.2) and the required lens system (cf. section 3.2.5). A schematic of the final setup with beam paths is depicted in Fig. 3.21.

Fig. 3.22 shows a photograph of the setup (with the exception of the DVA, which stands to the right of the depicted area, and the spectrometers, which are shown in Fig. 3.8). The photograph is overlaid with sketch visualizing the beam paths (ordinary beam shown in red, extraordinary beam shown in orange).
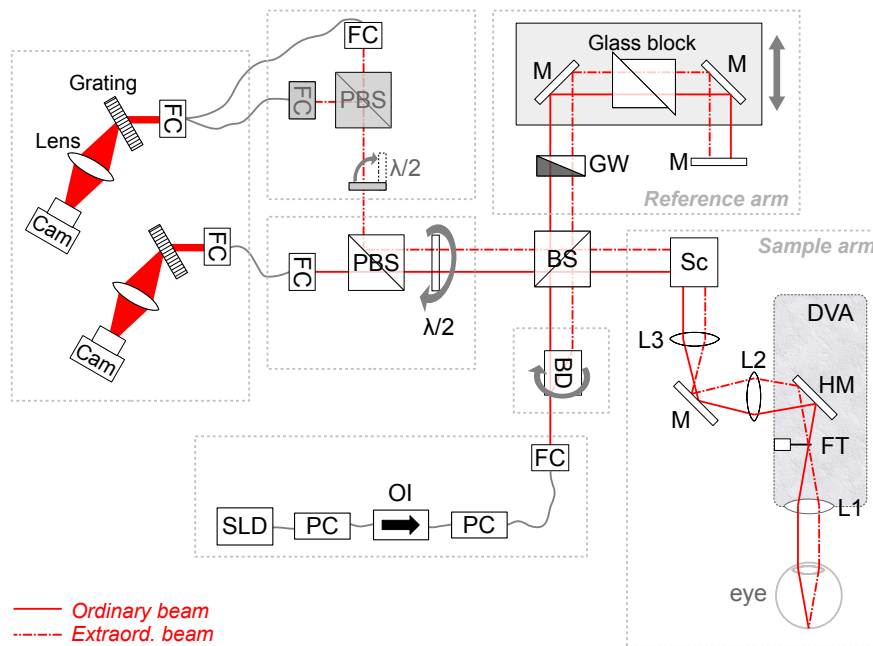
Figure 3.21: Schematic drawing of the complete setup with OCT and DVA. BD = beam displacer, Cam = camera, FC = fiber collimator, FT = fixation target, GW = grey wedge, HM = hot mirror, L = lens, $\lambda/2$ = halfwave-plate, M = mirror, OI = optical isolator, (P)BS = (polarizing) beam splitter, PC = polarization controller, Sc = scanner, SLD = superluminescent diode.
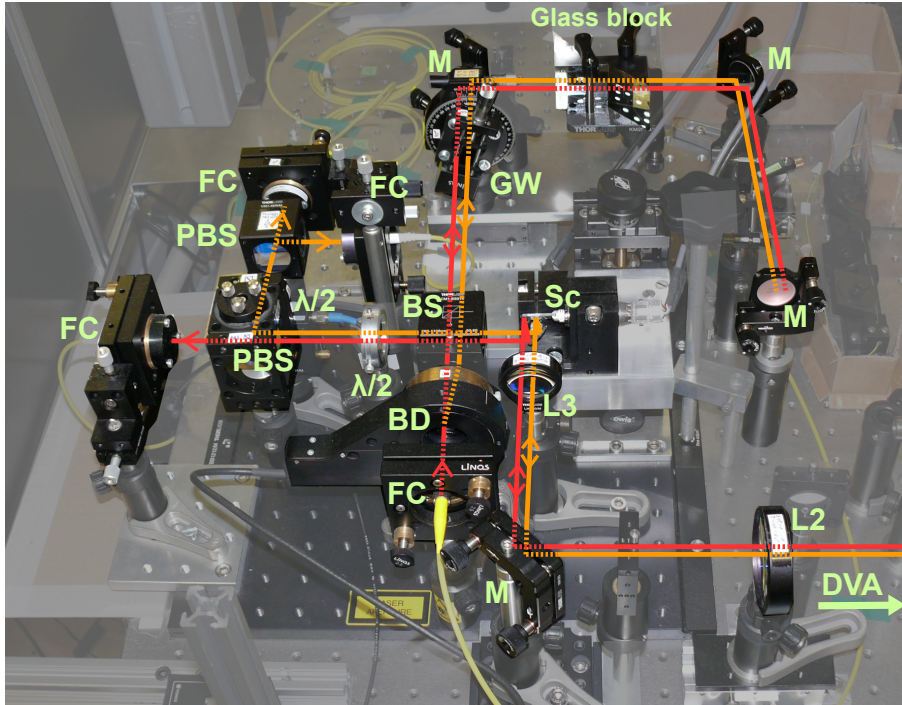
Figure 3.22: Photograph of the interferometer with sketched beams (red: ordinary beam, orange: extraordinary beam). BD = beam displacer, FC = fiber collimator, GW = grey wedge, L = lens, $\lambda/2$ = halfwave-plate, M = mirror, (P)BS = (polarizing) beam splitter, Sc = scanner.

3.4 Comparison with other systems

As mentioned in the introduction, there is hope that measuring the retinal blood flow will further the understanding of a number of ocular diseases. As Doppler OCT is a useful tool to determine absolute retinal blood flow velocities, a number of approaches differing from the one described above were developed using this measurement technique.

One of the possible approaches to measure absolute flow values with OCT is a modification of single beam method discussed in section 2.3.1. As mentioned in that section, only the velocity component in direction of the beam can be detected with single beam OCT; to calculate absolute velocity values, the Doppler angle δ must be estimated. A possible circumvention of this problem was suggested by Pedersen et al. [43] and Ahn et al. [44]: they presented a method to obtain absolute flow velocities with a single beam OCT system by delaying parts of the beam through the insertion of glass plates. Thus, the different parts of the single beam, illuminating the sample under different angles, could be distinguished by their different optical path lengths. Effectively, this gave three [43] to five [44] different k-vectors (i.e. a triple or pentuple beam system), which allowed measuring absolute flow values in arbitrarily oriented vessels. The feasibility of this approach was shown in vitro on

flow phantoms. The drawback of the method compared to the system presented in this thesis is the reduction of the depth range of the OCT-system. This is due to the fact that OCT systems have a maximal recordable depth range which depends on the spectrometer's characteristics (see Eq. 3.7); by intentionally introducing additional path length differences which are all measured with the same spectrometer, the effective depth range is strongly reduced. This limitation is problematic in vivo, where the depth range must be high enough to allow a certain range of movement while still imaging all relevant retinal layers.

Another approach to determine absolute flow values with a single beam system was suggested by Wang et al. [45]. In this method, the scanning pattern consisted of two concentric circles. By comparing the position of the measured vessels in both of the scans, it was possible to determine the Doppler angle and compute absolute velocity values. The method has the advantage of being relatively fast (a complete measurement was reported to take only 2 s [45]). The applicability of the method in vivo was reported in a number of publications on healthy and diseased patients [45–47]. However, the area in which the method can be applied in the eye is limited, as – effectively conducting two single beam measurements – only the component in beam direction could be measured, and the velocities in vessels with an angle of 90° to the beams cannot be measured. This problem could be solved by a reasonable choice of the measurement area (close to the optic disc, the vessels slope out of the eye, cf. section 5.1.1), but it still limits the measurable range. Additionally, bifurcations or bends of the vessels are not catered for – for the calculation of the velocity, the vessels are assumed to run straight and unbranching within the two measured circles. Moreover, a constant distance between the circle is presumed. As the two circles are not recorded simultaneously (contrarily to the dual beam method applied in the work presented here, where both beams impinge onto the sample concurrently), movements in the course of the recording result in incorrect values.

Instead of *determining* the Doppler angle, Baumann et al. [48] presented a method that *eliminates* the dependence on the Doppler angle, while still using a single beam system. This is possible via the *en-face* cross section: usually, the velocity component in beam direction is measured, converted to the absolute velocity (via the Doppler angle) and then multiplied with the vessel's cross section to yield the flow. What is measured in the method proposed by Baumann et al. is also the velocity in direction of the beam. However, it is not converted to the absolute velocity and multiplied with the cross-section. Rather, the measured velocity in beam direction is directly multiplied with the *en-face* cross-section of the vessel. As the dependence of the *en-face* cross-section on the Doppler angle is inverse to that of the velocity in beam direction, the Doppler angle is eliminated from the calculation. The method is thus capable of measuring absolute flow velocities without the necessity to estimate or measure the Doppler angle. Moreover, via the use of swept-source lasers, the method is extremely fast, enabling the recording of volumetric images. As the

method relies on Doppler shifts in a single beam, however, it underlies the same restrictions as mentioned with reference to the system by Wang et al. [45]: velocities in vessels with an angle of 90° to the beams cannot be measured. The method is thus employed in the vessels sloping into the optic disc, but is not readily applicable in the areas measured by the system presented here (cf. section 5.4.1 on the scanning pattern).

As discussed in section 2.3.2, the velocity measured with dual beam OCT is not dependent on the Doppler angle, which is why this method was selected for the measurements presented here. The dual beam approach was also used in the work of Blatter et al. [49], albeit with a different setup, optimized for a different scanning technique: instead of the rotatable BD to split the incoming beam into two and rotate the two beams, which is used in the system presented in this work, the system by Blatter et al. makes use of a a fiber coupler to split the beam into two, and a dove prism to rotate the beams. This has the advantage that both beams can be rotated freely around a common axis (using a BD, the ordinary beam stays fixed while the extraordinary beam rotates around it). The two beams are then scanned by a scanner similar to the one described in section 3.1.3 and focussed onto the retina. However, the scanning pattern differs from the one used here, which will be described in detail in section 5.4.1; in the setup by Blatter et al., the two beams are scanned in a circle around the optic disc (cf. section 5.1.1). In comparison to the scanning technique used by Wang et al. [45], which was described above, both beams are focussed onto the same point of the retina; thus, one circle is scanned simultaneously by two beam with different angles rather then two circles, which are scanned sequentially by only one beam. Additionally, the use of a swept light source makes the measurements very fast, thus reducing motion artefacts. However, focussing the beams onto the sample is problematic, as the circular scanning pattern requires the beams to be focussed at each point of the circle. This makes imaging in vivo more difficult than in the system presented in this work, where the focus could be adjusted for each of the measured scanning lines.

A system using not two but three beams was presented by Trasischker et al. [50]. In this approach, *three* beams are focussed onto the same point of the sample, making the system independent not only of the Doppler angle (as the dual beam system is) but also of the angle β between the plane spanned by the two beams of a dual beam system and a vessel. The method is thus completely independent of any prior knowledge of the sample geometry. The largest disadvantage of the system is the difficulty in focussing. This difficulty was already mentioned in relation to the dual-beam methods; naturally, it is even more pronounced when three beams have to be focussed onto the same point. As the measurement of the angle β is not very time-consuming or difficult, performing in vivo measurements with dual beam systems, such as the one presented in this work, is clearly less complex than with the triple beam system.

Altogether, the approaches to using Doppler OCT to measure total flow values are manifold. Different limitations make the methods suitable or less suitable for different areas of application. As all of the systems mentioned above, the system presented in this work has its downsides – amongst others, it is a dual beam system, with all the technique's limitations (cf. section 2.3.3); nevertheless, as mentioned in the descriptions of the other systems, it also has advantages compared to other approaches and is well suited to the measurement of the total retinal blood flow in the retina for with it was constructed.

Chapter 4

Ex vivo verification of the velocity measurements

*In theory there is no difference
between theory and practice.*

Attributed to Yogi Berra

4.1 Rotating disc, single beam
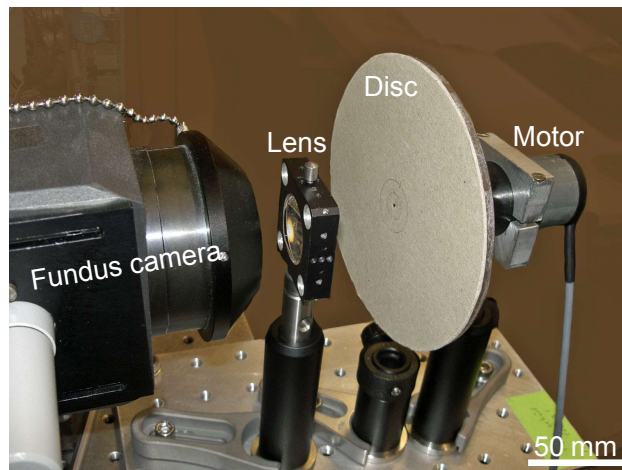
Figure 4.1: Photograph of the test setup to measure a rotating disc.

Naturally, the velocities measured with the OCT setup had to be verified first. One possibility to do so is to measure the known velocity of a rotating disk using only one of the dual beam setup's two beams. To this end, a plastic disc with a cardboard

layer attached to its front is rotated at a given speed using a small motor (maxon DC motor 2130.904-61.112-050). The OCT beam is focussed onto the disc by a lens (as substitution for the eye's optical system in the measurements in vivo). This setup is shown in Fig. 4.1.
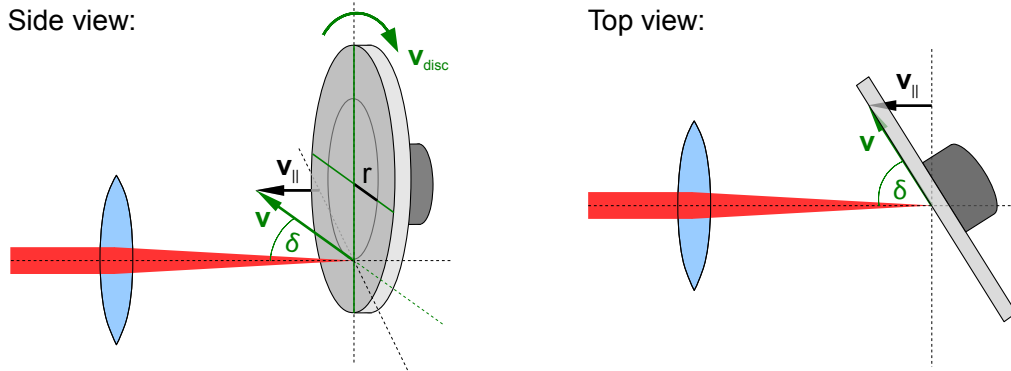
Figure 4.2: Single beam focussed onto a rotating disc.

In the case of a single-beam measurement, the disc must be set at an angle δ to the beam which is *different* from 90°; only then will there be a velocity component in direction of the beam (see Fig. 4.2). The velocities measured with the OCT setup are then compared with the disc's velocity at the point onto which the beam is focussed.

The velocity of the disc at a certain distance r between the centre of the disc and the point onto which the beam is focussed can be calculated as

$$v_{\mathrm{disc}} = \frac{2\pi r}{t_{\mathrm{disc}}}, \tag{4.1}$$

where t_{disc} is the disc's timed period of circulation.

The OCT measurements result in a phase value, which can be converted to a velocity using Eq. 2.72. In this case, the values to be inserted in Eq. 2.72 are the refractive index of the air surrounding the disc, i.e. $n = 1$, the angle $\delta = 82°$ by which the disc is tilted relative to the beam and the SLD's wavelength $\lambda = 838.8\,\mathrm{nm}$. Thus, Eq. 2.72 becomes

$$v_{\mathrm{OCT}} = \Delta\phi \cdot \frac{838.8\,\mathrm{nm}}{4\pi\tau \cdot \cos 82°}. \tag{4.2}$$

The disc was rotated at two different speeds, the beam being focussed on a point $r = 5\,\mathrm{mm}$ away from its centre (i.e. $v_{disc} = 2\pi \cdot 5\,\mathrm{mm}/t_{\mathrm{disc}}$). For each of the two rotation speeds, the phase was measured with the OCT setup using two different line periods (i.e. 27 and 52 µs). The results are given in Table 4.1 and show a very good agreement between the velocity measured with OCT and that calculated from the circulation time for all measurements.

Table 4.1: Velocity of disc (v_{disc}) at a distance of $5\,\mathrm{mm}$ from the disc's centre versus velocity measured with single beam OCT (v_{OCT}) and different exposure times τ at the same point.

Disc		OCT		
t_{disc} [s]	v_{disc} [mm/s]	τ [µs]	$\Delta\phi$ [rad]	v_{OCT} [mm/s]
6.5	4.8	52	0.53	4.9
		27	0.28	5.0
13.7	2.3	52	0.25	2.3
		27	0.12	2.1

4.2 Rotating disc, dual beam

The next step in verifying the data measured with the OCT system was to use both beams, which is the measurement technique used in the measurements on the eye.

Just as in the case of a single beam, the two beams are focussed onto one point of the disc by a lens (see Fig. 4.3). The two beams impinge on the disc under different angles: as opposed to the measurement with one beam, the disc *can* thus be set at an angle of 90° towards the optical axis, as at least one of the beams will always have an angle different to $\delta = 90°$. Nevertheless, the point onto which the beams are focussed onto the disc must still be chosen such that disc's velocity at this point has a component lying in the plane spanned by the two beams. In Fig. 4.3, for example, the beams are vertically aligned; the velocity must thus have a vertical component, or the reflected beams would not be Doppler shifted and the velocity could not be measured. This can be achieved by adjusting the relative position of the beams (horizontal or vertical, depending on the rotation of the beam displacer, cf. section 3.1.2) to the direction of rotation of the point they are focussed on.
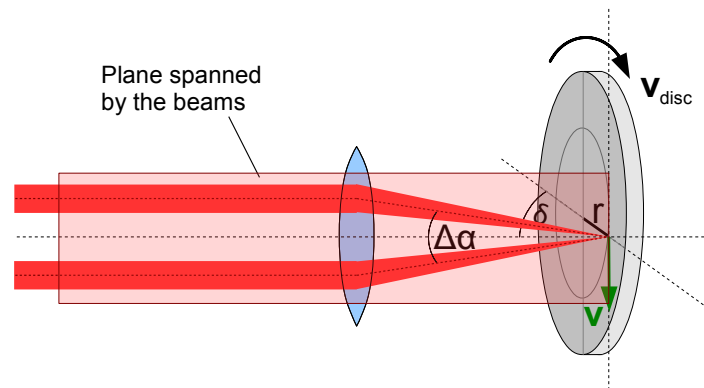
Figure 4.3: Both beams focussed onto a rotating disc.

76

Table 4.2: Velocity of disc (v_{disc}) at a distance of $10\,\text{mm}$ from the disc's centre versus velocity measured with dual beam OCT (v_{OCT}) and different relative beam positions (horizontal, vertical) at the same point.

beam pos.	Disc		OCT		
	t_{disc} [s]	v_{disc} [mm/s]	τ [µs]	$\Delta\phi$ [rad]	v_{OCT} [mm/s]
horizontal	15.4	4.1	52	0.19	3.6
	7.1	8.8		0.43	8.3
	2.3	27.3		1.35	25.7
vertical	15.1	4.2		0.23	4.4
	10.1	6.2		0.35	6.7
	5.0	12.6		0.71	13.6

As before, the disc's velocity is calculated from the period of circulation using Eq. 4.1. The velocity determined using the OCT system is calculated from the measured phase difference using Eq. 2.92. This equation contains the angle β between the plane spanned by the beams and the vector of velocity. If one measures at a point where the vector of velocity lies in the plane of the beams (as in the case depicted in Fig. 4.3), $\beta = 0$. The angle $\Delta\alpha$ between the two beams is, in this experiment, determined by the lenses' focal length and the displacement of the beams: for a lens with $f = 35\,\text{mm}$ and with a beam displacement of $2.34\,\text{mm}$, $\Delta\alpha$ is

$$\Delta\alpha = 2\arctan\left(\frac{2.34/2}{35}\right) = 0.066\,83\,\text{rad}. \tag{4.3}$$

Using this result and inserting the wavelength $\lambda = 838.8\,\text{nm}$, the surrounding air's refractive index $n = 1$ and the angle β, determined above to be zero, Eq. 2.92 becomes

$$v_{\text{OCT}} = \Delta\phi \cdot \frac{838.8\,\text{nm}}{4\pi\tau \cdot 1 \cdot \cos 0° \cdot 0.06683}. \tag{4.4}$$

The disc's velocity was measured with the beams vertically (beam displacer rotated by $0°$), as well as horizontally aligned (beam displacer rotated by $90°$). When changing the relative position of the beams, one had to adapt the point of the disc onto which the beams were focussed accordingly. This ensured that the velocity vector would be in the plane spanned by the beams in both cases. Results for both cases at different disc rotation speeds can be found in Table 4.2; the velocities of the disc and the OCT measurements are, once again, in good agreement.

4.3 Glass capillary

In vitro flow measurements were performed using a glass capillary and diluted milk ($\frac{1}{3}$ milk, $\frac{2}{3}$ water). To move the fluid through the capillary, a syringe was mounted in a syringe driver (a device used to eject a continuous flow of fluid from a syringe). A tube leading to a glass capillary with an inner diameter of $r_{\mathrm{cap}} = 0.157\,\mathrm{mm}$ was attached to the tip of the syringe. Two different syringe drivers were used for the velocity regions of $0\,\mathrm{mm/s}$–$20\,\mathrm{mm/s}$ and $10\,\mathrm{mm/s}$–$35\,\mathrm{mm/s}$. The driver used for the slower velocities (Driv1, combimat, MGVG, München, Germany) displays the volume of liquid ejected per hour. The velocity in the capillary, v_{cap}, can thus be calculated as

$$v_{\mathrm{cap}} = \frac{Q_{\mathrm{Driv1}}}{r_{\mathrm{cap}}^2 \cdot \pi}. \tag{4.5}$$

The syringe driver for the higher velocities (Driv2, Predicor, Infors AG, Basel, Switzerland) displays the driving velocity v_{Driv2}. When using a syringe with an inner diameter $r_{\mathrm{syr}} = 6.3\,\mathrm{mm}$, the velocity in the capillary can be calculated as

$$v_{\mathrm{cap}} = v_{\mathrm{Driv2}} \frac{r_{\mathrm{syr}}^2}{r_{\mathrm{cap}}^2}. \tag{4.6}$$
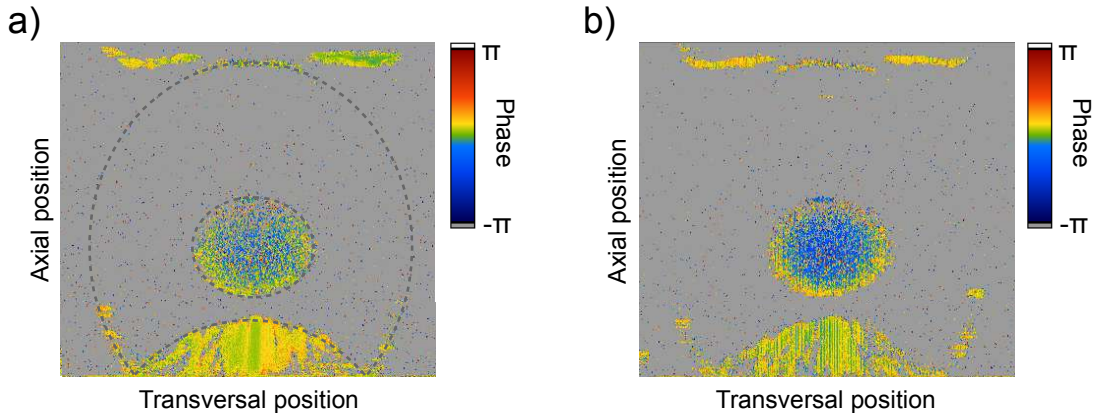
Figure 4.4: Phase images of diluted milk in a glass capillary moving with a) $0.56\,\mathrm{ml/h}$ and b) $0.37\,\mathrm{ml/h}$. The dashed lines in a) denote the inner and outer boarder of the capillary; the outer boarder protrudes past the DC term, so that the mirror terms of its lower end seem 'folded' back into the image.

Recorded phase images are shown in Fig. 4.4. The velocity v_{OCT} obtained the from OCT data was, once again, calculated using Eq. 2.92; inserting the SLD's central wavelength of $\lambda = 838.8\,\mathrm{nm}$, the refractive index of diluted milk (which can be approximated by a linear combination of the refractive indices of milk and water, $n = \frac{1}{3}n_{\mathrm{milk}} + \frac{2}{3}n_{\mathrm{H_2O}} = \frac{1}{3} \cdot 1.345 + \frac{2}{3} \cdot 1.333 = 1.335$), the angle $\Delta\alpha = 0.066\,83\,\mathrm{rad}$ between the beams (cf. Eq. 4.3) and $\cos\beta = 1$, since the capillary was aligned

78
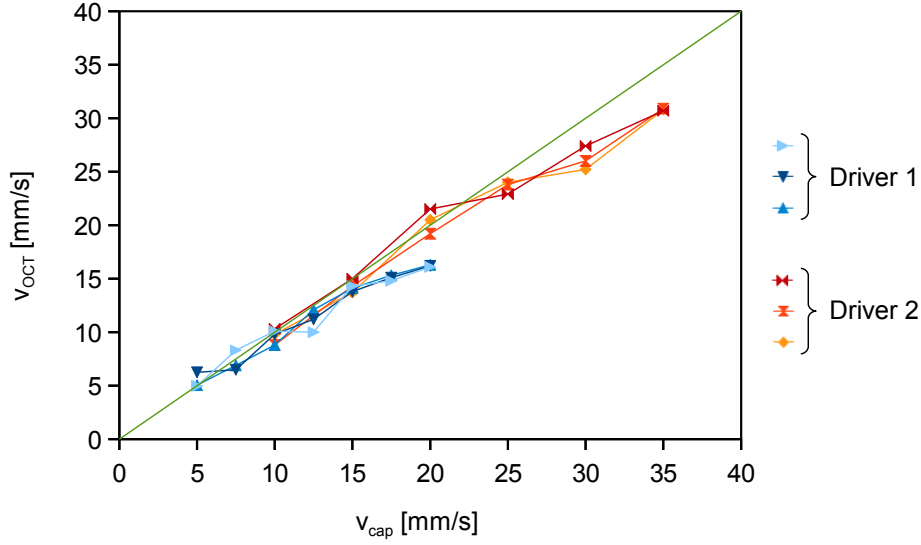
Figure 4.5: Velocity measurements on diluted milk in a glass capillary; blue graphs: slower syringe driver, red and orange graphs: faster driver, green line: unity slope.

parallely to the plane spanned by the beams, one obtains

$$v_{\mathrm{OCT}} = \Delta\phi \cdot \frac{838.8\,\mathrm{nm}}{4\pi \cdot 1.335 \cdot \tau \cdot 1 \cdot 0.06683}. \tag{4.7}$$

The results are displayed in Fig. 4.5; the blue graphs were measured when using the slower syringe driver (Driv1), the red and orange graphs with the faster one (Driv2). The deviations of the measured values from the nominal value in the capillary are most probably due to imprecisions of the syringe drivers when reaching their speed limitations, which would explain why the values around 20 mm/s are correct when using the faster driver, but deviate when using the slower one. In the regions where the syringe drivers are not at their limits, the OCT values are in good agreement with the expected curve.

Overall, the ex vivo measurements confirmed the correctness of the measured OCT data.

Chapter 5

In vivo measurements

5.1 Medical aspects

The eye is the organ of vision, and usually seen as the sense that humans rely on most. A very brief overview of the anatomical and physiological structures of the eye which are of relevance for this work will be given in the following. Much more detailed information on this topic is easily available to the interested reader – apart from the large number of books written on the topic, a search for 'ophthalmology' on the internet gives over nine million hits, which should suffice for any level of interest.

5.1.1 Anatomy of the human eye

The human eye is a complex anatomical system. Fig. 5.1 depicts the components of the eye which are relevant for understanding the *in vivo* measurements and will thus be described in this section.

The outermost layer of the eye is the sclera (the 'white of the eye'), a white protective layer surrounding most of the eye. The inside of the sclera is covered by the choroid, a tissue layer containing the vessels which supply the outer retinal layers
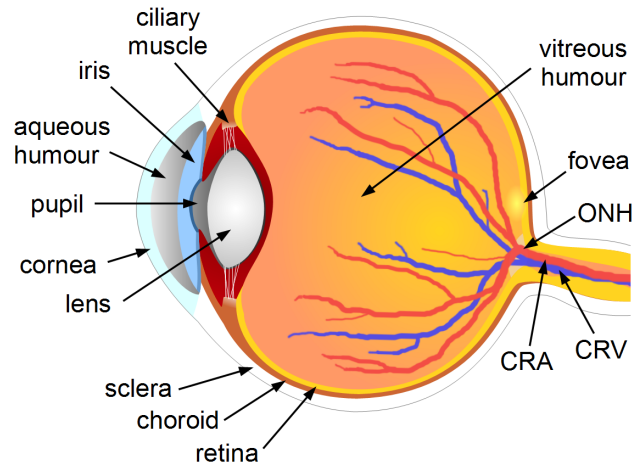
Figure 5.1: Simplified sectional view of the human eye's anatomy with its main layers (sclera, choroid and retina), refractive components (cornea, aqueous humour, lens, and vitreous humour), iris, pupil and ciliary muscles (which are responsible for accommodation and adaptation), the fovea as region of sharpest view and the optic nerve head (ONH) with the central retinal artery (CRA) and central retinal vein (CRV).

and the fovea – the region of sharpest vision – with blood (see section 5.1.2 for more details on the ocular perfusion). The innermost layer of the eye is the retina (see Fig. 5.2). It is itself composed of a number of layers including the nerve fiber layer, several layers of cells and the photoreceptor layer. The latter contains the rods (the very sensitive low-light photoreceptor cells for black-and-white vision) and the cones (photoreceptor cells of three types for colour vision). The vessels supplying the inner retina lie on the inner surface of the retina; these are the vessels in which the blood flow was measured in the course of this work.

Light entering the eye is focussed onto the retina by the eye's refractive parts, namely the cornea and the lens. All of these, as well as the aqueous and vitreous humour filling the eye, are transparent to allow light to pass through them. Together, the eye's refractive components have a refractive power of about $60\,\text{dpt}$[i]. Interestingly, the largest part of the refraction does not, as is often assumed, take place at the lens but at the cornea, as the difference of refractive indices is largest at the barrier between cornea and air. To allow accommodation, i.e. the change of refractivity so as to ensure a sharp image of objects at different distances on the retina, the shape of the lens can be altered by the ciliary muscles. The alteration can induce a change of refractivity of around 10 to $14\,\text{dpt}$ in young humans, but declines with age [52].

The intensity of the light passing into the eye can be regulated by the size of the aperture, called the pupil. The size of the pupil is determined by the pigmented (thus colourful) iris by which it is delimited. The iris is necessary to prevent high light

---

[i]The unit [dpt] stands for diopters – a unit of measurement frequently used in ophthalmology. It equals the reciprocal value of the focal length measured in metres, i.e. $1\,\text{dpt} = 1\,\text{m}^{-1}$.
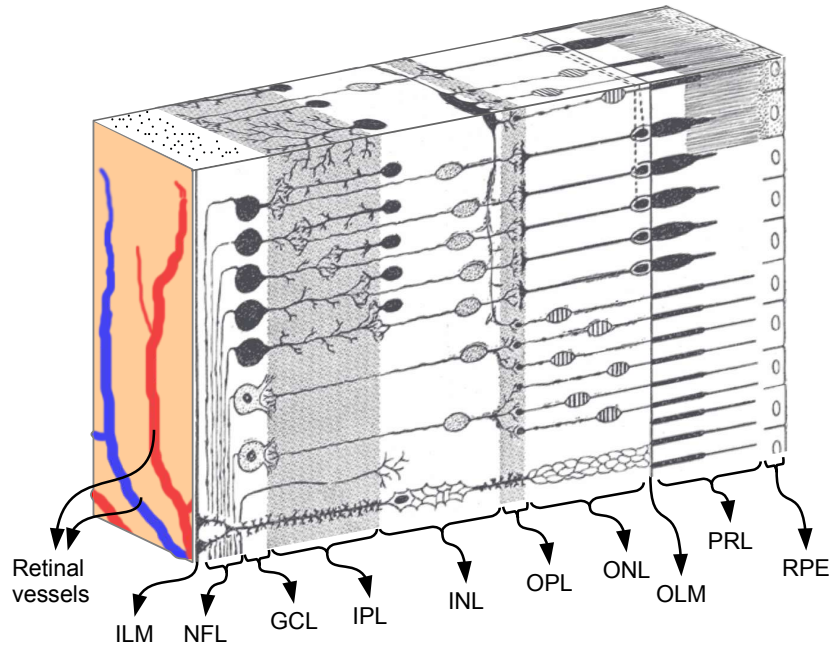
Figure 5.2: Sectional view of the retina with inner limiting membrane (ILM), nerve fiber layer (NFL), ganglion cell layer (GCL), inner plexiform layer (IPL), inner nuclear layer (INL), outer plexiform layer (OPL), outer nuclear layer (ONL), outer limiting membrane (OLM), photoreceptor layer (PRL) with rods and cones, and retinal pigment epithelium layer (RPE). Adapted from [51].

intensities from damaging the cells responsible for vision. For some ophthalmological examinations the pupil must be stopped from restricting. In this case, drugs such as e.g. tropicamin, subsumed under the name 'mydriatics', are administered to dilate the pupil (a state called mydriasis). These substances also induce a temporary paralysis of the ciliary muscles, impeding accommodation. This effect is, in general, desirable for the medical examinations, where a constantly changing accommodation of the eye would only interfere.

5.1.2   Retinal perfusion

Fig. 5.3 shows a fundus image, i.e. an image of the background of the eye. The network of small arteries (lighter, reddish) and veins (darker, bluish) is clearly visible. All of the arteries are branches of the central retinal artery (CRA), which enters the eye at the optic nerve head (ONH) and is responsible for the complete blood supply of the inner retina[ii]. Equally, all of the small veins merge into the central retinal vein (CRV) at the ONH: the CRV is the vessel which is solely responsible for draining the inner retina (see Fig. 5.3, inset). The outer retinal layers, including the photoreceptors, are supplied by the vessels in the choroid.

[ii]With the exception of a small region centred at the fovea, which is supplied by the choroid.
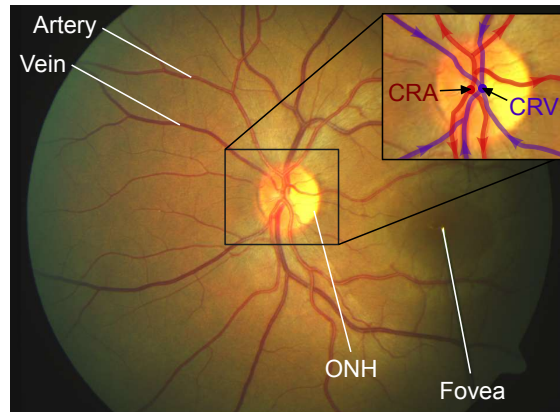
Figure 5.3: Fundus image; the network of arteries and veins splitting up from the CRA and the CRV at the ONH supply all of the inner retina with blood (with exception of a small area around the fovea).

Since the inner retina has no other blood supply than the CRA and the CRV, it would be sufficient to measure the blood flow in one of these two vessels to determine the total retinal blood flow. The CRA and the CRV are, however, not easily accessible, as they are not visible in a fundus image because they vanish into the ONH. This difficulty can be circumnavigated: as all of the vessels lying in the retina either spring from the CRA or drain into the CRV, it suffices to measure the flow in all the arteries or all the veins surrounding the ONH to determine the total retinal blood flow.

The fact that the CRA is the only source of blood supply for the inner retina and the CRV is the only drainage can also be used to validate flowmetry techniques: the blood flow into the eye (via the CRA) must equal the flow out of the eye (through the CRV) or – differently phrased – the total arterial flow must equal the total venous flow. Comparing outcomes of total retinal blood flow measurements in arteries and in veins can therefore serve to verify the validity of the measurement system.[iii]

5.2 Laser safety

Governmental guidelines regulate the use of laser products. The applicable laser safety norm for Austria is the ÖVE/ÖNORM EN 60825-1 [53]. One of the values specified in this guideline is the maximum permissible exposure (MPE), which is an experiment-based value that is set below known hazard limits.

[iii]Clearly, this is only an indicator of a correct measurement and not a final proof, as the measurements of both the arterial and the venous flow could be equally biased.

For exposure times above 10 s, the MPE can be calculated with the formula

$$\text{MPE} = 10 \cdot C_4 \cdot C_7 \text{ W/m}^2; \tag{5.1}$$

C_1 and C_4 are wavelength-dependent coefficients. For a wavelength of 838.8 nm,

$$C_4 = 10^{0.002(\lambda[\text{nm}]-700)},$$
$$C_7 = 1, \tag{5.2}$$

and the MPE becomes

$$\text{MPE} = 10 \cdot 10^{0.002(838.8\,\text{nm}-700)} \text{ W/m}^2 = 18.95 \text{ W/m}^2. \tag{5.3}$$

Regarding the calculation of the maximum permissible power on the human eye, the safety norm [53] notes that "[t]he values of ocular exposure in the wavelength range of 400 nm to 1400 nm are measured over a 7 mm diameter aperture (pupil). The MPE value is not to be adjusted to take into account smaller pupil diameters." The maximum permissible laser power P_{max} can thus be calculated as

$$P_{\text{max}} = \text{MPE} \cdot \frac{d_{\text{pupil}}^2 \cdot \pi}{4} = 18.95 \text{ W/m}^2 \cdot \frac{(7\,\text{mm})^2 \cdot \pi}{4} = 729\,\mu\text{W}. \tag{5.4}$$

To keep well below any dangerous radiation levels, the power on the subject's eye was not allowed to exceed 700 μW. This was verified by measuring the beams' power at the position of the eye with a power meter (Thorlabs, PM100D) at the beginning of each measurement.

5.3   Subjects

A total of four young, healthy subjects aged between 20 and 30 years participated in the study reported in this thesis. The study protocol was approved by the Ethics Committee of the Medical University of Vienna and complied with the standards of the Declaration of Helsinki. All subjects were informed about the nature of the study and gave their written consent to participate.

Inclusion criteria were normal ophthalmic findings and ametropia values of less than 3 dpt. These were determined during the ophthalmic screening examination, which all subjects had to pass prior to the measurements. The examination included slit lamp biomicroscopy and indirect funduscopy.

The subjects' pupils were dilated with one drop of a mydriatic (5 mg/mL, Mydriaticum Agepha eyedrops; AGEPHA GmbH, Austria), a drug used to induce a temporary widening of the pupil and paralysis of the ciliary muscles. The former

was needed to allow the measurement beams and the illumination for the fundus image to enter the pupil; the latter was necessary to prevent the subjects' lenses from accomodating (i.e. changing the refractivity), which would have hampered the adaptation of the measurement system to the eye's optical system. A resting period of fifteen minutes after administration of the mydriatic ensured that the pupil dilation would be sufficient to start the measurements.

As the individual vessels in the subjects' fundi had to be labelled for further reference, a nomenclature based on their position in the fundus as well as a running number was used: vessels inferior to (i.e. below) the ONH were designated with 'I', vessels superior (above) with 'S', nasal vessels (on the side of the nose) with 'N', and temporal vessels (on the side of the temples) with 'T', followed by a number. The fundus images of the measured subjects with vessel denominations are shown in Fig. A.8.

5.4 Measurement technique

5.4.1 Scanning pattern

The goal of this work was to measure the total retinal blood flow, which can be achieved by measuring the flow in all vessels entering or exiting the ONH (see section 5.1.2). It was thus necessary to choose a suitable pattern of scanning positions, completely surrounding the ONH. A rectangular scanning pattern with the ONH at its centre (see Fig. 5.4a) was found to be the most suitable configuration. The scans were performed in a distance of one to two diameters of the ONH; closer to the ONH, the vessels slant away in direction of the occiput[iv]; their angle is then less favourable for the measurement technique described in this thesis. The most evident alternative for the rectangular scanning pattern would have been a circular pattern, as used by a number of groups (e.g. [45, 47, 54]). However, a rectangular pattern consisting of straight lines simplifies the positioning and the adjustment of the measurement beams (which can be corrected separately for each scanning line), as well as the focussing.

As discussed in section 3.1.2, the orientation of the beams in the setup described here was determined with regard to the direction of the measured vessels. This allowed avoiding the problem that no Doppler shift is induced (i.e. the velocity cannot be measured) when the measurement beams are perpendicular to the velocity vector of a vessel. The layout of the vessels in the fundus and the decision to scan rectangularly around the ONH entailed that the vertical scans to both sides of the ONH (blue lines in Fig. 5.4a) mainly crossed vessels with a horizontal orientation,

---

[iv]Anatomical term for the posterior (back) portion of the head or skull.

while the horizontal scans (green lines in Fig. 5.4a) mainly crossed vessels with a vertical orientation. To maximise the Doppler shift in both cases, the orientation of the beams was attuned to that of the vessels: the beams were oriented vertically for the vertical vessels crossed by the horizontal scans (Fig. 5.4b) and vice versa for the horizontal vessels crossed by the vertical scans (Fig. 5.4c).
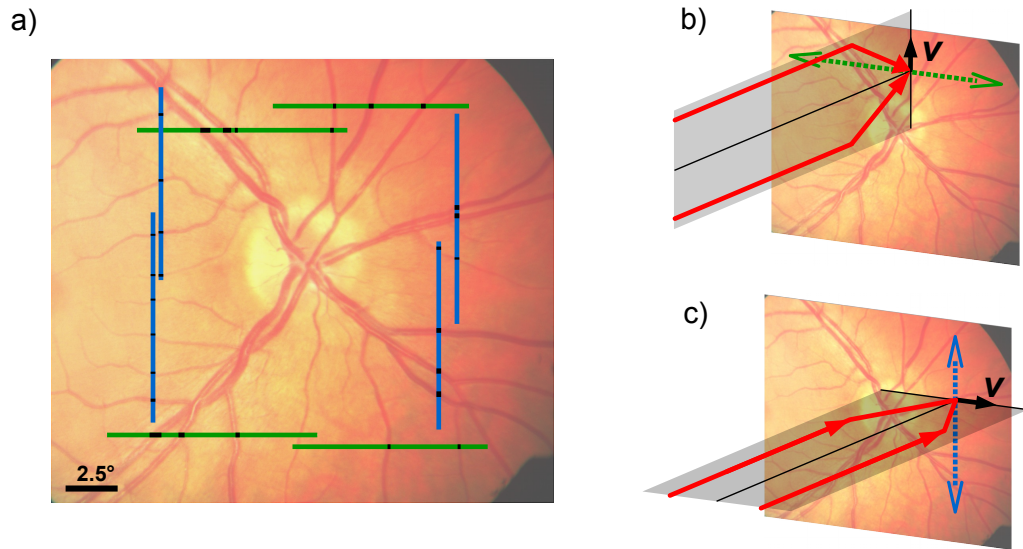
Figure 5.4: Fundus image with the rectangular scanning pattern consisting of eight scans (a); orientation of the beams to measure vessels with mainly vertical (b) and mainly horizontal velocity components (c). The green and blue arrows in (b) and (c) indicate the respective scanning directions. For clarity, the plane spanned by the two beams is depicted as shaded region.

In preparation of the in vivo measurements on individual subjects, adjustments of the scanning pattern to the individual's retina were planned: the general layout of the scans was always the rectangle in a distance of one to two disc-diameters from the ONH; however, the exact position of the scanning lines was adapted for each subject so as to avoid bifurcations and to transect the vessels at positions were they run relatively straight. Selecting straight vessel regions simplifies the determination of the vessel's *en-face* angle β, which is required for the calculation of the blood's flow velocity (Eq. 2.92). The actual scanning positions for all four subjects are shown in Fig. A.8.

5.4.2 Focussing

Focussing the OCT beams onto the same point of the retina is very critical – errors of focus lead to incorrect results, as the calculation of the velocity is based on the assumption that the phase shifts in both beams result from the same point of the vessel.
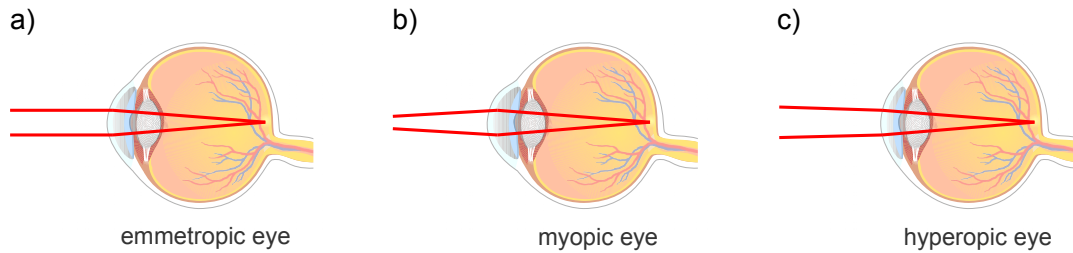
Figure 5.5: To be focussed onto the retina, beams must be parallel before the eye for emmetropic eyes (a), divergent for myopic eyes (b), and convergent for hyperopic eyes (c).

In its default alignment, the optical system is aligned for emmetropic, unaccomodated eyes[v], as the beams enter the eye parallel to each other (cf. section 3.2.5) and are, hence, focussed onto the same point of the fundus. To achieve focussing of the beams onto the retina also for ametropic eyes, the setup has to be adapted: the beams must be divergent to be focussed by myopic eyes and convergent for hyperopic eyes (cf. Fig. 5.5).
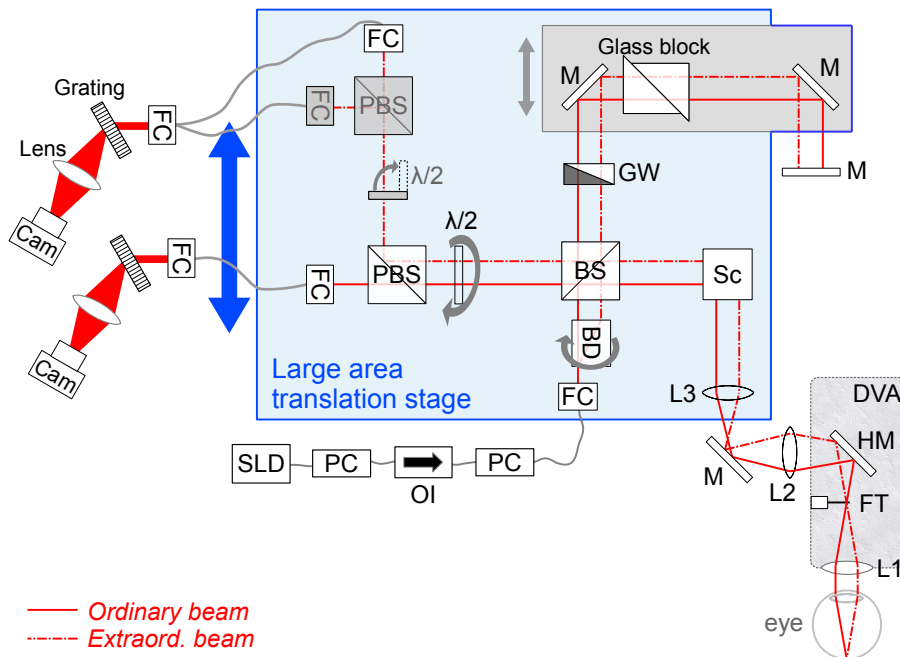
Figure 5.6: Sketch of the OCT system with the large area translation stage (blue) used to make the beams divergent or convergent at the eye to cater for ametropia.

To make the beams divergent or convergent at the cornea, the lens system shown in Fig. 3.18 has to be adapted. However, there are several restrictions: the position

---

[v]The administration of the mydriatic (see section 5.3) not only results in a widening of the pupil, but also a paralysis of the ciliary muscles – accommodation is no longer possible and only objects at infinity are in sharp focus.
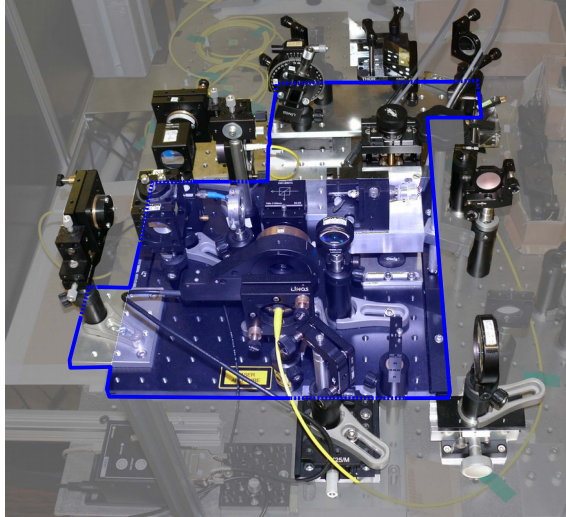
Figure 5.7: Photograph of the large area translation stage (black, tinted blue) and the attached parts that move with it (outlined by the blue line).

of the DVA's ophthalmoscope lens, $L1$, in respect to the eye cannot be changed, as the DVA requires a specific distance to illuminate the fundus optimally and to measure correctly. Also, the distance between the scanner and the lens $L3$ as well as between $L3$ and $L2$ must stay the same, as the scanner has to be in a pupil plane of the system so that the scanned beams will pass the pupil (cf. Fig. 3.16). The only distance that can be changed without interfering with the position of the pupil planes is the distance between $L2$ and $L3$ (as can be seen in Fig. 3.18b, the auxiliary 'pupil beams' are parallel there – changes in the distance between $L3$ and $L2$ will thus only affect the OCT beams, and not the positions of the pupil planes). All other distances must be kept constant. To achieve this, the whole setup up to and including $L3$ was mounted on a large-area translation stage (Thorlabs, TBB3030/M), as shown in Fig. 5.6 and in Fig. 5.7. Moving the part of the setup on the stage thus changed the distance between $L2$ and $L3$ and adapts the reference arm length to the new sample arm length, while leaving all other distances unchanged.

Another reason for incorrect focussing – apart from ametropia – occurs when using large scanning angles: the beams will then be far away from the ideal beam path, i.e. far from the optical axis, passing the lenses peripherally. This leads to aberration-induced errors in the focus overlap of the beams. To avoid this issue, the scanning pattern was chosen to be segmented (i.e. scanning along two short lines instead of one long one on every side of the fundus). Thus, small scanning angles were sufficient, so that aberration errors due to large distances from the optical axis could be avoided. Additionally, the overlap of the beams was visually monitored on the DVA's fundus image.[vi]

[vi]To this end, the infra-red filter of the DVA's CCD camera was exchanged with a weaker one, so as to allow the OCT beams to be seen more clearly in the fundus images.

As a further means of assuring correct focussing, LabVIEW code was programmed by Gerold Aschinger using vessel positions to monitor the correct focussing: if both beams are focussed and scanned over the same area of the retina (e.g. at the position of the green double arrow in Fig. 5.8c), then vessels have to appear in the same position on the images recorded by the two beams. As the blood in the vessels is strongly absorbing, a 'shadow' appears in the tissue behind the vessels (cf. Fig. 5.8a, b). When summing up the values of the amplitude images' pixels in depth direction, areas with vessels will thus have lower values. Graphs of these sums from both beams' images were smoothed using a Savitzky-Golay-filter and then superimposed (Fig. 5.8d). If the troughs (corresponding to the vessel locations) appeared in different positions, then the focus was readjusted.
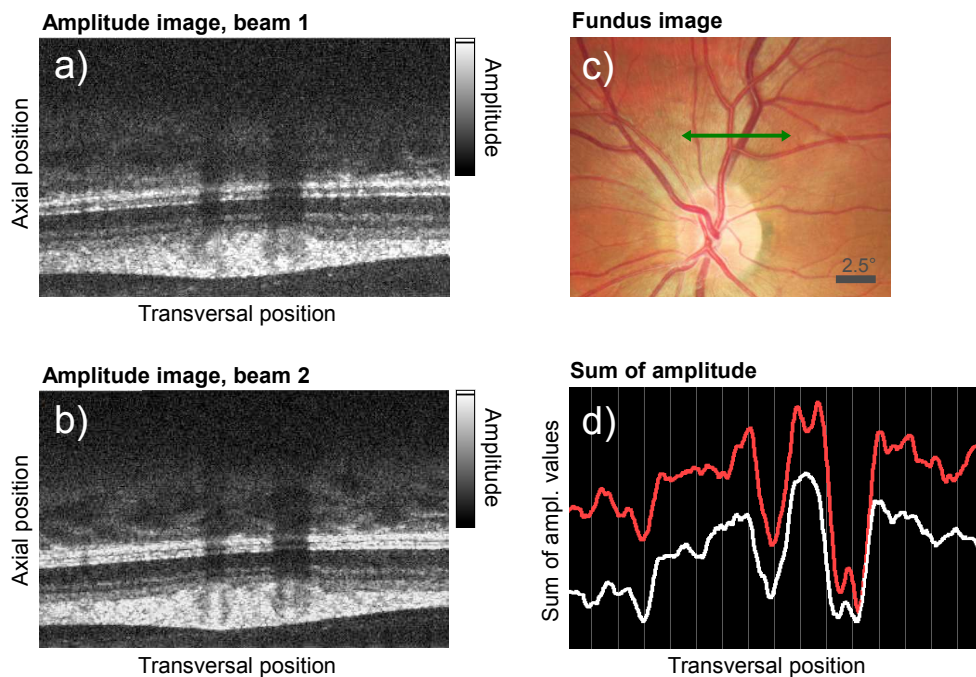
Figure 5.8: Focussing via amplitude summation. (a,b) OCT images with clearly visible 'shadowing' of the tissue behind the vessels for the two beams. (c) Fundus image with measurement position (green double arrow). (d) Superposed sums of amplitude values in depth direction – the shadowed regions behind vessels are clearly visible as troughs.

5.4.3 Measurement preparation

For the in vivo OCT measurements, each subject was asked to sit down and adjust the height of the chair to a position in which forehead and chin could be rested comfortably on the headrest – alignment was found to be more easy and stabler when the subjects were positioned comfortably. Moreover, the subject's head was secured in the headrest with a hook-and-loop fastener – this was also found to result

in stabler measurements and to be more relaxing for the subjects, as less attention had to be paid to holding the head in a stable position.

Via the DVA, a live fundus image of the subject's retina was recorded (see section 3.2.2). The subject was asked to fixate a certain point on the fixation target (a movable LED-light mounted in the DVA's first focal plain, see section 3.2.4). To simplify fixating the target with the measured eye, the subject's other, non-measured eye was covered with an eye-patch. By moving the target and verifying the result on the DVA's live image, the OCT beams were positioned at the scanning positions planned for this individual (cf. section 5.4.1). Great care was taken to focus the beams on the fundus as explained in section 5.4.2.

The image acquisition was performed with the software 'MainDataAcqu.vi', programmed in LabVIEW. The programme is based on code written by René Werkmeister, which was changed and adapted for the work presented in this thesis[vii]. In a first step, the programme starts the line cameras, sets the cameras' shading modes (correcting for the dark signal non-uniformity) and initializes the line cameras' frame grabber boards (Karbon-CL, BitFlow, USA).

For the purpose of alignment and measurement preparation before the actual recording of the OCT data, the cameras were programmatically set to continuous acquisition by a while-loop in the acquisition programme (see Fig. A.7). Straight after their acquisition, the recorded spectra were rescaled. This step is necessary in order to counteract the non-equidistant distribution of the wavelengths on the cameras' CCD-arrays, and is explained in section A.4.1.
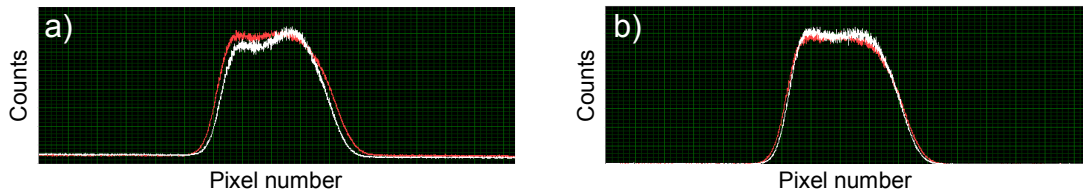
Figure 5.9: Graphs showing the spectra of the two beams (red and white lines). (a) Spectra not well matched. (b) Spectra maximised and better matched by adjusting the beams' polarization.

To maximize the resolution in both channels (i.e. the detection paths for both beams) and make sure that the signal intensity of the beams was comparable, the rescaled spectra were superposed and displayed. As explained in section 3.1.2, the beam from the SLD is split into two beams of equal intensity by the BD if, and only if, the incident beam's polarization is tilted by 45° towards the BDs axis. By changing the polarisation of the incident beam, the two beams' relative intensity can thus be changed. To achieve equal conditions in both arms, the polarization was hence adjusted until both recorded spectra were practically equal (see Fig. 5.9).

[vii]Screenshots and further details of the programme are given in the appendix (see section A.6).

According to Eq. 2.24, the OCT signal depends on the amount of light reflected from the reference arm and the sample arm. To maximize the recorded signal, the beams' power should, consequently, be as high as possible (as far as permitted by the laser safety guidelines, cf. section 5.2). On the other hand, the power should not exceed the maximum value recordable by the CCD-cameras. To verify the latter, the sample arm was covered (the power of the light reflected back from the eye's retina is negligible compared to that reflected by the mirror in the reference arm) and the grey wedge in the reference arm was adjusted until the spectra were as high as possible without overloading the cameras.

Thereafter, the sample arm was uncovered and the complete interference spectrum was recorded by the cameras and rescaled. A previously recorded 'reference spectrum' (i.e. the signal recorded when covering only the sample but not the rest of the sample arm) was subtracted from the complete spectrum, so that only structures from the sample, and not e.g. signals caused by reflections from components in the reference arm, would show up in the displayed images. Subsequently, a fast Fourier transform (FFT) of the spectra was performed, the result of which corresponds to the depth information $i_D(z)$ (see Eq. 2.63). The Fourier transformation of the real-valued detector current gives a complex-valued function, containing both amplitude values and phase values. The amplitude values contain the information on the reflectivity of the different layers in the sample; the phase values contain the velocity information and will be discussed in more detail later on.
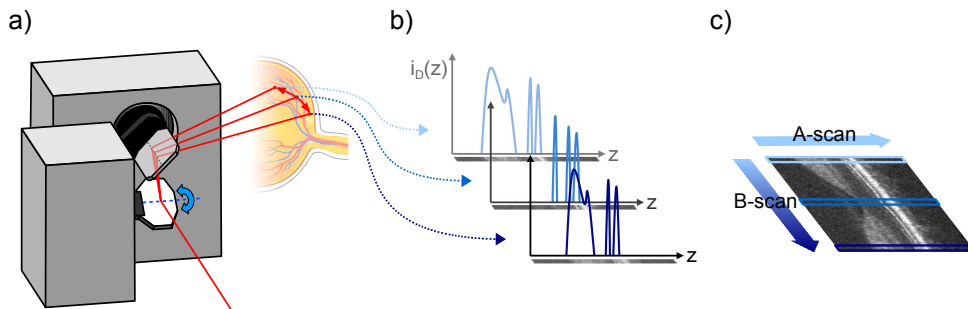
Figure 5.10: Explanation of A- and B-scans. (a) The two focussed OCT beams are scanned across the fundus in a line (for the sake of simplicity, only one of the beams is shown). (b) Depth profiles $i_D(z)$, also called 'A-scans', are recorded along the scanning line. (c) Many adjoining A-scans form a B-scan.

Analogously to ultrasound techniques, the reflectivity profiles are called 'A-scans'. Combining multiple such reflectivity profiles recorded during a scanner sweep of the measurement beams over the retina yields cross-sectional amplitude images, the so-called 'B-scans'. B-scans are thus the two-dimensional, sectional amplitude images achieved by scanning the focussed OCT beams over a line on the fundus and recording a number of one-dimensional depth profiles along the scanning line (see Fig. 5.10). Examples of amplitude images can be seen e.g. in Fig. 5.8a and Fig. 5.8b.

For the measurements reported here, the number of A-scans in one B-scan was set to 3000. As the two line cameras have arrays of 4096 pixels, a B-scan of 4096×3000 pixels was recorded by each camera during every sweep of the scanner. To correlate the cameras' acquisition and the movement of the beams across the retina, the cameras' frame grabber boards were set to be triggered by an external trigger. This external trigger signal was sent by the Reconfigurable I/O (RIO) device (NI PCI-7830R, National Instruments, Texas, USA), which also triggered the scanner's sawtooth-motion (see Fig. 5.11). Each time the scanner had flipped back to its starting position, a trigger signal to acquire a frame was sent to the cameras.
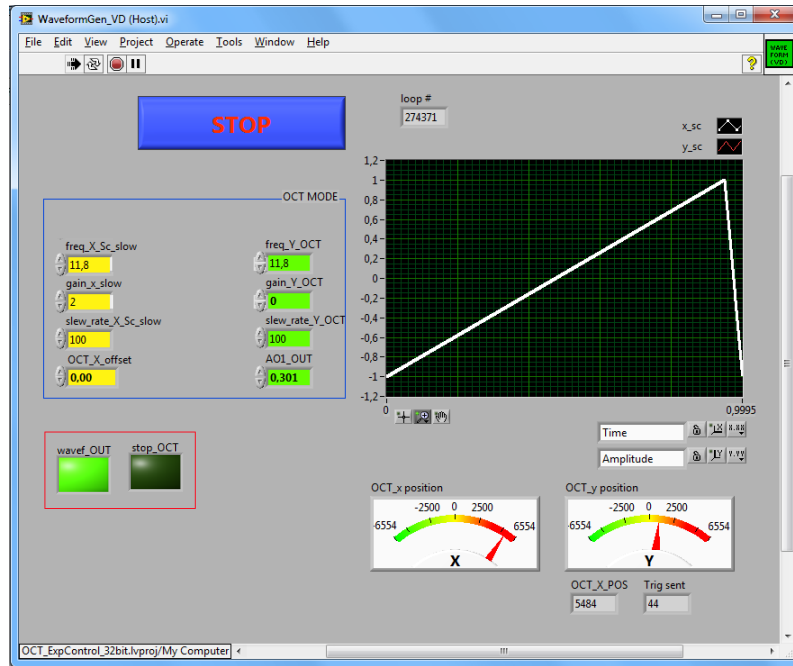
Figure 5.11: Frontpanel of the LabVIEW programme controlling the scanner. The display on the top right shows the scanner's sawtooth motion; the controls on the left change the parameters of the sawtooth (frequency, amplitude, etc.).

To see the signal from the sample, the reference arm's length had to be adapted to the sample arm length; only then was the signal from the subject's retina visible in the amplitude images. Although the signal intensity is highest when sample- and reference-arm length are precisely matched, care was taken to keep the distances between the BS and all the reflecting surfaces in the sample arm either slightly longer or slightly shorter than the distance between the BS and the reference mirror. This was necessary to keep image and mirror image (resulting from the fact that the Fourier transformed signal is symmetric around the DC-peak) well separated (cf. section 2.2.2). Adjusting the reference arm's distance was thus a critical factor in the measurement preparation. A constant alignment could, of course, only be achieved if the subjects did not move the head too much - although readjustments were possible before the measurement, this was not the case during the measure-

ment. Checking the measured images right after each measurement or recording two measurements at every point ensured that measurements corrupted by large head movements could be replaced.

5.4.4 Data acquisition

To determine the flow at one time point, recording one B-scan would be sufficient. To record the time-dependent variation of the blood flow, however, stacks of a number of B-scans had to be recorded at every scanning position. For the measurements presented here, the number of B-scans in each stack was set to 60. With the chosen line period of 27 μs, recording 60 B-scans with 3000 A-scans each resulted in an imaging time of around five seconds – a time frame that is sufficient to record several pulse periods and allow the computation of reasonable mean values, but which is not too strenuous for the subjects. To ensure that movements or errors e.g. in the focus overlap of the beams in one stack of B-scans would not hamper the evaluation of the total flow, the measurements at each of the scanning positions were performed twice.

Before the actual recording of OCT images, the subject was asked to blink once and then, if possible, keep the eye open during the complete recording time (usually around 5 s, as mentioned above).

For the measurements themselves, the required number of buffers was allocated and the frame grabber was set for triggered acquisition into the buffers. Using the DVA's camera, a fundus image was stored automatically right before the beginning of each measurement; the OCT-beams were visible on the image, so that the exact position of the scanning beams on the fundus would be known later on, when the *en-face* angle β of the vessels at the measurement position would be needed for the calculation of the velocity (see Eq. 2.92). The preset number of images was then recorded and stored together with a file with the file extension '.tim' containing information on the image number, the time of recording, the exposure time, etc.

After the last image was recorded and stored, the buffers were deleted, the connection to the boards closed and all changed variables reset to their default values.

5.5 Data evaluation

5.5.1 Automated image processing: amplitude images

All the processing steps that could be done automatically were included into the LabVIEW-programme 'ProcessImages.vi'. In a first step, the images were loaded,

using the information from the '.tim'-file for the number of lines and columns of each image.

Instead of subtracting the same previously recoded reference spectrum (see section 5.4.3) from all the A-scans in all the frames of a stack to eliminate image details that were not caused by the sample, each frame was corrected individually. This method was found to yield more reliable results, and the fact that it is slightly more calculation intensive was irrelevant in the automated post-processing steps (as opposed to the image display during the alignment, where speed is a great issue and subtracting one single reference spectrum from all A-scans gave sufficiently good results). Consequently, instead of subtracting a certain previously recorded reference spectrum, each frame's own 'mean spectrum' was subtracted. In detail, this means that for each frame, all the (in this case 3000) spectra making up the frame were averaged pixel by pixel to give a 'mean spectrum'. Thereby, frequencies which were not background (and thus did not appear on every spectrum) averaged out. However, frequencies that *were* background (and thus the same in each recorded spectrum) and did not average out and could be subtracted from each of the respective frame's recorded spectra.[viii]

In the next step, the data were rescaled (cf. section A.4.1 for details). Furthermore, any residual dispersion effects were numerically compensated: as explained in section 3.1.3, glass blocks were introduced into the reference arm to compensate the dispersion induced by the dispersing media (lenses, eye) in the sample arm. However, this compensation is not perfect (especially since every eye is slightly different) and can be improved by a numerical compensation in the post-processing. The compensated phase $\overline{\phi}(k)$ was computed by adding a phase correction to the original $\phi(k_0)$ using an algorithm developed by Wojtkowski et al. [55]:

$$\overline{\phi}(k) = \phi(k_0) - a_2(k - k_0)^2 - a_3(k - k_0)^3. \tag{5.5}$$

The coefficients a_2 and a_3 were manually varied and the resulting images compared to find the optimal values. Wrong values can seriously distort the image (see Fig. 5.12), so the values were chosen with care.

The corrected data were then Fourier-transformed, which, as already mentioned in section 2.2.2, yields data which are symmetric around zero (i.e. terms and mirror terms). The mirror terms do not carry any additional information; hence, the lower half of the pixels of each Fourier-transformed spectrum was deleted, which made the amount of data to process smaller.

After all these preliminary post-processing steps, the amplitude images (B-scans) could be displayed (see e.g. Fig. 5.12a). As explained in section 5.4.3, the B-scans

---

[viii]If the sample consisted of completely straight structures (such as a mirror face), these would, of course, average out too. However, in vivo samples are never perfectly straight, and were found not to average out.
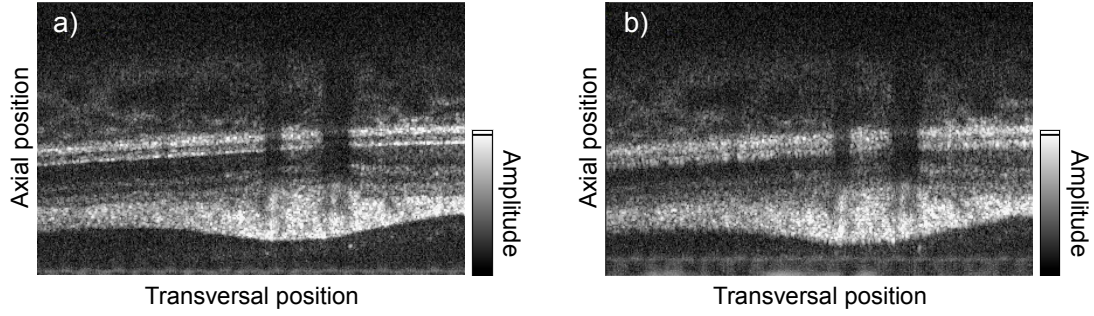
Figure 5.12: Numerical dispersion compensation of a B-scan. (a) Correct values chosen for the coefficients: the several imaged layers are clearly distinguishable. (c) Incorrect values chosen: structures appear blurred.

are composed of the absolute values of the Fourier-transformed spectra recorded during one scanner sweep.

However, the Fourier-transformed spectra contain not only absolute values (i.e. the information contained in the amplitude images) but also phase values. These phase values are necessary to calculate the Doppler shift which, in turn, is needed to obtain the velocity of the blood in the imaged vessels. The details of calculating the phase images will be explained in section 5.5.2.

5.5.2 Automatized image processing: phase images

As explained at the end of section 2.3.1, the Doppler shift $\Delta\phi_D$ results from subtracting the phases of two successive measurements acquired at the same point of the sample. Due to the scanning pattern used for the in vivo measurements, two consecutive measurements were not recorded at exactly the same position, as the scanner moved during the acquisition. However, these changes of position were negligible: assuming e.g. (as was the case in most of the measurements presented in this work) that the scanner scans a line of 1.5 mm with a frequency of 11.8 Hz (i.e. in 0.085 s), then the scanning beam moved a distance s of

$$s = \frac{1.5\,\text{mm}}{0.085\,\text{s}} \cdot 27\,\text{µs} = 0.48\,\text{µm} \tag{5.6}$$

during the line period of 27 µs. Since the size of human RBCs is about 7 µm [56], the distance s was small enough for two consecutive measurements to be considered to have been taken at the same point (cf. also the determination of the oversampling factor in section 3.1.6). The Doppler shift $\Delta\phi_D$ could thus be calculated as the phase shift between two adjacent lines.

The calculation of $\Delta\phi_D$ was executed in a LabVIEW subVI (i.e. a subroutine), a screenshot of which is shown in Fig. 5.13a. As explained in section 5.5.1, the
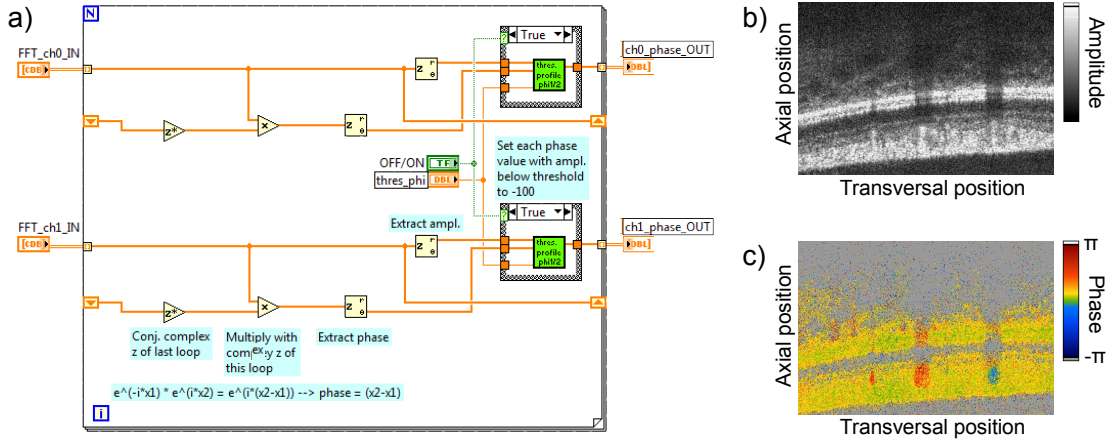
Figure 5.13: Calculating the Doppler shift $\Delta\phi_D$. (a) LabVIEW-subroutine for calculating Doppler shift and setting a threshold based on the corresponding values in the amplitude image (b). (c) Resulting phase image.

Fourier-transformed, complex-valued spectra i_D had, beforehand, been rescaled and dispersion compensated. Line by line, each of these corrected spectra i_D was now multiplied with the complex conjugate of the previous line's spectrum. As $i_D = A \cdot e^{i\phi}$ (cf. Eqs. 2.65 and 2.66), this multiplication yields, for the n-th line,

$$A_{n-1} \cdot e^{-i\phi_{n-1}} \cdot A_n \cdot e^{i\phi_n} = A_{n-1}A_n \cdot e^{i(\phi_n - \phi_{n-1})}. \tag{5.7}$$

Extracting the phase value of the product thus gives the Doppler shift $\Delta\phi_D = \phi_n - \phi_{n-1}$.

The phase image could now be displayed by plotting the resulting lines, or A-scans, of phase values $\Delta\phi_D(z)$ side by side. Before displaying the phase image, however, a thresholding was performed with respect to the values of the amplitude image: pixels that had too low values[ix] in the amplitude image (i.e. which did not represent the highly reflective tissue layers or vessels) were set to -100 (a value that is clearly recognizable to be out of range, as the Fourier transform only yields phase values between $-\pi$ and π) and greyed out in the phase image. The reason therefore was to allow the structure of the tissue, visible in the amplitude images, to become clear in the phase images as well.

Additionally to the thresholding, the phase images were bulk motion corrected using a LabVIEW subroutine programmed by René Werkmeister. The subroutine executes a histogram based correction method first proposed by Makita et al. [57] and adapted by Schmoll et al. [26] and Werkmeister et al. [58]. Amplitude- and phase-values were then stored for further processing.

[ix]The value at which the threshold was set depended upon the quality of the measurement and was determined separately for each stack of images.

For depiction, the phase image was transformed to pseudo-colours. An example of such a thresholded, bulk motion-corrected phase image in pseudo-colours is given in Fig. 5.13c: grey data points signify that the corresponding amplitude value (see Fig. 5.13b) was too low, greenish-yellow data points show that no phase shift occurred, and blue or red values show negative and positive phase shifts, respectively, induced by moving blood cells in the transected vessels.

5.5.3 Vessel area determination

The phase images contain phase values for the complete tomogram (with the exception of pixels set to -100 in the thresholding explained in section 5.5.2). Most of the values represent non-moving tissue; the values there are due to the phase noise, i.e. close to 0. The regions containing tissue, however, are of no further interest; one is only interested in the phase shifts in the regions of vessels, as only these are induced by moving blood cells and contain information of the flow velocity. Hence, the areas containing vessels had to be selected.

To select the areas of the phase image containing a vessel, the LabVIEW programme 'VesselSearch.vi' was used. A screenshot of this programme is shown in Fig. 5.14. First, the programme loads the amplitude and phase images calculated with the automatic processing programme (cf. sections 5.5.1 and 5.5.2). In these images, it is then possible to position cursors around the area containing the vessels (see Fig. 5.14, where the cursors – set to surround the vessel – are depicted in green and red in the phase images).

The vessel areas can be recognized on the one hand by their colour in the phase images: as mentioned in section 5.5.2, the images are shown in pseudo-colours, where positive phase shifts are depicted in red and negative shifts in blue. However, depending on the velocity and the angle of the measuring beam to the vessel, the colour difference of a vessel to the yellow-greenish background can be very slight. Moreover, the velocities at the boarder of the vessel are always very small, which makes the exact boarder of the vessel difficult to distinguish precisely. Hence, one line of 'greenish' pixels with values around zero was included on all sides of the vessel to ensure that all pixels containing a velocity-induced phase shift were contained.

A second possibility to recognize areas containing a vessel is using the shadow the vessel casts on the tissue behind it: as blood is highly absorptive and scattering, not much light reaches the tissue behind the vessel, and the area seems shadowed. This can be seen most markedly in the amplitude image, where the region behind the vessel appears dark. Thus, the positions of the vertical cursors were transferred to the amplitude images (yellow lines in the black-and-white amplitude images in Fig. 5.14) and used as additional reference for the determination of the exact vessel position.
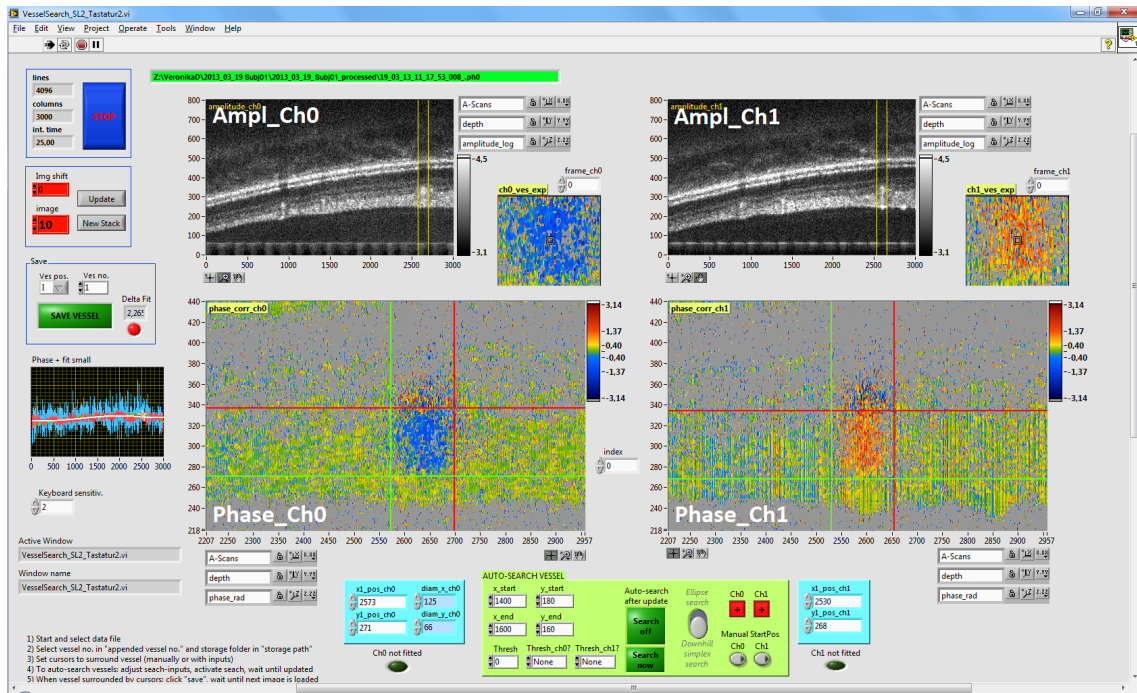
Figure 5.14: Screenshot of 'VesselSearch.vi', the programme used for extracting areas containing vessels. The cursors surrounding the vessel are depicted in green and red in the phase images (Phase_Ch0, Phase_Ch1) of both beams, and the vertical cursors are also displayed as yellow lines in the amplitude images (Ampl_Ch0, Ampl_Ch1) at the top.

On the one hand, the shadows certainly simplify determining the lateral boarders of the vessel. On the other hand, however, the shadowing makes it even more difficult to determine the back side of the vessel, where scattering and absorption obscure the contour. These 'colourful' areas can be seen clearly in the phase images in Fig. 5.14; here, the exact positioning of the horizontal cursors is difficult and requires much practice and experience. Positioning the cursors around the vessels was thus not an easy task and is still the processing step where the largest inter- and intra-grader differences arise, although all graders worked together on a regular basis and followed the same guidelines for determining the vessel boarders.

As the vessel areas had to be determined in every single B-scan (due to movements of the patient's head or eye, the vessels cannot be assumed to be at the same position in consecutive frames), this step is also the most time consuming. For the measurements evaluated in this thesis, the positioning could be done either manually, or by fitting an ellipse into the phase images using a downhill simplex fit routine written by Stefan Löffler. The routine aims to maximise the amount of positive or negative pixels (optionally also only those above or below a certain threshold) inside the ellipse, while minimizing the amount outside. For images with an acceptable image quality and reasonably high phase values, this algorithm worked very well and speeded up the evaluation considerably. At the time of writing this thesis, a further vessel search algorithm has been implemented by Gerold Aschinger which

works in even more cases; however, this algorithm is still in development and was not available when the measurements mentioned in section 5.6 were evaluated.

The region containing a certain vessel (shown in the small insets above the phase images in Fig. 5.14) was thus determined manually or by the fit routine for both measurement channels in each individual B-scan and the stacks of data for both channels were stored. For further processing, only these extracted regions were used.

5.5.4 Unwrapping

As mentioned above (cf. section 5.5.2), the phase values yielded by the Fourier transformation lie in the range of $[-\pi, \pi)$. In some larger vessels (especially in arteries, where the velocities during the systole are high), so-called 'phase wrapping' can occur: if the phase values become so large that they would exceed the range of $[-\pi, \pi)$, they will revert to values at the other end of the range, resulting in a seeming reversal of the flow towards the centre of the vessel. If, for example, an artery's phase values near the region of fastest flow in the vessel centre would exceed $+\pi$, the values above $+\pi$ will 'wrap' and be displayed as negative values (see Fig. 5.15a). This effect can be counteracted by adding or subtracting 2π (depending on whether the values exceeded $+\pi$ or $-\pi$, respectively) to the values over a manually set threshold[x]. The resulting phase values will thus lie in the range of $[-2\pi, 2\pi)$ (cf. Fig. 5.15b). Multiple wrapping could, theoretically, also occur (if the values exceeded even the enlarged range). In practice, however, this was not the case as the exposure times of the cameras were sufficiently small for the range of velocities measured in the vessels.
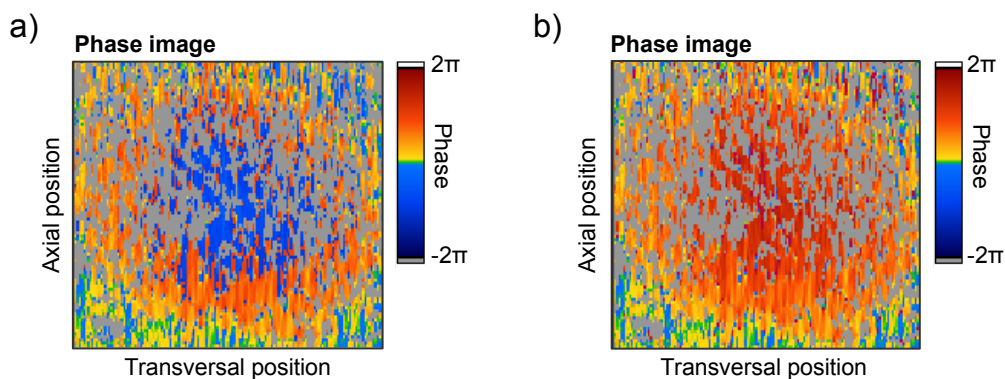
Figure 5.15: Unwrapping the phase data. (a) Wrapped phase: the values are in the range of $[-\pi, \pi)$ and seem to jump from positive to negative nearing the centre of the vessel. (b) Unwrapped, positive values, extending into the range of $[-2\pi, 2\pi)$.

---

[x]The threshold was set low enough to include all wrapped data points, but nevertheless as high as possible, so that no other data points would be falsely 'unwrapped'.

In the course of the data processing, each stack of vessel data was examined for phase wrapping and unwrapped if necessary.

5.5.5 Fitting of the data below the threshold

As mentioned several times (e.g. in section 5.5.2), phase values were set to -100 and greyed out in the phase images if their corresponding amplitude values lay below an empirically determined threshold. This was desirable so as to exclude areas where the phase shift values were not reliable because no (or a too low) signal was detected. It goes without saying that the phase values which were programmatically set to -100 could not be included in the calculation of a meaningful mean phase value in a vessel area which is necessary to determine the mean of the velocity profile – and thus the mean flow – in the vessel (cf. section 5.5.11). Nevertheless, the greyed-out pixels cannot simply be left out of the calculation either, as the phase values in a vessel differ across the vessel's cross-section (low values near the vessel boarders, high values in the centre). Missing pixels would thus distort the mean value, as shown schematically in Fig. 5.16.
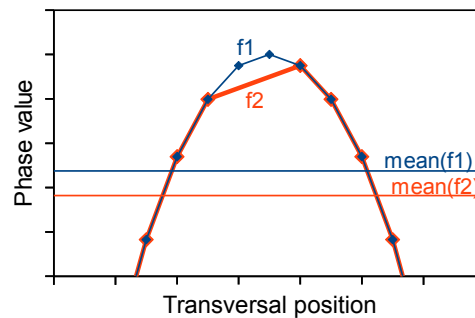
Figure 5.16: Schematic image of the error induced into the calculation of the mean phase value if missing pixels are not fitted: if the actual phase values follow the blue curve (labelled with '$f1$'), the mean is the blue line. If, however, some points are missing (as e.g. in the red curve designated as '$f2$'), the mean will be considerably lower (red line).

Consequently, the -100-values had to be fitted. The missing pixels were fitted to the existing data according to the parabolic function $f(x,y) = a + bx + cy + dx^2 + exy + fy^2$, where a, b, c, d, e and f are the fitted parameters. However, a parabolic flow was not assumed otherwise[xi]. The mean phase value would thus also be close to the true value for non-parabolic flow profiles.

[xi]The flow profiles in vessels are often close to parabolic (a parabolic profile would be expected for a non-Newtonian fluid in a tube), but can also be shaped differently (e.g. exhibiting a flattened flow profile). Although missing values were fitted according to a parabolic profile, none of the other calculations were based on the assumption of a parabolic flow.

Before finally calculating the mean phase shift in a vessel, the data were interpolated via a mean filter (i.e. a convolution with a square of 7×7 pixels) to remove outliers.

5.5.6 Calculating the mean phase shift

For both beams i ($i = 1, 2$), the mean of the phase values inside the vessel area was evaluated simply by adding the phase values $\Delta\phi_{i_n}$ of all the N pixels inside the vessel area and dividing by N:

$$\Delta\phi_{i,\mathrm{mean}} = \frac{1}{N} \sum_{n=1}^{N} \Delta\phi_{i_n}. \tag{5.8}$$

Thus, the mean phase value was determined directly and not via the maximum phase shift[xii].

From the difference of the mean phase shift of the two channels,

$$\Delta\phi_{\mathrm{mean}} = \Delta\phi_{1,\mathrm{mean}} - \Delta\phi_{2,\mathrm{mean}}, \tag{5.9}$$

the blood's velocity in the vessel could then be extracted; the exact procedure and processing steps necessary to achieve this will be explained in the following.

5.5.7 Determination of the angle $\Delta\alpha$

For the calculation of the velocity (see Eq. 2.92), it is necessary to know the angle $\Delta\alpha$ between the two OCT-beams. This angle depends on the experimental setup, which defines the distance between the beams at the cornea, and also on the optical properties and length of the subject's eye.

Initially, the two beams are parallel to each other and, with the scanner set to zero deflection, they have an angle of $\theta_1 = 0°$ to the optical axis. The displacement of the beams, which is due to the properties of the beam displacer (see section 3.1.2), is $2.7\,\mathrm{mm}$, which results in a distance of $r_1 = 1.35\,\mathrm{mm}$ of each beam to the optical axis. The lens system, calibrated for the properties of the ideal Gullstrand eye model [42], alters this distance to $y = 1.17\,\mathrm{mm}$ for each beam (cf. section 3.2.5), but retains the parallelism of the beams upon entering the eye, as an ideal, emmetropic eye will focus parallel beams on the fundus. For the Gullstrand eye model with its

---

[xii]Directly measuring the mean precludes a problem encountered in many papers using e.g. LDV, where the maximally shifted frequency is used; in that case, the measured centre-line velocity has to be converted to a mean velocity using a factor which assumes a specific velocity profile of the blood in a vessel and has lead to much discussion in the scientific community, cf. e.g. [59].

eye length of $d_{\mathrm{eye}} = 24.2\,\mathrm{mm}$, the angle $\Delta\alpha$ between the beams is thus

$$\Delta\alpha = 2\arctan\left(\frac{y}{d_{\mathrm{eye}}}\right) = 2\arctan\left(\frac{1.17}{24.2}\right) = 5.54°. \qquad (5.10)$$

This value is, however, not true for eyes with different eye lengths, and certainly not true for ametropic eyes, as explained in section 5.4.2: for the beams to be focussed onto the retina of ametropic eyes, they have to be non-parallel when they reach the eye – their distance and angle has to be adapted to the eye's optical properties by changing the lens system. This, in turn, changes the angle $\Delta\alpha$ between the focussed beams. As virtually no eye has exactly the ideal properties of the Gullstrand eye model, $\Delta\alpha$ had to be calculated for each individual subject.
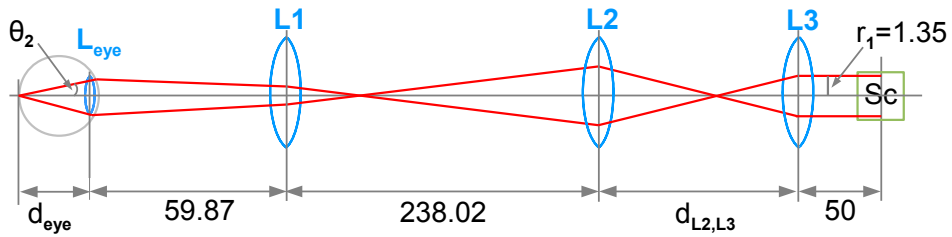
Figure 5.17: Schematic drawing of the beam path adapted for ametropic (here myopic) eyes, used for the calculation of $\Delta\alpha$ for individual subjects. The beams entering the eye are no longer parallel. All lengths are given in mm.

The beam path through the lens system for ametropic eyes is exemplified in Fig. 5.17: as mentioned earlier, each beam initially has a distance of $r_1 = 1.35\,\mathrm{mm}$ from the optical axis and runs in parallel to the optical axis (i.e. $\theta_1 = 0°$). They then pass the lenses $L3$, $L2$, $L1$ and L_{eye}, whereupon they should be focussed onto the retina under an angle of θ_2 to the optical axis (i.e. their distance r_2 from the optical axis at the retina should be zero). As explained in section 5.4.2, the distance between the lenses $L3$ and $L2$ could be adapted to cater for non-ideal optics of the subjects' eyes. Using the matrix method (cf. section A.3), the matrix equation for the lens system (cf. Eq. 3.47 and 3.48) reads

$$\begin{pmatrix} 0 \\ \theta_2 \end{pmatrix} = T_{\mathrm{eye}} \cdot M_{\mathrm{eye}} \cdot T_{L1,L_{\mathrm{eye}}} \cdot M_{L1} \cdot T_{L2,L1} \cdot M_{L2} \cdot T_{L3,L2} \cdot M_{L3} \cdot T_{Sc,L3} \cdot \begin{pmatrix} 1.35 \\ 0 \end{pmatrix} =$$

$$= \begin{pmatrix} 1 & d_{\mathrm{eye}} \\ 0 & 1 \end{pmatrix} \cdot \begin{pmatrix} 1 & 0 \\ -\frac{1}{f_{\mathrm{eye}}} & 1 \end{pmatrix} \cdot \begin{pmatrix} 1 & 59.87 \\ 0 & 1 \end{pmatrix} \cdot \begin{pmatrix} 1 & 0 \\ -\frac{1}{41.76} & 1 \end{pmatrix} \cdot \begin{pmatrix} 1 & 238.02 \\ 0 & 1 \end{pmatrix} \cdot$$

$$\begin{pmatrix} 1 & 0 \\ -\frac{1}{100} & 1 \end{pmatrix} \cdot \begin{pmatrix} 1 & d_{L2,L3} \\ 0 & 1 \end{pmatrix} \cdot \begin{pmatrix} 1 & 0 \\ -\frac{1}{50} & 1 \end{pmatrix} \cdot \begin{pmatrix} 1 & 50 \\ 0 & 1 \end{pmatrix} \cdot \begin{pmatrix} 1.35 \\ 0 \end{pmatrix}, \qquad (5.11)$$

where f_{eye} is the focal length of the eye and all values are given in mm. The top row of the equation can be solved to yield the distance $d_{L2,L3}$ that had to be chosen for

Table 5.1: Values for $d_{L2,L3}$, θ_2 and $\Delta\alpha$ for the Gullstrand eye model and the subjects calculated considering their respective eye lengths and ametropia values.

	Measured		Calculated			
	d_{eye} [mm]	dpt	f_{eye} [mm]	$d_{L2,L3}$ [mm]	θ_2 [mrad]	$\Delta\alpha$ [mrad]
Gullstrand eye model	24.20	0.00	24.20	253.89	48.374	96.748
Subject 1	25.83	-1.00	25.18	252.00	45.345	90.689
Subject 2	24.86	-2.75	23.27	248.71	47.115	94.229
Subject 3	24.87	-1.75	23.83	250.58	47.096	94.192
Subject 4	24.96	0.00	24.96	253.89	46.931	93.862

the beams to be focussed on the retina, whereby the result depends on the length and focal length of the eye:

$$d_{L2,L3} = \frac{253.89 \cdot (d_{\text{eye}} \cdot (f_{\text{eye}} - 7.41) + 7.41 \cdot f_{\text{eye}})}{d_{\text{eye}} \cdot (f_{\text{eye}} + 6.53 \cdot 10^{-3}) - 6.53 \cdot 10^{-3} \cdot f_{\text{eye}}}. \tag{5.12}$$

In emmetropic eyes, beams from infinity are focussed onto the fundus, i.e.

$$f_{\text{eye}} = d_{\text{eye}}. \tag{5.13}$$

For ametropic eyes, eye length and focal length of the eye's lens do not match: with an ametropia-value of n diopters, the relationship between an eye's focal length f_{eye} and the eye length d_{eye} is

$$f_{\text{eye}} = \frac{1}{\frac{1}{d_{\text{eye}}[\text{m}]} - n\,[\text{dpt}]} \cdot 1000\,[\text{mm}]. \tag{5.14}$$

With this knowledge and using Eq. 5.12, the angle θ_2 of the beams to the optical axis can be calculated for each subject's eye length and ametropia values by solving the bottom row of Eq. 5.11 (once again inserting all values in mm):

$$\theta_2 = \frac{1}{f_{\text{eye}}} \cdot \left[-6.22 \cdot 10^{-4} \left(f \cdot (d_{L2,L3} - 253.89) + 6.53 \cdot 10^{-3} \cdot \left(d_{L2,L3} + 2.878 \cdot 10^5 \right) \right) \right]. \tag{5.15}$$

Since θ_2 is half the angle $\Delta\alpha$ separating the two beams (cf. Fig. 5.17), $\Delta\alpha$ can be calculated as

$$\Delta\alpha = 2 \cdot \theta_2. \tag{5.16}$$

Eye lengths and ametropia values as well as the resulting values for $d_{L2,L3}$, θ_2 and $\Delta\alpha$ for the Gullstrand eye model and for the subjects evaluated in this work are given in Table 5.1. Converted to degrees, the values for $\Delta\alpha$ lie between $5.20°$ (subject 1) and $5.54°$ (Gullstrand eye model).

5.5.8   Determination of the angle β

Not only the angle $\Delta\alpha$, but also the angle β enters into the calculation of the velocity (cf. Eq. 2.92). β is the vessel's *en-face* angle, i.e. the angle of the vessel projected onto a plane that is orthogonal to the plane spanned by the beams (in Fig. 2.8, this is the x-y-plane). Thus, β can be determined from fundus images, if the measurement position is known. As explained in section 5.4.4, a fundus image with the OCT-beams visible on the retina (see Fig. 5.18) was recorded using the DVA's camera and stored at the beginning of each measurement. Using a graphics programme, the course of each vessel beneath the scanning beams was marked with a line. As the scanning direction was always perpendicular to the plane spanned by the beams (see Fig. 5.4), the angle β could be determined by reading out the angle between the vessel and the scanning line and subtracting 90°.
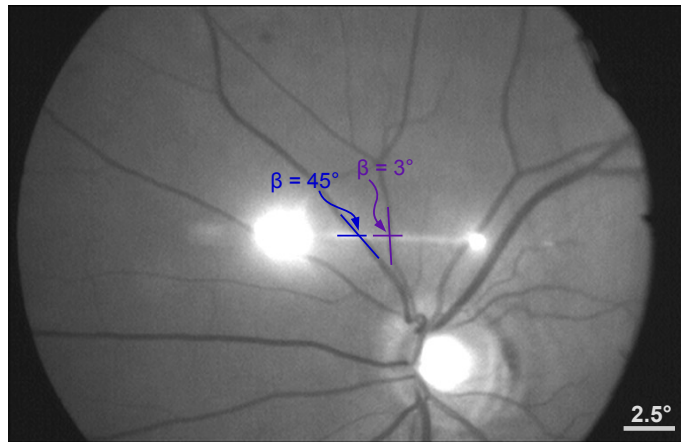
Figure 5.18: Fundus image with horizontally scanned OCT-beams (white line in the centre of the image). The angle β of a vessel at the crossing point of the beams can be determined using a graphics programme as shown for the two vessels in the image centre.

5.5.9   Determining the velocity

Using Eq. 2.92 and inserting the SLD's central wavelength $\lambda_0 = 838.8$ nm, the refractive index $n = 1.37$ of blood, the exposure time τ used for the measurement, the angle $\Delta\alpha$ between the beams calculated for the subject, the *en-face* angle β of the vessel and the mean phase shift $\Delta\phi_{\mathrm{mean}}$ induced by the movement of the blood in the vessel, the mean velocity of the blood flow can be calculated.

The mean phase shift $\Delta\phi_{\mathrm{mean}}$ used in the calculation must be a mean over space and over time: on the one hand, the phase shift is not constant over the vessel cross-section; thus, all pixels in the vessel area were averaged (see section 5.5.6). On the other hand, the phase shift varies due to the pulsatility of the blood flow (see section 5.6.1); consequently, the phase shift was averaged over several pulse cycles.

Table 5.2: Flow velocities v_{mean} of the inferior vessels of subject 1 and the data used to calculate these values (i.e. phase shift $\Delta\phi_{\mathrm{mean}}$ and *en-face* angle β of the vessel in question, as well as the exposure time τ used in the respective measurement).

Vessel #	Type	τ [μs]	β [deg]	$\Delta\phi_{\mathrm{mean}}$ [rad]	v_{mean} [mm/s]
I1	A	25	44	0.80653	3.6
I2	V	25	12.5	0.66072	13.5
I3	A	25	4	0.70300	7.9
I4	V	25	54	0.23650	14.9

As an example, Table 5.2 gives the velocities in several arteries ('A') and veins ('V') of subject 1 (for a fundus image, see Fig. A.8). $\Delta\alpha$ for subject 1, which is needed for the velocity determination, was calculated to be 90.689 mrad (see section 5.5.7).

5.5.10   DVA measurements

Additionally to the OCT measurements, the measured fundus region was recorded using the DVA (see section 3.2.2). This allowed postponing the evaluation of the recorded vessels' diameters to after the measurement session, thus speeding up the procedure. During the DVA recordings, the subjects did not have to hold their eye open – the DVA's software can deal with gaps in the recording due to blinking. Moreover, the DVA has an eye-tracking algorithm, so that stable fixation was less critical than during the OCT measurements.

The DVA's fundus camera and its software are calibrated for the Gullstrand eye model [42]. Only for such a configuration do the DVA's values correspond to absolute values in micrometer [41]. For eyes with eye lengths or ametropia values different from those of the Gullstrand eye model, a corrective multiplication factor F_{corr} has to be included. This factor was determined individually via a measurement of each subject's axial eye length and axial refraction values and was used to convert the DVA's results into micrometer. For the four subjects measured, the corrective factors are given in Table 5.3.

The DVA gives precise results for vessel diameters in its measurement range of vessel diameters down to 65 µm [41]; below this value, however, the results are less accurate. Consequently, vessels with diameters < 65 µm were measured using a different approach: at the position of each of the small vessels, an OCT measurement with a large number of lines (i.e. a high oversampling factor) and a long exposure

Table 5.3: Corrective factors F_{corr} for each subject necessary to convert the results of the vessel diameters given by the DVA to µm.

	F_{corr}
Gullstrand eye model	1.000
Subject 1	1.007
Subject 2	0.872
Subject 3	0.927
Subject 4	1.025

time (80 µs) was recorded[xiii]. The long exposure time allowed a high phase value to accumulate despite the low velocity of the blood in these small vessels. As discussed in section 3.1.6, the axial resolution of OCT is only determined by the bandwidth of the OCT's source, the refractive index of the medium, and the recording spectrometers' properties. Consequently, the axial pixel size of all images recorded with the same OCT system is identical. Thus, the size of vessels with diameters < 65 µm was determined as number of pixels in the OCT images. Principally, the pixel counts for the small vessels could be correlated directly with absolute units using the formula for the image resolution derived in section 3.1.6.

However, using the OCT pixels for the diameter determination is somewhat problematic, as was already discussed in section 3.2.1: velocities at the vessel walls may lie below the OCT's noise level, cell-free areas at the vessel walls do not yield a Doppler signal, shadowing effects behind the vessels obscure the borders, etc. All of these effects can lead to an underestimation of the vessel size with OCT. Diameter determination with the DVA is less problematic: it uses contrast rather than velocity values to determine the vessel boarders, its algorithms were developed exclusively for the purpose of determining diameters and it measures the *en-face* diameter, thereby avoiding problems with the shadowing behind the vessels. The only problem is that it only measures accurately for diameters > 65 µm.

The solution to measuring small diameters was thus to combine OCT and DVA: in order to correlate the measured OCT pixel values with absolute units, a number of large vessels' sizes in pixels was measured in addition to the small vessels and compared to the results of the DVA-measurement on the same large vessels. The resulting factor between the axial OCT-pixel size and the results from the DVA was then used as conversion factor to absolute units. This method allowed the determination of vessel diameters of down to about 30 µm.

[xiii]So as not to overstrain the focussing capabilities of the subjects and to keep the measurement time reasonable, the number of B-scans in these stacks was limited to 30.

5.5.11 Calculation of the flow

With the knowledge of a vessel's mean velocity v_{mean} determined from the OCT measurements via the steps detailed in section 5.5.9 and the corresponding vessel diameter D determined as described in section 5.5.10, it was possible to calculate the blood flow Q through each vessel using the equation for the flow:

$$Q = \frac{v_{\text{mean}} \cdot D^2 \cdot \pi}{4}. \qquad (5.17)$$

By calculating the flow values of all veins and all arteries entering and exiting the ONH, the total retinal blood flow in veins and arteries could be determined.

5.6 Results and discussion

As mentioned earlier (see section 5.3), total retinal blood flow measurements were performed on four young healthy subjects. Tables containing the data measured and calculated for the four subjects are given in section A.8. The different aspects of the results of the flow measurements will be explained in detail in the following.

5.6.1 Time dependence of the flow

Due to the heart beat, the flow in the retinal arteries is pulsatile (moreover, some of the retinal veins may also exhibit a low pulsatility). As mentioned in section 5.4.4, it was possible to monitor the pulsatility with the measurement technique explained in this thesis: the line period of $27\,\mu s$ in combination with a stack size of 60 B-scans with 3000 A-scans each results in an imaging time of around five seconds for each stack; this amount of time is sufficiently long to record several pulse periods.

Fig. 5.19 shows the change of the phase shifts in the two channels as well as the phase shift difference between the two channels for an artery (Fig. 5.19a) and a vein (Fig. 5.19b). Clearly, the artery's phase shift values are highly pulsatile, while the vein exhibits a constant phase shift difference (i.e. a constant velocity) over time. The ability to resolve these differences and to show the time course so distinctly underlines the high accuracy of the system, also in terms of temporal resolution.

The pulsatility of the phase values naturally corresponds to a pulsatility of the velocity and thus of the flow. To determine the time-independent mean value of the total retinal blood flow, the average of the phase shift over the several pulse periods was used in the calculations of velocity and flow (cf. section 5.5.9).
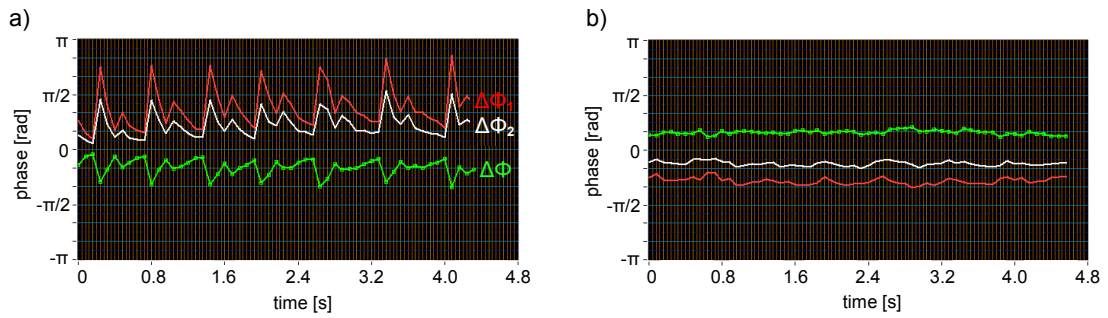
Figure 5.19: Phase shift changes over time for both individual beams (red and white graphs) and for the resulting phase shift difference (green graph). (a) Timeline of the phase shift in an artery. (b) Timeline of the phase shift in a vein.

Fig. 5.19b also clearly illustrates one of the major advantages of a dual beam system: the timelines of the phase shift in the two individual beams (red and white graphs) are not constant; the irregularities are due to small movements of the subject's head or eye, which are practically impossible to suppress even for very motivated subjects. One of these graphs would be the result gained from a single-beam system. The difference between the two phase shifts (green graph in Fig. 5.19b), however, is much straighter. This is due to the fact that phase shifts induced by movements of the subjects rather than movements of the RBCs occur simultaneously in both channels and cancel out when computing the phase shift difference. The results gained from a dual-beam system are thus considerable more stable and reliable than those from single-beam systems.

5.6.2   Temporal versus nasal flow
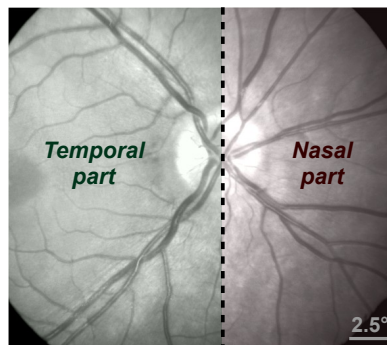
Figure 5.20: Division of the retina into a temporal and a nasal part by an imaginary line through the ONH. The temporal part is larger and contains the macula (darker area on the left side of the image).

A number of earlier studies (e.g. [38, 39, 60–62]) investigated the differences between temporal and nasal blood flow. To this end, an imaginary line is drawn through the

ONH (see Fig. 5.20); the flow in vessels to the temporal and to the nasal side of this line are then evaluated separately and compared.

In accordance with the published results, the blood flow in the temporal part of the retina was found to be considerable larger than in the nasal part (see Table 5.4). Riva et al. [38] attribute this to the larger area of the temporal retina: as the ONH lies a few millimetres to the nasal side of the fovea, the temporal area is larger than the nasal one. Additionally, Rassam et al. [60] remark that the temporal area contains the metabolically active part of the retina, namely the macula.

Table 5.4: Nasal vs. temporal flows in veins (V) and arteries (A) of the four measured subjects.

	A		V	
	nasal	temporal	nasal	temporal
Subject 1	15.3	23.3	9.3	26.0
Subject 2	9.7	19.9	10.0	22.5
Subject 3	11.4	25.8	15.4	18.2
Subject 4	13.7	23.5	9.5	32.9

5.6.3   Total flow

The results for the flow in the individual vessels of all subjects are listed in Tables A.1 to A.4. Summing up the total arterial or venous flow results in the total retinal blood flow. The latter is the property I set out to determine at the beginning of my thesis, as it is this value that changes in a number of ocular diseases (cf. chapter 1).

The mean arterial flow of all four subjects measured for this thesis was found to be $(35.7 \pm 4.1)\,\mu l/min$[xiv]; the mean venous flow was quantified as $(36.0 \pm 4.5)\,\mu l/min$ (cf. Table 5.5). Similar values have been reported by a number of studies using different measurement methods.

Using bidirectional LDV, Riva et al. [38] measured the retinal blood flow in arteries down to $39\,\mu m$ and veins down to $60\,\mu m$ as early as 1985. As mentioned in section 5.5.6, LDV does not measure the mean velocity directly; rather, the maximum velocity in the vessels' centre is measured, which has to be divided by a scaling factor to yield the mean velocity. Assuming this factor to be 1.6 and extrapolating the values for the vessels which were below their measurement range, Riva et al. reported total retinal blood flow values of $(33.0 \pm 9.6)\,\mu l/min$ in the arteries and $(34.0 \pm 6.3)\,\mu l/min$ in the veins of twelve healthy subjects (ibid.).

[xiv]Data are means $\pm$ standard deviations.

Another study that was among the first to report data on the total retinal blood flow was carried out by Feke et al. [39], who also used LDV to measure the flow velocities. However, they assumed the scaling factor between maximum and mean velocity to be $v_{\mathrm{max}}/v_{\mathrm{mean}} = 2$ (which is the case if the flow profile is parabolic) rather than 1.6, arriving at a higher value of $(80 \pm 12)\,\mathrm{\mu l/min}$ for the retinal blood flow in the three to five largest veins and, in two cases, also the largest retinal arteries of six healthy subjects. As this was one of the first measurements of the total retinal blood flow, there were not too many comparative measurements at the time. Retrospectively, however, the values seem to be rather higher than those reported in other publications.

Also using LDV, but once again with a scaling factor of 1.6, Grunwald and co-workers estimated the retinal blood flow in the larger retinal veins (in most cases only the four or five largest ones) and arrived at a value of $(38.1 \pm 6.2)\,\mathrm{\mu l/min}$ [1] from their measurements of the four to five largest retinal veins of twelve normal subjects, as well as $(38.5 \pm 4.7)\,\mathrm{\mu l/min}$ [40] from the measured three to six largest retinal veins of 16 subjects.

While all previously reported measurements used monochromatic fundus photographs to determine the vessel diameters, Garcia et al. [61] measured the total retinal blood flow with a Canon Laser Blood Flowmeter (a commercially available system based on LDV that is capable of measuring both the blood velocity and the diameter). They judged only the results of five of the 14 subjects they had measured to be reliable; among these five subjects, they found a blood flow value of $(64.9 \pm 12.8)\,\mathrm{\mu l/min}$ for the 4-6 largest retinal veins.

A number of studies using LDV as well, but measuring the vessel diameter with a DVA (as was done in this study) were previously carried out by our group: Polska et al. [63] reported a retinal blood flow value of $(34.1 \pm 2.3)\,\mathrm{\mu l/min}$ for eleven subjects, whereby the mean velocity was assumed to be $v_{\mathrm{max}}/1.6$. Pemp et al. [2] stated a retinal blood flow value of $(43 \pm 12)\,\mathrm{\mu l/min}$ in a study of 20 healthy subjects, using a factor of 2 between maximum and mean velocity. Using the same factor, Garhöfer et al. [62] measured the total retinal blood flow in all vessels with diameters above $60\,\mathrm{\mu m}$ and extrapolated the value for smaller vessels, yielding retinal blood flow values of $(42.3 \pm 12.1)\,\mathrm{\mu l/min}$ in the veins and $(43.3 \pm 12.1)\,\mathrm{\mu l/min}$ in the arteries of 64 healthy volunteers.

There have, of course, also been earlier attempts to measure the total retinal blood flow using FDOCT, as was done in the thesis on hand: the pioneering work in using FDOCT, albeit with a single beam, for the determination of the total retinal blood flow was performed by Wang et al. [45]. They overcame the difficulty of single beam OCT being dependent of the Doppler angle by scanning the beam in two concentric circles and calculating the vessel geometry from these data (cf. section 3.4). Drawbacks of this method are the high movement sensitivity (for the method to work, the circles have to be precisely concentric) and the inability to measure vessels with

confluences or curves between the two scanning circles. Nevertheless, they were able to determine the total retinal blood flow in the veins with diameters above 65 µm of two subjects to be (52.90 ± 2.75) µl/min and (45.20 ± 3.18) µl/min. In their follow-up studies, the group extended the number of patients measured: including veins with diameters down to 33 µm, they reported a mean total retinal blood flow of (45.6 ± 3.8) µl/min for eight subjects [46], and of (47.6 ± 5.4) µl/min for veins to below 30 µm for twenty healthy subjects [47]. In all of these studies, the vessel diameters were determined from the OCT images. The drawback of using the OCT images, however, is that the diameters might be underestimated due to the slow velocities at the vessel borders (cf. section 5.5.10). This drawback was avoided in the study presented here by using the DVA for the vessel diameter determination.

Deviations between the results of the total retinal blood flow presented in this thesis and earlier measurements may be explained by the small number of subjects in this study (the total blood flow can vary distinctly between different subjects; cf. Table 5.5). Studies including a larger number of subjects are already under way. Nevertheless, the results reported in this thesis are in good agreement with earlier results.

Several other aspects merit mentioning at this point to underline the advantages of the setup described in this thesis; these will be discussed in the following.

Small vessels

One of the advantages of the method employed in the work reported here was that it allowed the determination of vessel diameters of down to about 30 µm (see section 5.5.10) and, consequently, also flow values in these small vessels. These low flow values had, for the most part, been disregarded (e.g. in [1, 39, 40]) or only been estimated in the studies of ocular blood flow to date (e.g. in [38, 62]). With the system proposed here, it was possible to *measure* these small flows. That the flow in these small vessels should not be disregarded can be seen from the data measured in the course of this work and given in Tables A.1 to A.4: on average, the flow in vessels with diameters between 65 µm and 30 µm constituted above 6 % of the total flow.

In a study by Riva et al. [38], in which arteries down to 39 µm were included, the flow in arteries of 60 µm was measured to be 1 µl/min; this value could be confirmed in the measurements conducted with the setup described here.

Regarding veins, however, the study by Riva et al. (ibid.) only reported values for vessel diameters above 60 µm, and just gave an estimate for values below this limit. In the course of this thesis, the flow in veins of down to around 30 µm could be measured as well: a value of 1 µl/min was determined to be a good estimate for veins of 60 µm as well as for arteries, as had been suggested by Garhöfer et al. [62].

Table 5.5: Number of large ($D > 65\,\mu m$) and small ($D < 65\,\mu m$) vessels ('A' for arteries, 'V' for veins) measured for each subject, as well as the calculated venous and arterial flow.

	Subject 1	Subject 2	Subject 3	Subject 4	mean $\pm$ SD
# V $> 65\,\mu m$	8	7	6	5	
# V $< 65\,\mu m$	2	5	3	2	
# A $> 65\,\mu m$	6	7	5	5	
# A $< 65\,\mu m$	2	3	5	2	
Q_V [µl/min]	38.6	29.7	37.2	37.3	35.7 ± 4.1
Q_A [µl/min]	35.4	32.5	33.6	42.4	36.0 ± 4.5

The flow in small vessels ($D < 65\,\mu m$) was found to exhibit interesting characteristics, which will be described in section 5.6.4.

Comparison of arterial and venous flow

With the system described in this thesis, it was possible to measure the velocity of RBCs in veins as well as in arteries. This is not to be taken for granted: many studies reporting total retinal blood flow data used only the venous or only the arterial values, claiming that the respective other value had to be the same. Wang et al. [45], for example, states that

> [b]ecause the total venous flow volume is identical to that of arteries in the retina, as shown by Riva and colleagues [...], measuring the total venous flow alone is sufficient to quantify the total retinal blood flow.

This is, of course, correct (as was established in section 5.1.2), as the the inner retina is supplied solely by the CRA and is drained solely by the CRV. Thus, adhering to the law of mass conservation, all the blood entering the inner retina must exit it again. As venous and arterial flow have different properties (e.g. different pulsatility, velocity, etc.), some methods are simply more suited to measure one or the other.

Nevertheless, it is a great advantage to be able to measure both the venous and the arterial flow: if the two measurements give similar values, this is a good indicator for the system's functionality. This test of concept is not available in studies measuring only one type of flow. Table 5.5 shows the values for the venous and the arterial flow of the four measured subjects. As can be seen, the venous and arterial flows are in very good agreement.

5.6.4 Murray's law

As mentioned before, it was possible to measure vessels with a large range of diameters in this study. An interesting characteristic was found when investigating the correlation between vessel diameter and blood flow in the vessel over this large range of diameters. Before going into detail regarding the findings, however, it is necessary to look at the theory of blood flow in a vessel.

An incompressible, Newtonian[xv] fluid flowing laminarly through a pipe with a constant, circular cross-section with radius R behaves according to the Hagen-Poiseuille-law, which states that

$$Q = \frac{\pi R^4}{8\eta} \frac{\partial p}{\partial x},$$
(5.18)

where η is the fluid's viscosity and $\partial p/\partial x$ is the pressure gradient along the length of the pipe. For blood, being a non-Newtonian fluid, the equation is be a bit more complex, the dependence of the flow Q on the fourth power of the radius, however, remains the same (cf. e.g. [64]).

In 1926, Murray published a paper in which he applied the principle of minimum work to the vascular system [65]. He suggested that small vessels would require much energy to pump the blood through the body due to the high friction on their walls. However, if the vessels were too large, they would require a large large volume of blood to fill them. Since blood must be produced and maintained by the body, requiring large amounts of blood would also require a lot of energy. Starting with Hagen-Poiseuille's law and including this energy-minimisation consideration, Murray arrived at a modified equation for the blood flow in the vascular system:

$$Q \propto \frac{R^3}{\sqrt{\eta}}.$$
(5.19)

When plotted on a log-log scale, the flow should thus rise linearly with the radius with a factor of three. A number of earlier studies attempted to measure this factor experimentally, and reported values close to three: Riva et al. [38], measuring arteries with $39\,\mu m$ to $134\,\mu m$ and veins with $64\,\mu m$ to $177\,\mu m$, arrived at values of 2.76 ± 0.16 and 2.84 ± 0.12, respectively. Grunwald et al. [1] reported, for 54 veins with diameters of $72\,\mu m$ to $185\,\mu m$, a value of 2.87. A slightly higher value of 3.35 ± 0.23 was reported by Garcia et al. [61] when studying 22 retinal veins of $84\,\mu m$ to $177\,\mu m$ diameter.

The log-log regression analysis for diameter and blood flow was also performed in the course of this thesis. Using the data from the vessels with diameters above $65\,\mu m$

[xv]A Newtonian fluid is inelastic, i.e. the viscous stresses in the fluid are linearly proportional to the strain rate.

yielded values similar to those reported in literature: the regression coefficient was found to be 2.83 ± 0.13 in veins and 3.71 ± 0.27 in arteries[xvi].

An unexpected trend was found, however, when including vessels with diameters below 65 µm into the regression analysis: the calculated values for the regression coefficient were, in this case, 2.26 ± 0.43 in arteries and as low as 1.68 ± 0.42 in veins. Thus, the regression line in vessels with these small diameter values diverged clearly from the linear regression in vessels with larger diameters (see Fig. 5.21). As mentioned in section 5.5.10, the vessel diameters which were below 65 µm and were thus too small to be measured with the DVA were determined from the OCT images. However, the smooth transition between the data points measured with DVA and OCT (see Fig. 5.21) indicates that the methods complement one another well and that, consequently, the differing method of diameter determination of the small vessels is not the reason for the differing flow-diameter regression. Moreover, low line rates and small scan regions in the recording of the OCT images used for the diameter determination ensured a high reliability.
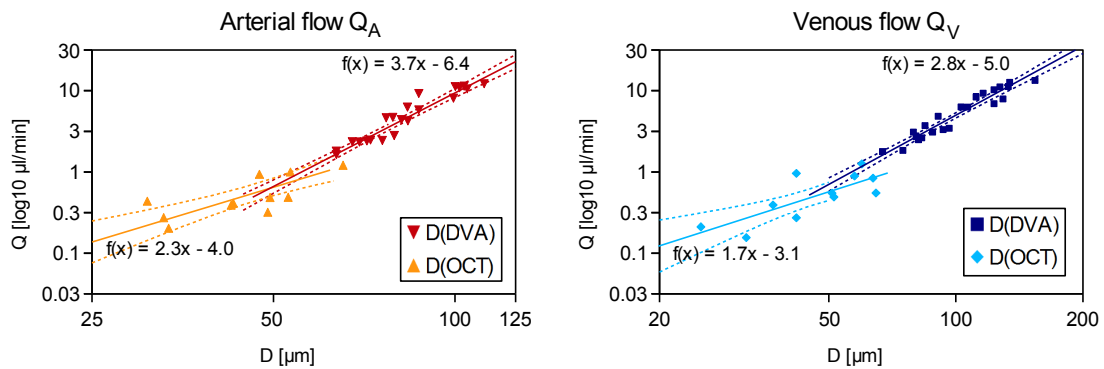
Figure 5.21: Log-log plots of the flow Q over the vessel diameter D for arteries (left) and veins (right) with trend lines (full lines) and 95% confidence intervals (dotted lines).

The amount of data points for small vessels measured in the study on hand was not large enough to allow definite conclusions on the exact values of the regression coefficients. This is also manifest in the fact that the standard deviation given above is much higher for the small vessels than for the large ones. However, the trend towards a different regression line is clearly visible in Fig. 5.21.

A divergence from the linear regression between flow and diameter would also explain why Garhöfer et al. [62], when measuring the relationship between velocity and diameter for the largest vessels of each retinal quadrant, found that several of the regression lines as well as the respective 95% confidence intervals did not include the point (0,0). A divergence from the extrapolated regression line at smaller diameters could lead to the point (0,0) being included.

[xvi]The higher value in arteries may be due to the pulsatility of the flow and the higher velocity in the arteries.

A possible explanation for the change of the relationship between flow and diameter may be the Fåhræus-Lindqvist effect. This effect describes changes in the viscosity of blood due to different vessel diameters: in smaller vessels, the viscosity decreases, thus leading to an increased flow rate (cf. Eq. 5.19). The effect was first described in glass capillaries by Fåhræus and Lindqvist [66], but has, to date, also been reported in several studies in vivo, a number of which are cited in the review article on blood viscosity by Secomb and Pries [67].

Chapter 6

Outlook

6.1   Improvements to the system

As has been shown, the total retinal blood flow measurements with the newly developed OCT system in the configuration explained above yielded promising results in the measurement of young healthy patients. Improvements and additions to the system, both in terms of the setup and the software involved, have been ongoing since the measurements reported here were performed, and are envisaged for the future.

One of the changes included in the meantime was to add an additional hot mirror to the coupling of the OCT to the DVA system. Although the originally included hot mirror fulfilled its function, namely letting the DVA's lighting pass and reflecting the OCT beams into the DVA's beam path, it had an important drawback: keeping in mind that the mirror's thickness of 3.3 mm is non-negligible, the DVA's visible light did not pass the mirror unimpeded but was refracted. In consequence, the OCT beams and the DVA's illumination pathway were not congruent and it could be difficult to pass both beams into the eye, especially in subjects where the pupil did not widen very much when dilated. By adding an additional mirror, inclined in the opposite direction as the originally included one (see Fig. 6.1), the DVA's lighting was refracted out of its original beam path by the newly included mirror, but then refracted back into its path by the hot mirror coupling DVA and OCT.
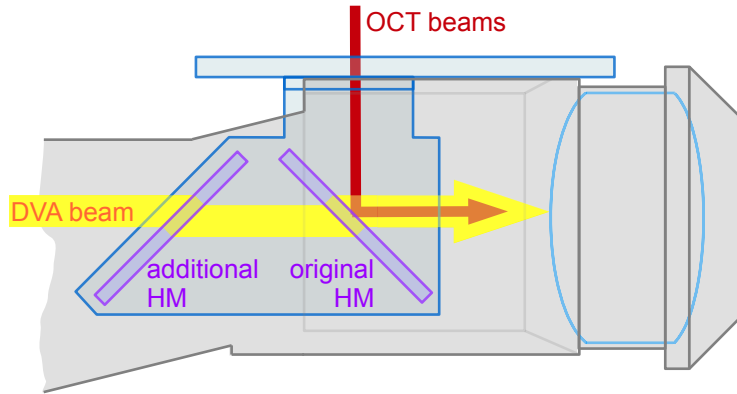
Figure 6.1: The additional hot mirror, included before the original hot mirror, corrects the DVA's beam path.

An additional problem regarding the passing of both the OCT beams and DVA's illumination into the eye is the rotation of the OCT beams. As they are rotated by rotating the beam displacer crystal which produces them, they do not rotate around each other: rather, the ordinary beam remains at the same position, while the extraordinary beam rotates around it. This entails, however, that the beams cannot pass centrally through the lens system. If one would adjust the beams such that they had the same distance from a lens's centre when aligned horizontally, then a rotation of the beam would leave the ordinary beam unmoved but move the extraordinary beam far away from the lens's centre. Thus, the beams have to be 'misaligned' in both their horizontal and vertical positions so as to achieve the optimal alignment for both cases. This effect could be countered if the rotation were not done by rotating the beam displacer, but via an additionally included dove prism, as proposed e.g. in the work by Blatter et al. [49]. Attempts to adapt the setup to include the spacious dove prism are under way.

Regarding the software, a better vessel recognition and image registration, faster loading of the images, and better image correction are envisaged at the moment.

The changes explained above are some of the improvements which would make the measurement process and the data evaluation faster and more easy. Overall, however, the system has been shown to yield reliable, exact measurements already; further improvements can thus be seen as an additional step in the right direction.

6.2 Further measurements

The goal of developing systems to measure the total retinal blood flow is, clearly, not only to confirm or disprove earlier measurements of retinal blood flow values,

but much rather to gain a better understanding of the processes involved in ocular perfusion in general, and in ocular diseases in particular. To this end, it is necessary not only to measure young, healthy subjects, but also to record and compare measurements of elderly subjects or subjects with ocular diseases that have an impact on the eye's perfusion.

Additionally, our group has already begun recording changes of the ocular blood flow to different stimuli such as flicker light and the inhalation of different breathing gases. The continuation of these measurements and evaluation of the data will, hopefully, add to our understanding of the retinal blood flow and shed more light onto the mechanisms underlying ocular diseases which affect the eye's perfusion.

Chapter 7

Conclusions

This thesis presented the results of the development of a novel dual-beam Fourier domain Doppler OCT system with rotatable beams and an integrated Dynamic Vessel Analyser. The system's operational capability could be verified in ex vivo measurements. As was shown in vivo, the system was capable of recording both the vessel diameters and the velocity induced phase shifts in the vessels, thus allowing to measure the total retinal blood flow in arteries as well as in veins.

The value for the total retinal blood flow, measured in the course of this work for four young healthy subjects, was found to be (35.7 ± 4.1) µl/min in the arteries and (36.0 ± 4.5) µl/min in the veins. These values for the total retinal blood flow are in line with retinal blood flow values reported in earlier studies; both studies using OCT and studies relying on other methods of flow measurement such as LDV.

The system's ability to measure very small vessels down to 30 µm in diameter allowed the quantification of the flow in these small vessels. It was thus possible to assess the assumptions and measurements of a number of earlier studies and confirm the supposition that the flow in retinal arteries as well as retinal veins with diameters of 60 µm is about 1 µl/min.

Additionally, measuring the flow in such small vessels gave a further insight into the relationship of blood flow and vessel diameter. According to the results of this study, the log-log regression coefficient between these two quantities is not constant over the whole range of diameters. While, at larger diameters above 60 µm, the

coefficient is around three, which is in line with the predictions of Murray's law, a lower value was found for small vessels. Although further studies with a larger study population will be necessary to precisely determine the reduction of the regression coefficient, the trend is fairly clear.

Overall, the system seems to perform as expected and yielded very promising results. In consequence, it has a high potential for measuring the blood flow in patients suffering from retinal diseases affecting the retinal blood flow such as macular degeneration, diabetic retinopathy and glaucoma. The system shows promise to make a fair contribution to the understanding of the processes involved in such diseases.

Postface

As I stated in the introduction, the aim of my work was to build an OCT system to measure the total retinal blood flow, as the latter is influenced by a number of diseases. The field of optics is one of my favourite areas of physics, and being able to apply theoretical knowledge practically was wonderful – ever much more so, as this was done in an area which is useful and in which developments can make a difference for many people.

Now I am writing the last few sentences of my thesis – the system is built, the goal is achieved, and yet so much still remains to be done: even after over three years of engagement, numerous small improvements could be made and numerous areas of application of the system still wait to be explored.

A quote ascribed to author and engineer Daniel H. Wilson expresses precisely my feeling while writing these words: "But instead of the end, I'm pretty sure I found myself at the start of something." I find myself sincerely hoping that this 'something' I initiated with this work will, one day, really make a difference.

Appendix

A.1 Functionality of optical isolators

Optical isolators (OIs) work via a rotation of the light's polarization direction. Easier to explain are polarization dependent OIs: they consist of a polarization rotator and two polarizers (see Fig. A.1). Light entering the OI in transmission direction is linearly polarized, and then transmitted through the rotator, whereby its polarization is rotated by 45°. The output polarizer's axis is at 45° to that of the input polarizer, so light in transmission direction passes it unimpededly (Fig. A.1a). Light entering in isolation direction, however, is linearly polarized at 45° by the output polarizer, rotated by an additional 45° by the rotator and thus polarized at 90°, which prohibits its passing the input polarizer (Fig. A.1b).
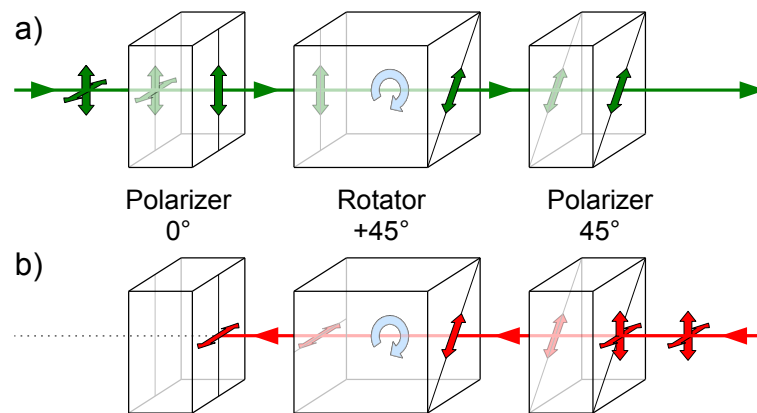
Figure A.1: Schematic drawing of a polarization dependent optical isolator in (a) transmission direction and (b) isolation direction.

Polarization independent OIs operate on a similar principle, but using BDs instead of the input and output polarizers and an additional half-wave plate (see Fig. A.2). In forward direction, light exiting a fiber collimator is split into an ordinary and an extraordinary beam with orthogonal polarization directions by the first BD. As in the polarization dependent OI, the beams are rotated by 45° by the polarization

rotator. Additionally, however, they are rotated by 45° by the half-wave plate. Hence, each beam is now rotated by 90°, so that a second birefringent wedge can recombine the beams and direct them into a collimator. In isolation direction, the light is likewise split into orthogonal polarization components. In this case, however, the half-wave plate and the polarization rotator do not rotate the polarization in the same direction: with respect to an external frame of reference, the polarization's rotation depends on the direction of incidence at a half-wave plate, while the rotation induced by the polarization rotator is always the same (see Fig. A.2b). Consequently, the beams have the same polarization orientation before the rotator and the half-wave plate as behind these two components. The following beam displacer will thus displace the beams even further instead of recombining them, making it impossible for the light to re-enter the following fiber collimator.
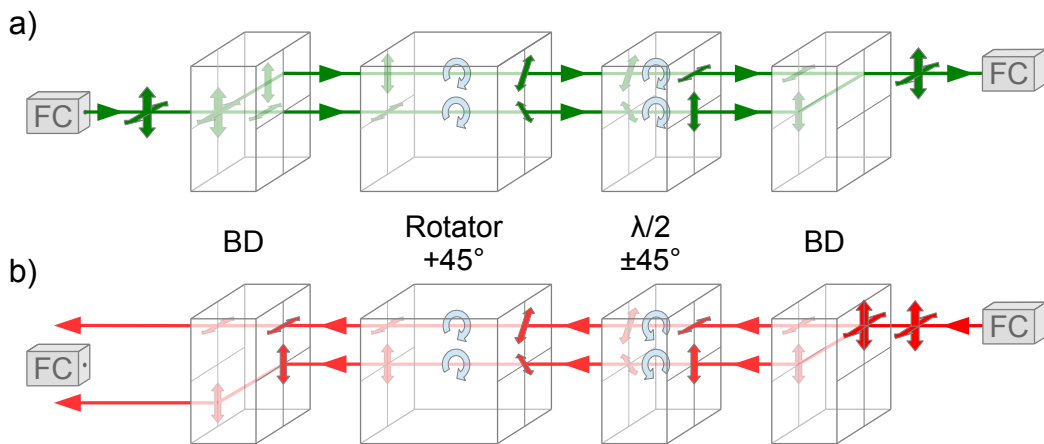
Figure A.2: Schematic drawing of a polarization independent optical isolator in transmission direction (a) and isolation direction (b) with fiber collimators (FCs), beam displacers (BDs), half-wave plate ($\lambda/2$) and Faraday rotator.

A.2 Equations for thick lenses

The thin lens equation with focal length f, object distance $\hat{g}$ and image distance $\hat{b}$,

$$\frac{1}{f} = \frac{1}{\hat{b}} + \frac{1}{\hat{g}}, \tag{A.1}$$

cannot be used directly to find images formed by thick lenses.

To deal with this difficulty, a thick lens can be defined by its *principal planes*. Knowing their location, the thick lens can be treated as if it were a thin lens if the distance between the principal planes is disregarded.
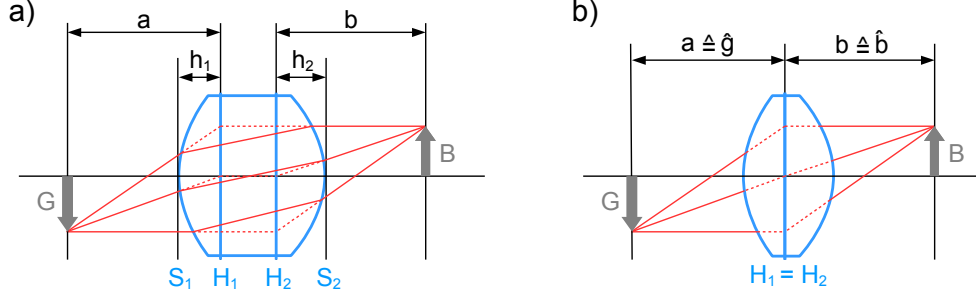
Figure A.3: Imaging through (a) a thick lens with principal planes H_i, vertices S_i; dashed lines are the auxiliary construction of the light path; (b) equivalent thin lens after omitting the distance between the principal planes.

Instead of the thin lens equation A.1, the focal length for thick lenses can be calculated with

$$\frac{1}{f} = \frac{1}{a} + \frac{1}{b}, \tag{A.2}$$

using the equivalences

$$a = \overline{GH_1} = \overline{GS_1} + \overline{S_1H_1}, \tag{A.3}$$
$$b = \overline{H_2B} = \overline{H_2S_2} + \overline{S_2B}, \tag{A.4}$$

where a is equivalent to the object distance and b to the image distance of thin lenses. Here, G is the object, B the image, H_1 and H_2 are the principal planes of the lens, and S_1 and S_2 are the vertices (see Fig. A.3).

A.3   Ray transfer matrix analysis

In the matrix method, a beam is given by two parameters, namely its distance r_i from the optical axis, and its angle θ_i to the optical axis:

$$\begin{pmatrix} r_i \\ \theta_i \end{pmatrix}. \tag{A.5}$$

The propagation of a beam is given by the transfer matrix T,

$$T = \begin{pmatrix} 1 & d \\ 0 & 1 \end{pmatrix}, \tag{A.6}$$

where d is the distance of propagation.

The transmittance of a beam through a lens with the focal length f is given by the lens matrix M,

$$M = \begin{pmatrix} 1 & 0 \\ -\frac{1}{f} & 1 \end{pmatrix}. \tag{A.7}$$

A.4 Handling of the data from the spectrometers

A.4.1 Why rescaling?

Exact relationship between λ_x and x

Due to the geometry of the spectrometers, the distribution of the wavelengths on the cameras' CCD-arrays is not equidistant. For the following data processing, however, it is necessary for the wavelengths to be known. Thus, one needs to find the relation between a point x on the cameras' display and the corresponding wavelength λ_x.

The following explanation can be found in Park et al. [36] and Werkmeister [24], but is given in further detail here.
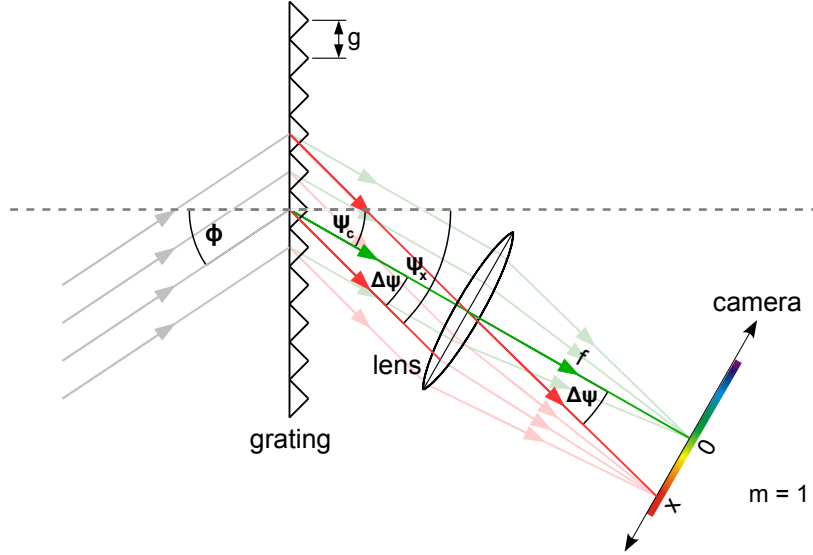
Figure A.4: Geometrical setup of the spectrometer.

As mentioned above, the grating in the experimental setup is followed by a lens and the camera (see Fig. A.4). The order of diffraction which is used in the spectrometer's setup is $m = 1$.

Light passing the spectrometer's grating is diffracted according to the grating equation (Eq. 3.1). The lens and the camera are adjusted to allow the light of a certain 'central wavelength' λ_c (green beams in Fig. A.4) to be focussed onto the centre of the camera's CCD-array. Light with this wavelength λ_c leaves the grating under an angle ψ_c (see Eq. 3.1):

$$\lambda_c = g \cdot (\sin \phi + \sin \psi_c) \quad \Leftrightarrow \quad \psi_c = \arcsin \left(\frac{\lambda_c}{g} - \sin \phi \right). \qquad \text{(A.8)}$$

Light beams with a different wavelength λ_x (e.g. the red beams in Fig. A.4) exit the grating at a different angle, also following the grating equation:

$$\lambda_x = g \cdot (\sin \phi + \sin \psi_x). \tag{A.9}$$

According to their angle of deflection, these beams are focussed onto the camera at a different points with a distance x to the camera's centre. To determine which wavelength λ_x is focussed onto which point x of the camera, it is necessary to establish a relationship between x and λ_x. As can be seen in Fig. A.4, the angle ψ_x and the distance x are related via $\Delta\psi$, where $\Delta\psi = \psi_x - \psi_c$:

$$\tan(\Delta\psi) = \tan(\psi_x - \psi_c) = \frac{x}{f}$$

$$\Rightarrow \psi_x = \psi_c + \arctan\left(\frac{x}{f}\right), \tag{A.10}$$

where f is the distance between lens and camera, which equals the lens's focal length. Inserting Eq. A.10 into Eq. A.9 finally yields a correspondence between x and λ_x, namely

$$\lambda_x = g \cdot \left(\sin \phi + \sin\left[\psi_c + \arctan\left(\frac{x}{f}\right)\right]\right). \tag{A.11}$$

Approximation of the relationship between λ_x and x

To investigate the non-linearity of the relation between λ_x and x, one can use a Taylor expansion. Beforehand, however, it is helpful to rearrange the expression, because Taylor-expanding the sine of a sum containing a tangent is not the easiest solution: Eq. A.11 can be simplified by using the addition theorem for the sine function,

$$\sin(a + b) = \sin a \cdot \cos b + \cos a \cdot \sin b. \tag{A.12}$$

To simplify the calculation of the sine and cosine of a tangent, one can express the cosine in terms of tangents[i]:

$$\cos a = \sqrt{\frac{1}{\frac{1}{\cos^2 a}}} = \sqrt{\frac{1}{\frac{\sin^2 a + \cos^2 a}{\cos^2 a}}} = \sqrt{\frac{1}{\tan^2 a + 1}} = \frac{1}{\sqrt{\tan^2 a + 1}}, \tag{A.13}$$

which, via the relation $\tan a = \frac{\sin a}{\cos a}$, can also be applied to the sine:

$$\sin a = \tan a \cdot \cos a = \tan a \cdot \frac{1}{\sqrt{\tan^2 a + 1}} = \frac{\tan a}{\sqrt{\tan^2 a + 1}}. \tag{A.14}$$

---

[i]Here, it is implicitly assumed that $-\pi/2 < a < \pi/2$ such that $\cos a > 0$.

Equipped with these relations, we can rewrite Eq. A.11: first, by applying the addition theorem Eq. A.12, which leads to

$$\lambda_x = g \cdot \left(\sin\phi + \sin\psi_c \cdot \cos\left[\arctan\left(\frac{x}{f}\right)\right] + \cos\psi_c \cdot \sin\left[\arctan\left(\frac{x}{f}\right)\right] \right); \quad \text{(A.15)}$$

secondly, by substituting the relations given in Eq. A.13 and A.14 for the cosine and the sine, giving

$$\lambda_x = g \cdot \left(\sin\phi + \sin\psi_c \cdot \frac{1}{\sqrt{\tan^2\left[\arctan\left(\frac{x}{f}\right)\right] + 1}} + \right.$$
$$\left. + \cos\psi_c \cdot \frac{\tan\left[\arctan\left(\frac{x}{f}\right)\right]}{\sqrt{\tan^2\left[\arctan\left(\frac{x}{f}\right)\right] + 1}} \right). \quad \text{(A.16)}$$

This can easily be simplified to

$$\lambda_x = g \cdot \left(\sin\phi + \sin\psi_c \cdot \frac{1}{\sqrt{(x/f)^2 + 1}} + \cos\psi_c \cdot \frac{x/f}{\sqrt{(x/f)^2 + 1}} \right). \quad \text{(A.17)}$$

Now we can think of Taylor-expanding the equation for λ_x for small values of $\frac{x}{f}$. To do so, we need the Taylor-expansion for $\frac{1}{\sqrt{1+y}}$, which is

$$\frac{1}{\sqrt{1 + y}} \approx 1 - \tfrac{1}{2}y + \tfrac{3}{8}y^2 + \dots \quad \text{(A.18)}$$

Applying this expansion to Eq. A.17 results in

$$\lambda_x \approx g \cdot \left(\sin\phi + \sin\psi_c \cdot \left[1 - \frac{1}{2}\left(\frac{x}{f}\right)^2 + \dots\right] + \cos\psi_c \cdot \left(\frac{x}{f}\right)\left[1 - \frac{1}{2}\left(\frac{x}{f}\right)^2 + \dots\right] \right)$$
$$= g \cdot \left(\sin\phi + \sin\psi_c + \cos\psi_c\left(\frac{x}{f}\right) - \frac{\sin\psi_c}{2}\left(\frac{x}{f}\right)^2 - \frac{\cos\psi_c}{2}\left(\frac{x}{f}\right)^3 + \dots \right). \quad \text{(A.19)}$$

As $\frac{x}{f}$ is assumed to be small, terms of order 2 or higher can safely be neglected, yielding

$$\lambda_x \approx g \cdot \left(\sin\phi + \sin\psi_c + \cos\psi_c \cdot \left(\frac{x}{f}\right) \right). \quad \text{(A.20)}$$

Justification of the linear approximation of λ_x

The maximal magnitude of the deviation from linearity can be calculated by using the maximally possible value for x in the experimental setup, which equals half the length of the CCD-array (see Fig. A.4), i.e. $x_{\max} = 20.48\,\text{mm}$. As, in the setup, $g = 1/1200\,\text{mm}$, the angles $\phi = \psi_c = 30°$, and the focal length of the lens $f = 150\,\text{mm}$, the exact maximal value can be calculated from Eq. A.11:

$$
\begin{aligned}
\lambda_{x_{\max}}^{\text{exact}} &= g \cdot \left(\sin\phi + \sin\left[\psi_c + \arctan\left(\frac{x}{f} \right) \right] \right) \\
&= \frac{1}{1200} \cdot \left(\sin 30° + \sin\left[30° + \arctan\left(\frac{20.48}{150} \right) \right] \right) \text{mm} \\
&= 927.13\,\text{nm}.
\end{aligned}
\tag{A.21}
$$

This value can then be compared to the approximated maximal value from Eq. A.20:

$$
\begin{aligned}
\lambda_{x_{\max}}^{\text{approx}} &\approx \frac{1}{G} \cdot \left(\sin\phi + \sin\psi_c + \cos\psi_c \cdot \left(\frac{x}{f} \right) \right) \\
&= \frac{1}{1200} \cdot \left(\sin 30° + \sin 30° + \cos 30° \cdot \left(\frac{20.48}{150} \right) \right) \text{mm} \\
&= 931.87\,\text{nm}.
\end{aligned}
\tag{A.22}
$$

The maximum relative error Δ made by the linear approximation can thus be calculated to be

$$
\Delta = \frac{100 \cdot (931.87 - 927.13)}{927.13} = 0.51\%.
\tag{A.23}
$$

This small error can be compensated in the rescaling process.

A.4.2 Rescaling the spectra

Reason for rescaling the spectra

In FDOCT, each pixel i of the CCD records a different wavelength λ_i. As there is a linear relationship between a pixel's number i and its position x, and an (approximately) linear relationship between λ_i and x (cf. Eq. A.20), the values are recorded in λ-space.

FDOCT-experiments are, however, not done to measure wavelengths, but to obtain the intensity values containing the sample's depth information. To obtain such intensity values, the recorded wavelength-values must be converted from the λ-space to the $\frac{1}{\lambda}$-space (also called 'k-space') [68] and then Fourier-transformed, resulting in the intensity values (cf. Eq. 2.25) which were sought.

To describe the desired depth information correctly, the intensity values have to be equidistantly distributed after the Fourier transform. This necessitates that the values were already equidistant in the k-space before applying the Fourier transform. Thus, spectra measured in the λ-space have to be rescaled to fulfil this requirement.
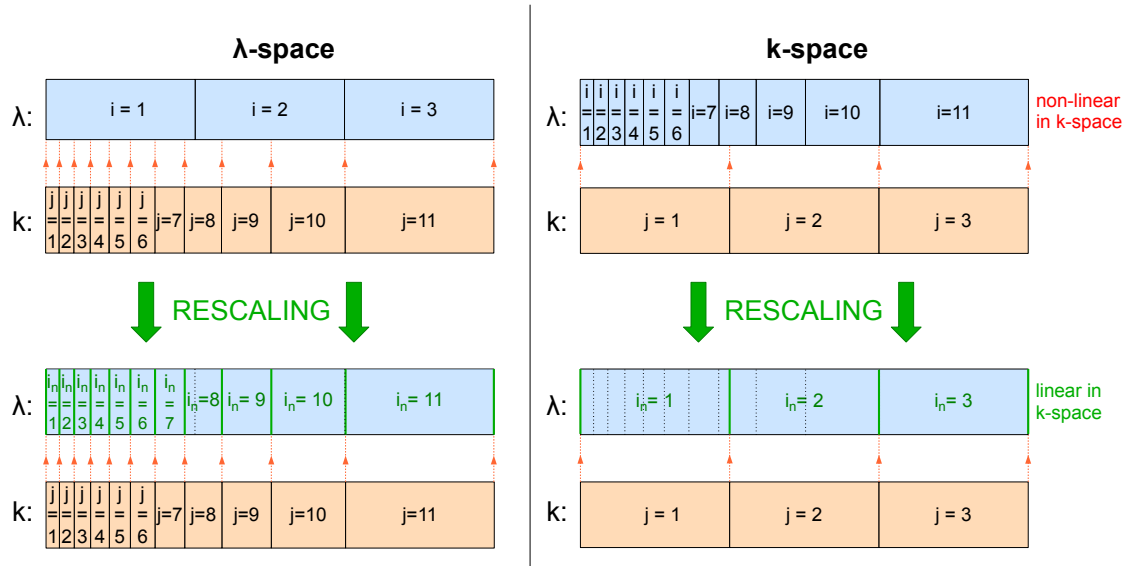
Figure A.5: Rescaling process in λ-space (left) and k-space (right): the values i, which are linear in λ-space, are rescaled to give new values i_{new}, which are linear in k-space.

A schematic drawing of the rescaling process is given in Fig. A.5, assuming that the λ-values are linear in the λ-space (which is the approximation arrived at in subsection A.4.1). In this case, the λ-values (given by the blue bars in Fig. A.5) have equidistant indices i in λ-space (see Fig. A.5, top left). However, as $k = \frac{1}{\lambda}$, they are still non-linearly distributed in k-space (Fig. A.5, top right). Due to their being reciprocal, the opposite is the case for that k-values (orange bars in Fig. A.5): their indices j are non-linear in λ-space, but linear in k-space.

To make the λ-values linear in k-space, the values have to be rescaled. This results in new indices i_{new} for the λ-values. A mathematical approach to the rescaling will be given in the following.

Rescaling under the approximation of linearly distributed λ_x

As was established in subsection A.4.1, the CCD-camera's information is almost equidistant in λ-space. However, we need equal spacing in k-space, and not in λ-space. The following procedure of equalizing in k-space under the assumption of linear λ-values can be found in Baumann [68], and is – with small adaptations – explained here.

In the spectrometers, each wavelength λ_i is imaged onto a pixel i with $i \in [0, N-1]$ on a camera with a CCD-array of N pixels. The shortest detectable wavelength, $\lambda_{\min}$ is imaged onto pixel $i = 0$, the longest wavelength $\lambda_{\max}$ onto pixel $i = N - 1$. If the measured wavelengths λ_i are linearly spaced in λ-space, one finds the relation

$$\lambda_i = \lambda_{\min} + \frac{i}{N-1}(\lambda_{\max} - \lambda_{\min}). \tag{A.24}$$

We know that k is $\frac{1}{\lambda}$, which means that

$$k_{\min} = \frac{1}{\lambda_{\max}}, \tag{A.25}$$

$$k_{\max} = \frac{1}{\lambda_{\min}}. \tag{A.26}$$

As we want the k-values to be equidistant, we want them to follow a relation such as Eq. A.24; i.e. the equally spaced k_j shall follow

$$k_j = k_{\min} + \frac{j}{N-1}(k_{\max} - k_{\min})$$
$$= \frac{1}{\lambda_{\max}} + \frac{j}{N-1}\left(\frac{1}{\lambda_{\min}} - \frac{1}{\lambda_{\max}}\right). \tag{A.27}$$

We now need to know which value λ_i corresponds to a certain one of the equally spaced k_j. As the indices i are chosen such that the k-values are *not* linearly spaced, we will need a new set of indices i_{new} for the λ-values, with

$$k_j = \frac{1}{\lambda_{i_{\text{new}}}}. \tag{A.28}$$

The original i were integers. The new i_{new}, however, will be interpolation indices between the originally discrete i-values. This can also be seen in the top half of Fig. A.5: the rescaling process "cuts" the discrete pixels into smaller parts.

We would now like to find a formula for these new i_{new}, so that we know which k_j corresponds to which $\lambda_{i_{\text{new}}}$. We therefore use Eq. A.28, A.24 and A.27:

$$k_j = \frac{1}{\lambda_{i_{\text{new}}}} = \frac{1}{\lambda_{\min} + \frac{i_{\text{new}}}{N-1}(\lambda_{\max} - \lambda_{\min})} = \frac{1}{\lambda_{\max}} + \frac{j}{N-1}\left(\frac{1}{\lambda_{\min}} - \frac{1}{\lambda_{\max}}\right). \tag{A.29}$$

Expanding the last term,

$$\frac{1}{\lambda_{\max}} + \frac{j}{N-1}\left(\frac{1}{\lambda_{\min}} - \frac{1}{\lambda_{\max}}\right) = \frac{(N-1)\lambda_{\min} + j \cdot (\lambda_{\max} - \lambda_{\min})}{\lambda_{\max} \cdot \lambda_{\min} \cdot (N-1)},$$

Eq. A.29 can be rearranged:

$$\lambda_{\min} + \frac{i_{\text{new}}}{N-1}(\lambda_{\max} - \lambda_{\min}) = \frac{\lambda_{\max} \cdot \lambda_{\min} \cdot (N-1)}{(N-1)\lambda_{\min} + j \cdot (\lambda_{\max} - \lambda_{\min})}. \tag{A.30}$$

Expressing i_{new} results in

$$i_{\text{new}} = \frac{N-1}{\lambda_{\text{max}} - \lambda_{\text{min}}} \cdot \left(\frac{\lambda_{\text{max}} \cdot \lambda_{\text{min}} \cdot (N-1)}{(N-1) \cdot \lambda_{\text{min}} + j \cdot (\lambda_{\text{max}} - \lambda_{\text{min}})} - \lambda_{\text{min}} \right)$$

$$= \frac{N-1}{\lambda_{\text{max}} - \lambda_{\text{min}}} \cdot \left(\frac{\lambda_{\text{max}} \cdot (N-1)}{(N-1) + j \cdot \left(\frac{\lambda_{\text{max}}}{\lambda_{\text{min}}} - 1 \right)} \right.$$

$$\left. - \lambda_{\text{min}} \cdot \frac{(N-1) + j \cdot \left(\frac{\lambda_{\text{max}}}{\lambda_{\text{min}}} - 1 \right)}{(N-1) + j \cdot \left(\frac{\lambda_{\text{max}}}{\lambda_{\text{min}}} - 1 \right)} \right)$$

$$= \frac{N-1}{\lambda_{\text{max}} - \lambda_{\text{min}}} \cdot \left(\frac{\lambda_{\text{max}}(N-1) - \lambda_{\text{min}}(N-1) - j(\lambda_{\text{max}} - \lambda_{\text{min}})}{(N-1) + j \cdot \left(\frac{\lambda_{\text{max}}}{\lambda_{\text{min}}} - 1 \right)} \right)$$

$$\Rightarrow \quad i_{\text{new}} = \frac{(N-1) \cdot (N-1-j)}{(N-1) + j \cdot \left(\frac{\lambda_{\text{max}}}{\lambda_{\text{min}}} - 1 \right)}, \tag{A.31}$$

which is the relation between the index of interpolation i_{new} of the λ-values and a certain index j of the k-values.

Rescaling of the exact λ_x

Of course, instead of using the linear approximation for λ_x, one can also use the exact equation (Eq. A.11) to calculate the index of interpolation for the rescaling; the formula is then more complicated, as it contains trigonometric functions. It is given here for the sake of completeness. To prevent confusion, the new index using the exact equation will be called $i_{\text{new}}^{\text{ex}}$.

Using the exact equation A.11, Eq. A.29 changes to

$$k_j = \frac{1}{\lambda_{i_{\text{new}}^{\text{ex}}}} = \frac{1}{\frac{1}{G} \cdot \left(\sin \phi + \sin \left[\psi_c + \arctan \left(\frac{i_{\text{new}}^{\text{ex}}}{f} \right) \right] \right)}$$

$$= \frac{1}{\lambda_{\text{max}}} + \frac{j}{N-1} \left(\frac{1}{\lambda_{\text{min}}} - \frac{1}{\lambda_{\text{max}}} \right). \tag{A.32}$$

Analogous to Eq. A.30, this can be rewritten as

$$\frac{1}{G} \cdot \left(\sin \phi + \sin \left[\psi_c + \arctan \left(\frac{i_{\text{new}}^{\text{ex}}}{f} \right) \right] \right) = \frac{\lambda_{\text{max}} \cdot \lambda_{\text{min}} \cdot (N-1)}{(N-1)\lambda_{\text{min}} + j \cdot (\lambda_{\text{max}} - \lambda_{\text{min}})},$$

which can be reformulated to

$$i_{\text{new}}^{\text{ex}} = \tan \left[\arcsin \left(\frac{\lambda_{\text{max}} \cdot \lambda_{\text{min}} \cdot (N-1) \cdot G}{(N-1)\lambda_{\text{min}} + j \cdot (\lambda_{\text{max}} - \lambda_{\text{min}})} - \sin \phi \right) - \sin \psi_c \right] \cdot f, \tag{A.33}$$

which is the exact equivalent of Eq. A.31. However, the approximated equation is exact enough and was thus implemented in the experiment's data processing.

A.5 Fitting

Assuming that a set of data points can be described by the linear model

$$f(D) = A \cdot (D - D_0) + B, \tag{A.34}$$

one needs to determine the fit parameters A and B such that the model best describes the data. The variable D_0 in this equation can be chosen arbitrarily; a good choice of D_0 can make the fit more stable, as will be mentioned below.

For a certain data point D_i with a value v_i, the residual r_i, i.e. the deviation of a data point from the linear fit, is given by

$$r_i(A, B) = v_i - f(D_i). \tag{A.35}$$

The sum of the squared residuals, S, for m data points is defined as

$$S(A, B) = \sum_{i=1}^{m} (r_i(A, B))^2 \,. \tag{A.36}$$

For an optimal fit, the sum of squared residuals must be minimized, which implies that

$$\frac{\partial S}{\partial A} = 0 \quad \text{and} \quad \frac{\partial S}{\partial B} = 0. \tag{A.37}$$

This leads to the system of equations

$$\sum v_i \cdot (D_i - D_0) = A \cdot \sum (D_i - D_0)^2 + B \cdot \sum (D_i - D_0)$$
$$\sum v_i = A \cdot \sum (D_i - D_0) + B \cdot \sum 1,$$

which can be written more compactly in matrix form:

$$\begin{pmatrix} \sum (D_i - D_0)^2 & \sum (D_i - D_0) \\ \sum (D_i - D_0) & \sum 1 \end{pmatrix} \cdot \begin{pmatrix} A \\ B \end{pmatrix} = \begin{pmatrix} \sum v_i \cdot (D_i - D_0) \\ \sum v_i \end{pmatrix}. \tag{A.38}$$

The first matrix of Eq. A.38 is usually termed $(J^T J)$, i.e.

$$(J^T J) \cdot \begin{pmatrix} A \\ B \end{pmatrix} = \begin{pmatrix} \sum v_i \cdot (D_i - D_0) \\ \sum v_i \end{pmatrix}. \tag{A.39}$$

To solve this system of equations for A and B, $(J^T J)$ has to be inverted, which is relatively easy for 2×2 matrices using the relation

$$\begin{pmatrix} a & b \\ c & d \end{pmatrix}^{-1} = \frac{1}{\det} \cdot \begin{pmatrix} d & -b \\ -c & a \end{pmatrix} \cdot = \frac{1}{ad - bc} \cdot \begin{pmatrix} d & -b \\ -c & a \end{pmatrix}, \qquad \text{(A.40)}$$

where "det" stands for the determinant of the matrix $\left(\begin{smallmatrix} a & b \\ c & d \end{smallmatrix}\right)$. For the matrix $(J^T J)$ from Eq. A.38, the determinant is

$$\det(J^T J) = \sum (D_i - D_0)^2 \cdot \sum 1 - \left(\sum (D_i - D_0) \right)^2. \qquad \text{(A.41)}$$

Thus, one arrives at the equations for the linear fit

$$\begin{pmatrix} A \\ B \end{pmatrix} = \underbrace{\frac{1}{\det(J^T J)} \cdot \begin{pmatrix} \sum 1 & -\sum(D_i - D_0) \\ -\sum(D_i - D_0) & \sum(D_i - D_0)^2 \end{pmatrix}}_{(J^T J)^{-1}} \begin{pmatrix} \sum v_i \cdot (D_i - D_0) \\ \sum v_i \end{pmatrix}.$$

or, explicitly

$$A = \frac{1}{\det(J^T J)} \cdot \left(\sum 1 \cdot \sum v_i \cdot (D_i - D_0) - \sum (D_i - D_0) \cdot \sum v_i \right), \qquad \text{(A.42)}$$

$$B = \frac{1}{\det(J^T J)} \cdot \left(-\sum (D_i - D_0) \cdot \sum v_i \cdot (D_i - D_0) + \sum (D_i - D_0)^2 \cdot \sum v_i \right). \qquad \text{(A.43)}$$

If the parameter D_0 is suitably chosen (namely as mean of the D_i) only the diagonal terms remain; A and B thus become statistically independent, which simplifies the calculation.

The matrix

$$K = \frac{S}{m - n} (J^T J)^{-1} = \begin{pmatrix} \sigma_A^2 & \text{cov}(A, B) \\ \text{cov}(A, B) & \sigma_B^2 \end{pmatrix} \qquad \text{(A.44)}$$

is called covariance matrix [69, 70]. Here, S is, as defined above, the sum of the square residuals and m is the number of data points. n is the number of fit parameters (in our case two, namely A and B). The covariance matrix' elements are the squared standard deviations (σ_A^2, σ_B^2) and the covariance of A and B. The error $\Delta f(D)$ of the model can now be written as

$$\Delta f(D) = \sqrt{\left(\frac{\partial f}{\partial A}\big|_D \quad \frac{\partial f}{\partial B}\big|_D \right) \cdot K \cdot \begin{pmatrix} \frac{\partial f}{\partial A}\big|_D \\ \frac{\partial f}{\partial B}\big|_D \end{pmatrix}}. \qquad \text{(A.45)}$$

According to Eq. A.34,

$$\frac{\partial f}{\partial A}\bigg|_D = D - D_0, \quad \text{and} \quad \frac{\partial f}{\partial B}\bigg|_D = 1.$$

Consequently, the error of the model for a certain value D is

$$\Delta f(D) = \sqrt{(D - D_0)^2 \cdot \sigma_A^2 + 2 \cdot (D - D_0) \cdot \mathrm{cov}(A, B) + \sigma_B^2}. \qquad \text{(A.46)}$$

The 95% confidence interval is used in many graphs to indicate the reliability of the linear fit through the data points. For a normal distribution, about 95% of the values lie within two standard deviations of the mean. Thus, the 95% confidence interval is $f(D) \pm 2\Delta f(D)$.

A.6 Main Data Acqusition programme

'MainDataAcqu.vi' is the LabVIEW programme used to control the recording of the OCT images. The basic structure of the programme is a sequence structure with a number of frames (see Fig. A.6). The first few frames of the sequence structure contain the setting of the cameras' shading files and shading modes, the initialisation of the programme's variables, and the frame grabbers' setup. The next frame's content is a while-loop, governing the continuous acquisition and display of graphs necessary for the measurement preparation and alignment (see Fig. A.7). In the following, the continuous acquisition is stopped and the setup of the required number of buffers is executed. After waiting for the acknowledgement from the user, frames are recorded until the buffers are filled. In the following frames of the sequence structure, the frames and a file containing additional information on the acquisition are saved to the hard disk, the buffers deleted, the frame grabber boards closed and the variables reset to their default values.

The while-loop mentioned above, which controls the continuous acquisition and displays the graphs necessary for the measurement preparation and alignment, is detailed in Fig. A.7. It contains all the steps which are needed to yield the amplitude images and phase images gained from the OCT measurements. These steps include recording and displaying the interference spectra, rescaling them to cater for the non-uniformity of the wavelength distribution on the cameras' sensors (cf. section A.4.1), recording and subtracting a reference spectrum, Fourier transforming the data and splitting it into its radial and angular components, i.e. into amplitude and phase images, respectively.
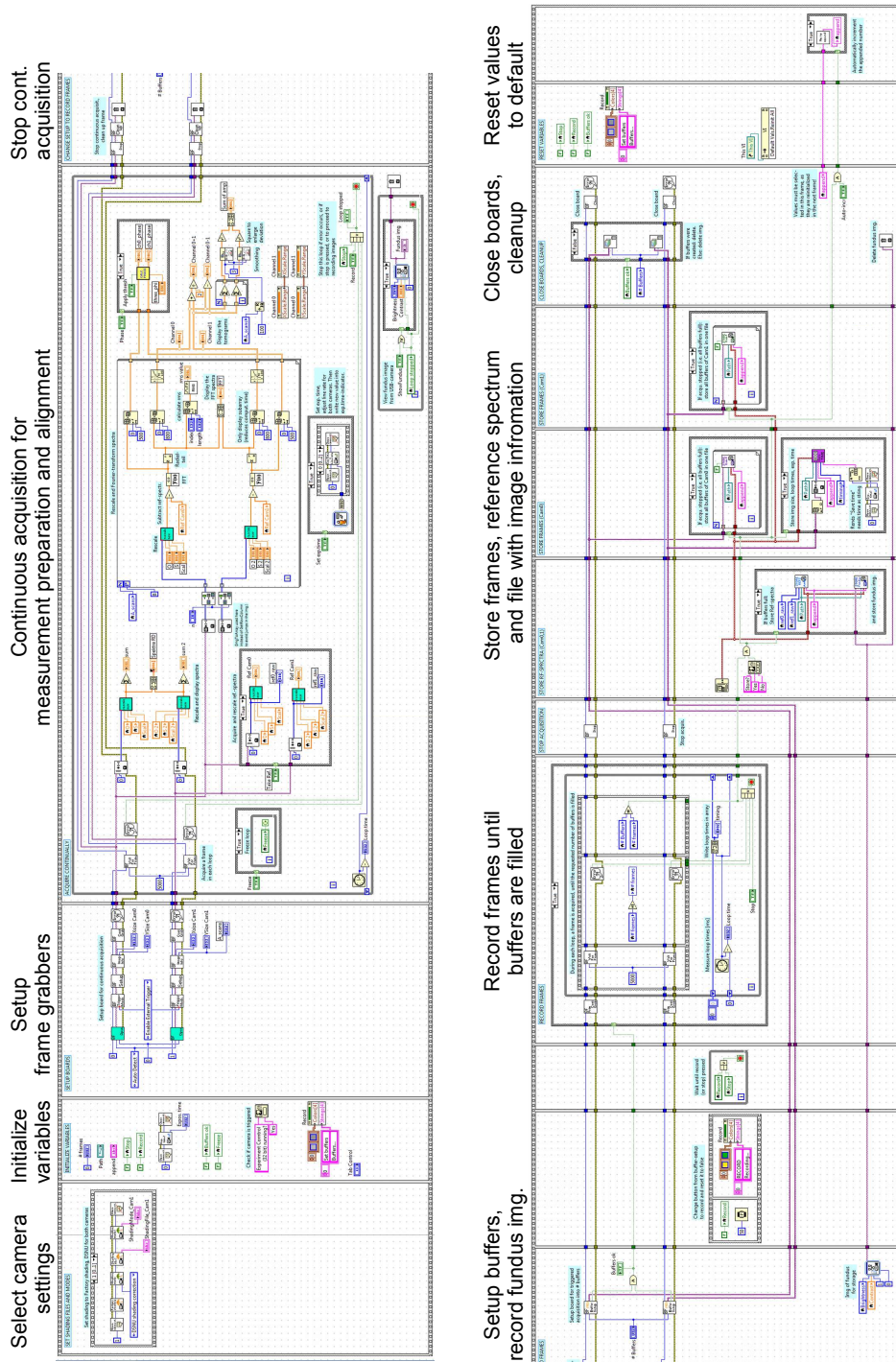
Figure A.6: Block diagram of the programme used to acquire and store the OCT-images; explanations of the various frames of the sequence structure are given above.
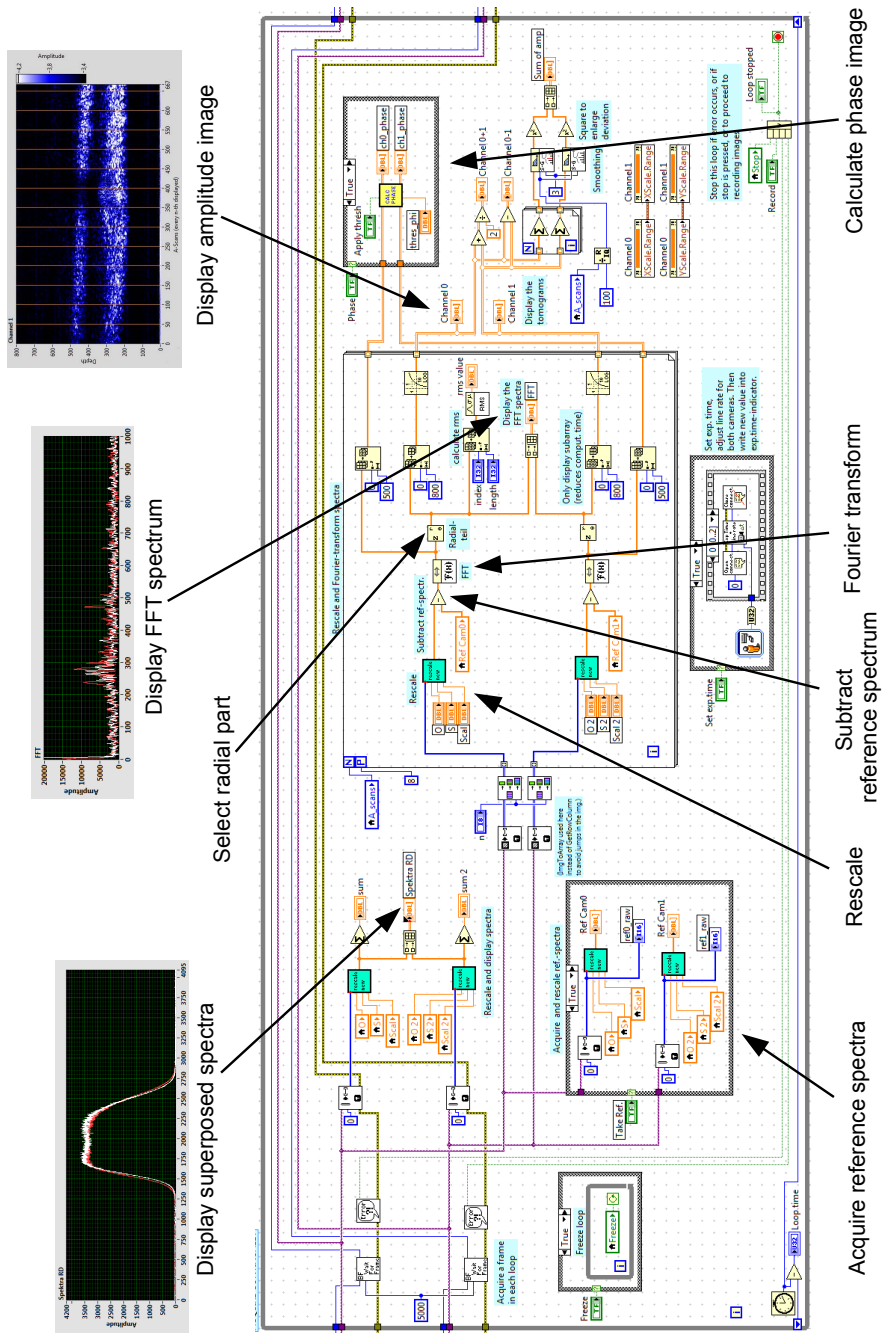
Figure A.7: Block diagram of the while-loop governing the continuous acquisition and display in the MainDataAcquisition programme including all relevant image calculation steps.

A.7 Subjects' fundus images

The images given in Fig. A.8 show the four subjects' fundus images with vessel labels I1, I2, etc. (for an explanation of the designations see section 5.3) and the scanning patterns (cf. section 5.4.1). In all four subjects, the right eye (oculus dexter, OD) was measured.
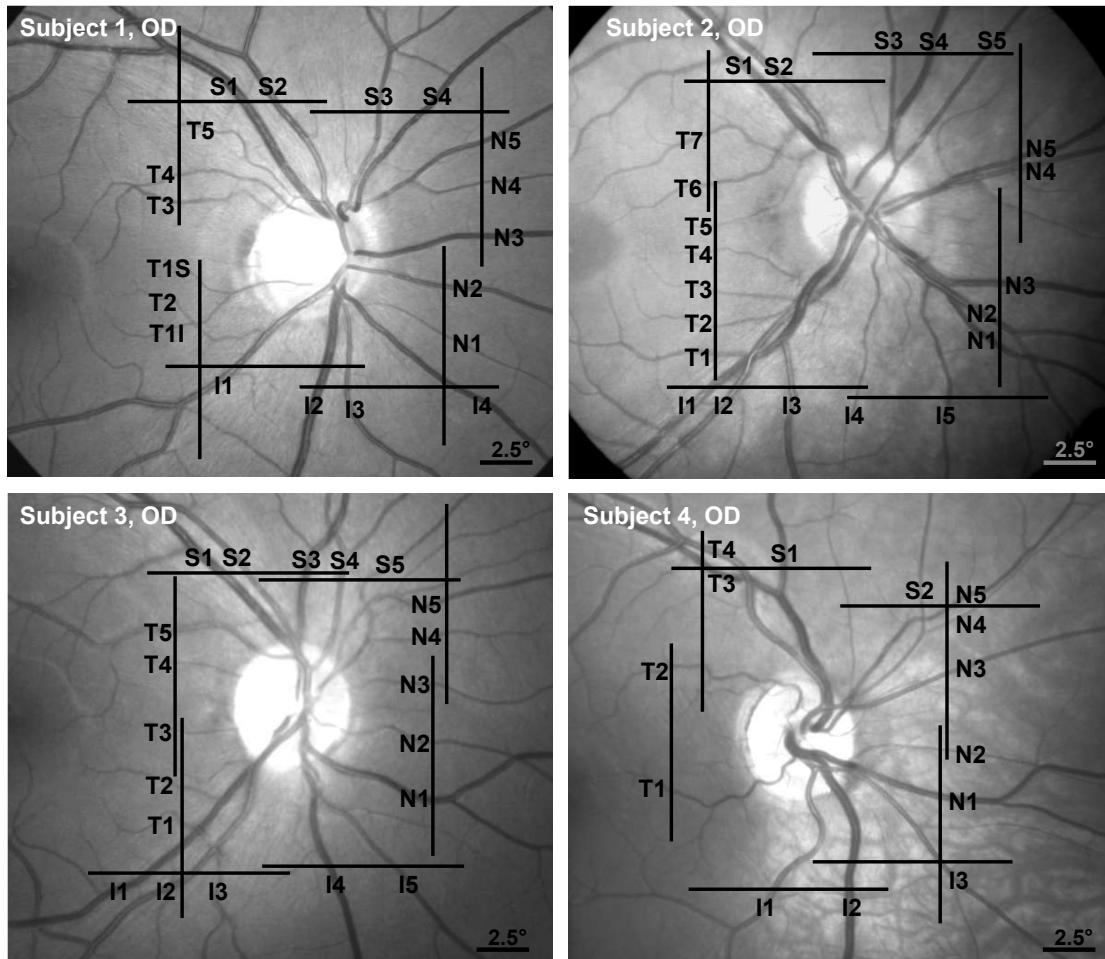
Figure A.8: Fundus images of the measured subjects' right eyes. Letters and numbers label the vessels according to their position (inferior, superior, nasal or temporal of the ONH). Black lines denote the scan lines.

A.8 Measured data

Tables A.1 to A.4 list the retinal blood flow data of all four measured subjects. The tables include, for each vessel, the number (#) with which it is labelled in the fundus images (Fig. A.8), its type ('A' for artery or 'V' for vein), the exposure time τ of the measurement, the vessel's *en-face* angle β, the mean phase shift difference $\Delta\phi_{\mathrm{mean}}$, the resulting velocity v in the vessel, the vessel's diameter D and the calculated flow Q in the vessel. If more than one measurement on the vessel in question was evaluated, the tables also include these measurements averaged velocity v_{avg} and flow Q_{avg}.

Table A.1: Measured data for subject 1, including vessel designation, vessel type (vein or artery), exposure time, mean phase difference, velocity, diameter and flow for each measurement, as well as mean velocity and mean flow for multiple measurements of the same vessel.

#	Type	τ [µs]	β [deg]	$\Delta\phi_{\mathrm{mean}}$ [rad]	v [mm/s]	v_{avg} [mm/s]	D [µm]	Q [µl/min]	Q_{avg} [µl/min]
I1	A	25	45	0.88850	25.00	22.36	102	12.19	10.90
	A	25	43	0.72455	19.71		102	9.61	
I2	V	25	15	0.57823	11.91	13.46	133	9.92	11.21
	V	25	10	0.74321	15.02		133	12.50	
I3	A	25	4	0.75198	15.00	14.02	82	4.70	4.40
	A	25	4	0.65402	13.05		82	4.09	
I4	V	25	52	0.29136	9.42	7.94	82	2.95	2.49
	V	25	56	0.18164	6.46		82	2.03	
S1	V	25	34	0.62034	14.89	14.93	134	12.59	12.62
	V	25	34	0.62375	14.97		134	12.65	
S2	A	25	47	0.73064	21.32	20.31	105	11.02	10.50
	A	25	31	0.83135	19.30		105	9.97	
S3	A	25	2	0.67003	13.34	12.92	84	4.39	4.25
	A	25	2	0.62755	12.49		84	4.11	
S4	V	25	48	0.41986	12.49	11.02	85	4.21	3.72
	V	25	39	0.37315	9.55		85	3.22	
N1	V	25	29	0.20004	4.55	4.55	40	0.35	0.35
N2	A	25	16	0.70163	14.52	12.93	79	4.22	3.76
	A	25	10	0.56106	11.34		79	3.30	
N3	V	25	2	0.42905	8.54	9.06	81	2.61	2.77
	V	25	1	0.48133	9.58		81	2.93	
N4	A	25	13	0.20944	4.28	5.06	42	0.36	0.43
	A	25	0	0.29387	5.85		42	0.49	
N5	A	25	20	0.47685	10.10	9.98	73	2.50	2.47
	A	25	25	0.44919	9.86		73	2.44	

#	Type	τ [µs]	β [deg]	$\Delta\phi_{\mathrm{mean}}$ [rad]	v [mm/s]	v_{avg} [mm/s]	D [µm]	Q [µl/min]	Q_{avg} [µl/min]
T1I	V	80	7	1.75315	11.57	11.57	42	0.96	0.96
T2	A	50	23	0.60804	6.82	8.60	31	0.31	0.44
	A	50	23	0.92423	10.37		34	0.57	
T3	A	25	8	0.20506	4.12	4.12	53	0.55	0.55
T4	V	80	12	1.10488	7.40	7.40	60	1.26	1.26
T5	A	80	21	1.25518	8.81	8.81	48	0.94	0.94

Table A.2: Measured data for subject 2, including vessel designation, vessel type (vein or artery), exposure time, mean phase difference, velocity, diameter and flow for each measurement, as well as mean velocity and mean flow for multiple measurements of the same vessel.

#	Type	τ [µs]	β [deg]	$\Delta\phi_{\mathrm{mean}}$ [rad]	v [mm/s]	v_{avg} [mm/s]	D [µm]	Q [µl/min]	Q_{avg} [µl/min]
I1	V	25	60	0.38704	14.82	14.68	116	9.40	9.31
	V	25	60	0.37961	14.54		116	9.22	
I2	A	25	31	0.79795	17.83	17.38	99	8.30	8.09
	A	25	36	0.71504	16.93		99	7.88	
I3	V	25	7	0.58094	11.21	10.43	79	3.33	3.10
	V	25	8	0.49950	9.66		79	2.87	
I4	A	80	21	0.68129	4.60	4.56	43	0.39	0.39
	A	80	21	0.66826	4.51		43	0.39	
I5	A	25	7	0.27813	5.37	5.37	51	0.67	0.67
S1	V	25	47	0.49553	13.91	14.27	112	8.17	8.38
	V	25	47	0.52079	14.62		112	8.59	
S2	A	25	46	0.38441	10.60	13.22	99	4.93	6.16
	A	25	46	0.57468	15.84		99	7.38	
S3	A	25	2	0.40444	7.75	8.54	64	1.48	1.63
	A	25	2	0.48739	9.34		64	1.78	
S4	V	25	10	0.43585	8.48	8.48	88	3.10	3.10
S5	A	25	37	0.39394	9.45	9.45	64	1.80	1.80
N1	V	25	34	0.29914	6.91	6.97	75	1.83	1.85
	V	25	34	0.30421	7.03		75	1.86	
N2	A	25	32	0.48436	10.94	9.47	79	3.25	2.81
	A	25	32	0.35419	8.00		79	2.37	
N3	V	25	3	0.37234	7.14	8.09	93	2.93	3.32
	V	25	3	0.41385	7.94		93	3.26	
	V	25	3	0.47868	9.18		93	3.77	
N4	A	25	23	0.40489	8.42	10.00	72	2.03	2.41

#	Type	τ [μs]	β [deg]	$\Delta\phi_{\mathrm{mean}}$ [rad]	v [mm/s]	v_{avg} [mm/s]	D [μm]	Q [μl/min]	Q_{avg} [μl/min]
	A	25	23	0.55664	11.58		72	2.79	
N5	V	25	11	0.43077	8.40	8.40	67	1.79	1.79
T1	A	80	2	1.52380	9.61	9.51	86	3.34	3.30
	A	80	2	1.49070	9.41		86	3.27	
T2	V	80	12	0.71791	4.63	4.39	64	0.89	0.84
	V	80	12	0.64539	4.16		64	0.80	
T3	A	80	6	0.93414	5.92	7.42	53	0.80	1.00
	A	80	6	1.40564	8.91		53	1.20	
T4	V	80	12	0.85995	5.54	5.54	38	0.37	0.37
T5	A	80	10	0.52691	3.37	3.81	34	0.18	0.20
	A	80	10	0.66238	4.24		34	0.23	
T6	V	80	8	0.57417	3.66	3.94	52	0.46	0.49
	V	80	8	0.66238	4.22		52	0.53	
T7	A	80	24	0.89070	6.15	6.03	65	1.24	1.21
	A	80	24	0.85673	5.91		65	1.19	

Table A.3: Measured data for subject 3, including vessel designation, vessel type (vein or artery), exposure time, mean phase difference, velocity, diameter and flow for each measurement, as well as mean velocity and mean flow for multiple measurements of the same vessel.

#	Type	τ [μs]	β [deg]	$\Delta\phi_{\mathrm{mean}}$ [rad]	v [mm/s]	v_{avg} [mm/s]	D [μm]	Q [μl/min]	Q_{avg} [μl/min]
I1	V	25	51	0.40802	12.42	12.29	103	6.20	6.32
	V	25	51	0.44148	13.44		103	6.71	
	V	25	50	0.39756	11.85		103	5.91	
	V	25	50	0.38479	11.47		109	6.47	
I2	A	25	47	0.83718	23.52	23.76	100	11.11	11.22
	A	25	47	0.70431	19.78		100	9.34	
	A	25	29	1.13653	24.89		100	11.76	
	A	25	29	1.22482	26.83		100	12.67	
I3	A	80	13	0.59216	3.83	3.68	53	0.51	0.49
	A	80	13	0.54441	3.52		53	0.47	
I4	V	25	22	0.33580	6.94	7.87	96	3.04	3.45
	V	25	22	0.45053	9.31		96	4.08	
	V	25	22	0.35629	7.36		96	3.22	
I5	A	25	42	0.36354	9.37	10.27	70	2.13	2.34
	A	25	42	0.56957	14.68		70	3.34	
	A	25	42	0.26197	6.75		70	1.54	

#	Type	τ [µs]	β [deg]	$\Delta\phi_{\mathrm{mean}}$ [rad]	v [mm/s]	v_{avg} [mm/s]	D [µm]	Q [µl/min]	Q_{avg} [µl/min]
S1	V	25	44	0.57508	15.32	14.59	127	11.64	11.09
	V	25	45	0.51197	13.87		127	10.54	
S2	A	25	36	1.06764	25.28	25.79	87	9.05	9.23
	A	25	50	0.77958	23.24		87	8.31	
	A	25	50	0.96840	28.86		87	10.33	
S3	V	25	11	0.57526	11.23	11.73	107	6.01	6.28
	V	25	12	0.62472	12.24		107	6.55	
S4	A	25	6	0.99041	19.08	19.12	83	6.26	6.27
	A	25	6	0.99422	19.15		83	6.28	
S5	V	80	52	0.35682	3.66	4.47	51	0.45	0.55
	V	80	52	0.24334	2.49		51	0.31	
	V	80	38	0.64833	5.19		51	0.64	
	V	80	38	0.81885	6.55		51	0.80	
N1	V	25	7	0.63405	12.24	12.46	91	4.76	4.85
	V	25	7	0.65752	12.69		91	4.94	
N3	A	80	4	0.98973	6.26	4.75	43	0.55	0.41
	A	80	4	0.51245	3.24		43	0.28	
N4	V	80	4	0.62046	3.92	3.28	42	0.33	0.27
	V	80	4	0.41739	2.64		42	0.22	
N5	A	25	25	0.33897	7.17	10.88	68	1.55	2.35
	A	25	24	0.68929	14.46		68	3.12	
	A	25	25	0.52083	11.01		68	2.38	
T5	A	25	20	0.80711	16.45	16.61	77	4.59	4.63
	A	25	20	0.82207	16.76		77	4.68	
T1	A	80	24	0.79042	5.46	5.59	33	0.28	0.29
	A	80	24	0.82752	5.71		33	0.29	
T2	V	80	14	0.98850	6.43	6.07	37	0.41	0.39
	V	80	14	0.87897	5.71		37	0.37	
T3	V	80	10	1.11802	7.16	7.16	25	0.21	0.21
T4	V	80	0	0.46861	2.96	3.23	32	0.14	0.16
	V	80	0	0.55604	3.51		32	0.17	

Table A.3 – *Continued from the previous page*

Table A.4: Measured data for subject 4, including vessel designation, vessel type (vein or artery), exposure time, mean phase difference, velocity, diameter and flow for each measurement, as well as mean velocity and mean flow for multiple measurements of the same vessel.

#	Type	τ [µs]	β [deg]	$\Delta\phi_{\mathrm{mean}}$ [rad]	v [mm/s]	v_{avg} [mm/s]	D [µm]	Q [µl/min]	Q_{avg} [µl/min]
I1	A	25	31	1.18197	26.51	22.53	104	13.39	11.38
	A	25	25	0.87422	18.54		104	9.37	
I2	V	25	1	0.50509	9.71	11.97	154	10.82	13.33
	V	25	1	0.68191	13.11		154	14.61	
	V	25	1	0.67986	13.07		154	14.56	
I3	A	25	38	0.71589	17.47	16.20	87	6.25	5.80
	A	25	38	0.71099	17.35		87	6.20	
	A	25	52	0.47513	14.84		87	5.31	
	A	25	52	0.48568	15.17		87	5.43	
S1	V	25	4	0.50450	9.72	10.05	129	7.64	7.90
	V	25	3	0.54051	10.41		129	8.18	
	V	25	1	0.52131	10.02		129	7.88	
S2	A	25	7	0.43897	8.50	9.00	76	2.31	2.44
	A	25	7	0.45618	8.84		76	2.40	
	A	25	7	0.49839	9.65		76	2.62	
N1	V	25	13	0.48681	9.61	9.69	123	6.85	6.91
	V	25	13	0.49526	9.77		123	6.97	
N2	A	80	7	0.61418	3.92	4.20	49	0.45	0.48
	A	80	7	0.70346	4.49		49	0.52	
N3	A	25	20	0.79096	16.18	15.99	79	4.75	4.70
	A	25	20	0.77261	15.81		79	4.64	
N4	A	80	29	0.38887	2.81	2.81	49	0.32	0.32
N5	V	25	33	0.35600	8.16	8.09	83	2.65	2.63
	V	25	33	0.34978	8.02		83	2.60	
T1	V	80	22	0.47751	3.26	2.78	65	0.64	0.55
	V	80	22	0.33798	2.31		65	0.46	
T2	V	80	12	0.99542	6.44	5.69	58	1.01	0.89
	V	80	12	0.76408	4.94		58	0.77	
T3	V	25	30	0.53096	11.79	14.35	123	8.40	10.23
	V	25	38	0.69362	16.92		123	12.06	
T4	A	25	19	0.98053	19.94	20.68	112	11.73	12.16
	A	25	19	1.05338	21.42		112	12.60	

Bibliography

[1] J. E. Grunwald, C. E. Riva, J. Baine, and A. J. Brucker. Total retinal volumetric blood flow rate in diabetic patients with poor glycemic control. *Investigative Ophthalmology and Visual Science*, 33(2):356–63, 1992. URL `http://www.iovs.org/content/33/2/356.abstract`.

[2] B. Pemp, E. Polska, G. Garhöfer, M. Bayerle-Eder, A. Kautzky-Willer, and L. Schmetterer. Retinal blood flow in type 1 diabetic patients with no or mild diabetic retinopathy during euglycemic clamp. *Diabetes Care*, 33(9):2038–2042, 2010. doi: 10.2337/dc10-0502 1935-5548.

[3] J. Durham and I. Herman. Microvascular modifications in diabetic retinopathy. *Current Diabetes Reports*, 11(4):253–264, 2011. doi: 10.1007/s11892-011-0204-0.

[4] B. Pemp and L. Schmetterer. Ocular blood flow in diabetes and age-related macular degeneration. *Canadian Journal of Ophthalmology*, 43(3):295–301, 2008. doi: 10.3129/i08-049.

[5] B. Feigl. Age-related maculopathy – linking aetiology and pathophysiological changes to the ischaemia hypothesis. *Progress in Retinal and Eye Research*, 28 (1):63–86, 2009. doi: 10.1016/j.preteyeres.2008.11.004.

[6] A. Popa-Cherecheanu, G. Garhöfer, D. Schmidl, R. Werkmeister, and L. Schmetterer. Ocular perfusion pressure and ocular blood flow in glaucoma. *Current Opinion in Pharmacology*, 13(1):36–42, 2013. doi: 10.1016/j.coph.2012.09.003.

[7] V. P. Costa, A. Harris, D. Anderson, R. Stodtmeister, F. Cremasco, H. Kergoat, J. Lovasik, I. Stalmans, O. Zeitz, I. Lanzl, K. Gugleta, and L. Schmetterer. Ocular perfusion pressure in glaucoma. *Acta Ophthalmologica*, 92(4):e252–e266, 2014. doi: 10.1111/aos.12298.

[8] T. Y. Wong, R. Klein, D. J. Couper, L. S. Cooper, E. Shahar, L. D. Hubbard, M. R. Wofford, and A. R. Sharrett. Retinal microvascular abnormalities and incident stroke: the Atherosclerosis Risk in Communities Study. *The Lancet*, 358(9288):1134–1140, 2001. doi: 10.1016/S0140-6736(01)06253-5.

[9] T. Y. Wong. Is retinal photography useful in the measurement of stroke risk? *The Lancet Neurology*, 3(3):179–183, 2004. doi: 10.1016/S1474-4422(04)00682-9.

[10] R. Klein, A. R. Sharrett, B. E. Klein, L. E. Chambless, L. S. Cooper, L. D. Hubbard, and G. Evans. Are retinal arteriolar abnormalities related to atherosclerosis?: The Atherosclerosis Risk in Communities Study. *Arteriosclerosis, Thrombosis, and Vascular Biology*, 20(6):1644–1650, 2000. doi: 10.1161/01.ATV.20.6.1644.

[11] M. Araie and J. Kami. *Ocular Blood Flow in Disease: Other Diseases*, chapter 18, pages 429–432. Springer, Berlin, Heidelberg, 2012.

[12] Z. Chen and J. Zhang. Doppler optical coherence tomography. In Wolfgang Drexler and James G. Fujimoto, editors, *Optical Coherence Tomography: Technology and Applications*, pages 621–651. Springer, Berlin, Heidelberg, 2008. ISBN 978-3-540-77549-2.

[13] C. Riva, B. Ross, and G. B. Benedek. Laser Doppler measurements of blood flow in capillary tubes and retinal arteries. *Investigative Ophthalmology*, 11(11): 936–944, 1972. URL http://www.iovs.org/content/11/11/936.abstract.

[14] G. T. Feke and C. E. Riva. Laser Doppler measurements of blood velocity in human retinal vessels. *Journal of the Optical Society of America*, 68(4):526–531, 1978. doi: 10.1364/JOSA.68.000526.

[15] C. E. Riva, J. E. Grunwald, S. H. Sinclair, and K. O'Keefe. Fundus camera based retinal LDV. *Applied Optics*, 20(1):117–120, 1981. doi: 10.1364/AO.20.000117.

[16] G. T. Feke, D. G. Goger, H. Tagawa, and F. C. Delori. Laser Doppler technique for absolute measurement of blood speed in retinal vessels. *Biomedical Engineering, IEEE Transactions on*, BME-34(9):673–800, 1987. doi: 10.1109/TBME.1987.325992.

[17] J. B. Hickam and R. Frayser. A photographic method for measuring the mean retinal circulation time using fluorescein. *Investigative Ophthalmology*, 4(5): 876–884, 1965. URL http://www.iovs.org/content/4/5/876.abstract.

[18] S. S. Hayreh. Blood supply of the optic nerve head and its role in optic atrophy, glaucoma, and oedema of the optic disc. *British Journal of Ophthalmology*, 53 (11):721–748, 1969. doi: 10.1136/bjo.53.11.721.

[19] T. Koyama, N. Matsuo, K. Shimizu, M. Mihara, Y. Tsuchida, S. Wolf, and M. Reim. Retinal circulation times in quantitative fluorescein angiography. *Graefe's Archive for Clinical and Experimental Ophthalmology*, 228(5):442–446, 1990. doi: 10.1007/BF00927258.

[20] J.A. Izatt and M.A. Choma. Theory of optical coherence tomography. In Wolfgang Drexler and James G. Fujimoto, editors, *Optical Coherence Tomography: Technology and Applications*, pages 47–72. Springer, Berlin, Heidelberg, 2008. ISBN 978-3-540-77549-2.

[21] A. M. Davis. *Development of Fourier domain optical coherence tomography for applications in developmental biology.* Dissertation, Duke University, 2008. URL http://hdl.handle.net/10161/702.

[22] M. Wojtkowski, A. Kowalczyk, R. Leitgeb, and A. F. Fercher. Full range complex spectral optical coherence tomography technique in eye imaging. *Optics Letters*, 27(16):1415–1417, 2002. doi: 10.1364/OL.27.001415.

[23] R. Leitgeb, L. Schmetterer, W. Drexler, A. Fercher, R. Zawadzki, and T. Bajraszewski. Real-time assessment of retinal blood flow with ultrafast acquisition by color Doppler Fourier domain optical coherence tomography. *Optics Express*, 11(23):3116–3121, 2003. doi: 10.1364/OE.11.003116.

[24] R. Werkmeister. *Dual-beam Bidirectional Doppler Fourier-Domain Optical Coherence Tomography.* Dissertation, Medical University of Vienna, 2010. URL http://media.obvsg.at/AC07809304.

[25] C. E. Riva, G. T. Feke, B. Eberli, and V. Benary. Bidirectional LDV system for absolute measurement of blood speed in retinal vessels. *Applied Optics*, 18 (13):2301–2306, 1979. doi: 10.1364/AO.18.002301.

[26] T. Schmoll, C. Kolbitsch, and R. A. Leitgeb. Ultra-high-speed volumetric tomography of human retinal blood flow. *Optics Express*, 17(5):4166–4176, 2009. doi: 10.1364/OE.17.004166.

[27] E. Koch, J. Walther, and M. Cuevas. Limits of Fourier domain Doppler-OCT at high velocities. *Sensors and Actuators A: Physical*, 156(1):8–13, 2009. doi: 10.1016/j.sna.2009.01.022.

[28] G. Aschinger, R. Werkmeister, V. Doblhoff-Dier, R. Leitgeb, G. Garhöfer, M. Gröschl, and L. Schmetterer. Blood flow velocity vector field reconstruction from dual-beam bi-directional Doppler OCT measurements in retinal veins. Manuscript in preparation, 2014.

[29] M. Pircher, C. K. Hitzenberger, and U. Schmidt-Erfurth. Polarization sensitive optical coherence tomography in the human eye. *Progress in retinal and eye research*, 30(6):431–451, 2011. doi: 10.1016/j.preteyes.2011.06.003.

[30] T. Torzicky, S. Marschall, M. Pircher, B. Baumann, M. Bonesi, S. Zotter, E. Gotzinger, W. Trasischker, T. Klein, W. Wieser, B. Biedermann, R. Huber, P. Andersen, and C. K. Hitzenberger. Retinal polarization-sensitive optical coherence tomography at 1060 nm with 350 kHz A-scan rate using a Fourier

domain mode locked laser. *Journal of Biomedical Optics*, 18(2):026008, 2013. doi: 10.1117/1.JBO.18.2.026008.

[31] S. W. Lee, H. W. Jeong, B. M. Kim, Y. C. Ahn, W. Jung, and Z. Chen. Optimization for axial resolution, depth range, and sensitivity of spectral domain optical coherence tomography at 1.3 μm. *Journal of Korean Physical Society*, 55(6):2354–2360, 2009. doi: 10.3938/jkps.55.2354.

[32] J.G. Fujimoto and W. Drexler. Introduction to optical coherence tomography. In Wolfgang Drexler and James G. Fujimoto, editors, *Optical Coherence Tomography: Technology and Applications*, pages 1–45. Springer, Berlin, Heidelberg, 2008. ISBN 978-3-540-77549-2.

[33] K. Iizuka. *Elements of Photonics*, volume 1: In Free Space and Special Media. John Wiley and Sons, New York, 2002. ISBN 0-471-83938-8.

[34] R. A. Leitgeb, R. M. Werkmeister, C. Blatter, and L. Schmetterer. Doppler optical coherence tomography. *Progress in Retinal and Eye Research*, 41:26–43, 2014. doi: 10.1016/j.preteyeres.2014.03.004.

[35] A. S. Singh, T. Schmoll, and R. A. Leitgeb. Segmentation of Doppler optical coherence tomography signatures using a support-vector machine. *Biomedical Optics Express*, 2(5):1328–1339, 2011. doi: 10.1364/BOE.2.001328.

[36] B. Park, M. C. Pierce, B. Cense, S. H. Yun, M. Mujat, G. Tearney, B. Bouma, and J. de Boer. Real-time fiber-based multi-functional spectral-domain optical coherence tomography at 1.3 μm. *Optics Express*, 13(11):3931–3944, 2005. doi: 10.1364/OPEX.13.003931.

[37] A. R. Pries and T. W. Secomb. *Microcirculation*, chapter Blood Flow in Microvascular Networks, pages 3–36. Handbook of Physiology. Elsevier, Academic Press, Amsterdam, London, 2nd edition, 2008. ISBN 978-0-12-374530-9.

[38] C. E. Riva, J. E. Grunwald, S. H. Sinclair, and B. L. Petrig. Blood velocity and volumetric flow rate in human retinal vessels. *Investigative Ophthalmology and Visual Science*, 26(8):1124–1132, 1985. URL `http://www.iovs.org/content/26/8/1124.abstract`.

[39] G. T. Feke, H. Tagawa, D. M. Deupree, D. G. Goger, J. Sebag, and J. J. Weiter. Blood flow in the normal human retina. *Investigative Ophthalmology and Visual Science*, 30(1):58–65, 1989. URL `http://www.iovs.org/content/30/1/58.abstract`.

[40] J. E. Grunwald, J. DuPont, and C. E. Riva. Retinal haemodynamics in patients with early diabetes mellitus. *British Journal of Ophthalmology*, 80(4):327–331, 1996. doi: 10.1136/bjo.80.4.327.

[41] G. Garhöfer, T. Bek, A. G. Boehm, D. Gherghel, J. Grunwald, P. Jeppesen, H. Kergoat, K. Kotliar, I. Lanzl, J. V. Lovasik, E. Nagel, W. Vilser, S. Orgul, and L. Schmetterer. Use of the retinal vessel analyzer in ocular blood flow research. *Acta Ophthalmologica*, 88(7):717–722, 2010. doi: 10.1111/j.1755-3768.2009.01587.x.

[42] A. Gullstrand. *The dioptrics of the eye*, volume 1, pages 351–352. Optical Society of America, 1924.

[43] C. J. Pedersen, D. Huang, M. A. Shure, and A. M. Rollins. Measurement of absolute flow velocity vector using dual-angle, delay-encoded Doppler optical coherence tomography. *Optics Letters*, 32(5):506–508, 2007. doi: 10.1364/OL.32.000506.

[44] Y. C. Ahn, W. Jung, and Z. Chen. Quantification of a three-dimensional velocity vector using spectral-domain Doppler optical coherence tomography. *Optics Letters*, 32(11):1587–1589, 2007. doi: 10.1364/OL.32.001587.

[45] Y. Wang, B. A. Bower, J. A. Izatt, O. Tan, and D. Huang. Retinal blood flow measurement by circumpapillary Fourier domain Doppler optical coherence tomography. *Journal of Biomedical Optics*, 13(6):064003, 2008. doi: 10.1117/1.2998480.

[46] Y. Wang, A. Lu, J. Gil-Flamer, O. Tan, J. A. Izatt, and D. Huang. Measurement of total blood flow in the normal human retina using Doppler Fourier-domain optical coherence tomography. *British Journal of Ophthalmology*, 93(5):634–637, 2009. doi: 10.1136/bjo.2008.150276.

[47] Y. Wang, A. A. Fawzi, R. Varma, A. A. Sadun, X. Zhang, O. Tan, J. A. Izatt, and D. Huang. Pilot study of optical coherence tomography measurement of retinal blood flow in retinal and optic nerve diseases. *Investigative Ophthalmology and Visual Science*, 52(2):840–845, 2011. doi: 10.1167/iovs.10-5985.

[48] B. Baumann, B. Potsaid, M. F. Kraus, J. J. Liu, D. Huang, J. Hornegger, A. E. Cable, J. S. Duker, and J. G. Fujimoto. Total retinal blood flow measurement with ultrahigh speed swept source/Fourier domain OCT. *Biomedical Optics Express*, 2(6):1539–1552, 2011. doi: 10.1364/BOE.2.001539.

[49] C. Blatter, S. Coquoz, B. Grajciar, A. S. G. Singh, M. Bonesi, R. M. Werkmeister, L. Schmetterer, and R. A. Leitgeb. Dove prism based rotating dual beam bidirectional Doppler OCT. *Biomedical Optics Express*, 4(7):1188–1203, 2013. doi: 10.1364/BOE.4.001188.

[50] W. Trasischker, R. M. Werkmeister, S. Zotter, B. Baumann, T. Torzicky, M. Pircher, and C. K. Hitzenberger. In vitro and in vivo three-dimensional velocity vector measurement by three-beam spectral-domain Doppler optical

coherence tomography. *Journal of Biomedical Optics*, 18(11):116010, 2013. doi: 10.1117/1.JBO.18.11.116010.

[51] H. Gray. *Gray's Anatomy*. Lea and Febiger, Philadelphia, 20th edition, 1918. URL `http://www.bartleby.com/107/illus882.html`.

[52] A. Despopoulos and S. Silbernagl. *Color Atlas of Physiology*. Thieme, New York, 5th edition edition, 2003. ISBN 1-58890-061-4.

[53] International Electrotechnical Commission. Safety of laser products - part 1: Equipment classification and requirements, 2006.

[54] C. Dai, X. Liu, H. F. Zhang, C. A. Puliafito, and S. Jiao. Absolute retinal blood flow measurement with a dual-beam Doppler optical coherence tomography. *Investigative Ophthalmology and Visual Science*, 54(13):7998–8003, 2013. doi: 10.1167/iovs.13-12318.

[55] M. Wojtkowski, V. Srinivasan, T. Ko, J. Fujimoto, A. Kowalczyk, and J. Duker. Ultrahigh-resolution, high-speed, Fourier domain optical coherence tomography and methods for dispersion compensation. *Optics Express*, 12(11):2404–2422, 2004. doi: 10.1364/OPEX.12.002404.

[56] M. L. Turgeon. *Clinical Hematology: Theory and Procedures*. Lippincott Williams and Wilkins, 4th edition edition, 2005. ISBN 0-7817-5007-5.

[57] S. Makita, Y. Hong, M. Yamanari, T. Yatagai, and Y. Yasuno. Optical coherence angiography. *Optics Express*, 14(17):7821–7840, 2006. doi: 10.1364/OE.14.007821.

[58] R. M. Werkmeister, N. Dragostinoff, S. Palkovits, R. Told, A. Boltz, R. A. Leitgeb, M. Gröschl, G. Garhöfer, and L. Schmetterer. Measurement of absolute blood flow velocity and blood flow in the human retina by dual-beam bidirectional Doppler Fourier-domain optical coherence tomography. *Investigative Ophthalmology and Visual Science*, 53(10):6062–6071, 2012. doi: 10.1167/iovs.12-9514.

[59] D. N. Damon and B. R. Duling. A comparison between mean blood velocities and center-line red cell velocities as measured with a mechanical image streaking velocitometer. *Microvascular Research*, 17(3):330–332, 1979. doi: 10.1016/S0026-2862(79)80008-4.

[60] S. M. Rassam, V. Patel, H. C. Chen, and E. M. Kohner. Regional retinal blood flow and vascular autoregulation. *Eye*, 10(3):331–337, 1996. doi: 10.1038/eye.1996.69.

[61] J. P. Garcia, Jr., P. T. Garcia, and R. B. Rosen. Retinal blood flow in the normal human eye using the Canon Laser Blood Flowmeter. *Ophthalmic Research*, 34 (5):295–299, 2002. doi: 10.1159/000065600.

[62] G. Garhöfer, R. Werkmeister, N. Dragostinoff, and L. Schmetterer. Retinal blood flow in healthy young subjects. *Investigative Ophthalmology and Visual Science*, 53(2):698–703, 2012. doi: 10.1167/iovs.11-8624.

[63] E. Polska, K. Kircher, P. Ehrlich, P. V. Vecsei, and L. Schmetterer. RI in central retinal artery as assessed by CDI does not correspond to retinal vascular resistance. *American Journal of Physiology - Heart and Circulatory Physiology*, 280 (4):H1442–H1147, 2001. URL `http://ajpheart.physiology.org/content/280/4/H1442`.

[64] B. C. Eu. Generalization of the Hagen-Poiseuille velocity profile to non-Newtonian fluids and measurement of their viscosity. *American Journal of Physics*, 58(1):83–84, 1990. doi: 10.1119/1.16328.

[65] C. D. Murray. The physiological principle of minimum work: I. The vascular system and the cost of blood volume. *Proceedings of the National Academy of Sciences of the United States of America*, 12(3):207–214, 1926. URL `http://www.pnas.org/content/12/3/207.full.pdf+html`.

[66] R. Fåhræus and T. Lindqvist. The viscosity of the blood in narrow capillary tubes. *The American Journal of Physiology*, 96:562–568, 1931. URL `http://ajplegacy.physiology.org/content/96/3/562`.

[67] T. W. Secomb and A. R. Pries. Blood viscosity in microvessels: Experiment and theory. *Comptes Rendus Physique*, 14(6):470–478, 2013. doi: 10.1016/j.crhy.2013.04.002.

[68] B. Baumann. Spektrale optische Kohärenztomographie bei 1310 nm. Master thesis, University of Vienna, 2006. URL `http://ubdata.univie.ac.at/AC05256473`.

[69] P. T. Boggs and J. E. Rogers. The computation and use of the asymptotic covariance matrix for measurement error models. Technical Report NISTIR 89—4102, National Institute of Standards and Technology, 1990.

[70] G. A. F. Seber and C. J. Wild. *Nonlinear Regression.* John Wiley and Sons, Hoboken, New Jersey, 2003. ISBN 0-471-47135-6.

Veronika Doblhoff-Dier

Curriculum vitae

Jägerstraße 69/1/12, 1200 Vienna, Austria
v.doblhoff@gmail.com
+43 (0)676 325 93 38

Personal data

Date of birth	**11 February, 1985**.
Place of birth	**Vienna, Austria**.
Citizenship	**Austrian**.

Education

10/2010 to date	**Doctoral Programme in Technical Sciences**, *Vienna University of Technology, Vienna, Austria*. Topic: A technique to measure total retinal blood flow based on Fourier-domain optical coherence tomography and fundus imaging.
11/2014	**LabVIEW Certified Associate Developer**.
09/2008 – 10/2013	**Master of Education for physics and English**, *Vienna University of Technology, Vienna, Austria and University of Vienna, Vienna, Austria*. Both diploma exams passed with distinction.
09/2003 – 06/2008	**Master Programme Technical Physics**, *Vienna University of Technology, Vienna, Austria*. Diploma thesis: Corrosion pits and influence of environment on fatigue crack growth in steam turbine steel. All diploma exams passed with distinction.
02/2007 – 07/2007	**Exchange semester**, *École Polytechnique Fédérale de Lausanne, Lausanne, Switzerland*. Key area of training: Biophysics
06/2003	**A-levels**, *GRG19 Billrothgymnasium, Vienna, Austria*. A-levels exams passed with distinction.
03/2001 – 06/2001	**Exchange term**, *Wakefield Girls High School, Wakefield, United Kingdom*.

Professional experience

10/2010 to date	**Project assistant**, *Medical University of Vienna, Vienna, Austria.* Development of a dual beam Fourier-domain optical coherence tomography system to measure the total retinal blood flow.
10/2009 – 06/2010	**Scientific assistant**, *University of Natural Resources and Life Sciences, Vienna, Austria.* Laura Bassi Projekt BRIC (BioResorbable Implants for Children): wettability measurements, tensile testing, and fatigue testing
09/2007 – 07/2008	**Intern**, *Institute of Sensor- and Actuator-Systems, Vienna University of Technology, Vienna, Austria.* Development of a Braille-pad for teaching geometry in schools for the blind.
09/2003	**Intern**, *Zentralanstalt für Meteorologie und Geodynamik (Institute for meteorology and geodynamics), Vienna, Austria.*

Teaching

09/2014 to date	**High school teacher for Physics and English**, *BRG18 Schopenhauerstraße and BG18 Klostergasse, Vienna, Austria.*
09/2008 – 01/2009	**High school teacher for Physics**, *GRG19 Billrothgymnasium, Vienna, Austria.*
09/2007 – 07/2008	**Tutor**, *Institute of Solid State Physics, Vienna University of Technology, Vienna, Austria.* Fundamentals of Physics I and II (exercises).

Prizes and Awards

08/2014	**Talente@Alpbach awardee**, *Scholarship for the Technology Symposium at the European Forum Alpbach.*
09/2007 – 06/2008	**TUtheTop awardee**, *High excellency program Vienna University of Technology.*
06/2008	**EBC*L Champions League**, *European Business Competence Licence.* National competition: 1st prize; international competition: 7th prize.
09/2006 – 06/2008	**Achievement scholarship**, *Vienna University of Technology.*

Publications and Conference Contributions

Papers in peer-reviewed journals

V. Doblhoff-Dier, L. Schmetterer, W. Vilser, G. Garhöfer, M. Gröschl, R. A. Leitgeb, and R. M. Werkmeister. Measurement of the total retinal blood flow using dual beam Fourier-domain Doppler optical coherence tomography with orthogonal detection planes. *Biomedical Optics Express*, 5(2):630–642, 2014. doi: 10.1364/BOE.5.000630.

G. Aschinger, R. M. Werkmeister, V. Doblhoff-Dier, R. Leitgeb, G. Garhöfer, M. Gröschl, and L. Schmetterer. Blood flow velocity vector field reconstruction from dual-beam bi-directional Doppler OCT measurements in retinal veins. Manuscript in preparation, 2014.

E. K. Tschegg, R. A. Lindtner, V. Doblhoff-Dier, S. E. Stanzl-Tschegg, G. Holzlechner, C. Castellani, T. Imwinkelried, and A. Weinberg. Characterization methods of bone-implant-interfaces of bioresorbable and titanium implants by fracture mechanical means. *J Mech Behav Biomed Mater*, 4(5):766–775, 2011. doi: 10.1016/j.jmbbm.2010.08.004.

Conference contributions

V. Doblhoff-Dier, R. M. Werkmeister, G. Aschinger, and L. Schmetterer. Determination of the total retinal blood flow with a dual-beam Doppler Fourier-domain optical coherence tomograph and an integrated Dynamic Vessel Analyser, 2014. Poster at the 10th YSA PhD Symposium.

G. Aschinger, R. M. Werkmeister, V. Doblhoff-Dier, and L. Schmetterer. Blood flow profiles in vivo in retinal vessels acquired via Doppler FD-OCT, 2014. Poster at the 10th YSA PhD Symposium.

V. Doblhoff-Dier, G. Aschinger, L. Schmetterer, W. Vilser, and R. M. Werkmeister. Acquisition of the total retinal blood flow with a dual-beam FD-OCT system and an integrated Dynamic Vessel Analyser, 2014. Poster at the ARVO 2014 Annual meeting.

G. Aschinger, R. M. Werkmeister, V. Doblhoff-Dier, and L. Schmetterer. Blood flow profiles in vivo in retinal vessels acquired via Doppler FD-OCT, 2014. Poster at the ARVO 2014 Annual meeting.

V. Doblhoff-Dier, R. M. Werkmeister, M. Gröschl, and L. Schmetterer. Dual beam Doppler FD-OCT system with integrated Dynamic Vessel Analyzer and rotatable beams to measure total retinal blood flow, 2014. Talk at the 2014 Photonics West BiOS Conference.

V. Doblhoff-Dier, A. Celarek, C. Castellani, E. K. Tschegg, S. E. Stanzl-Tschegg, and A.-M. Weinberg. Bioresorbable implants for children, 2010. Poster at the 2010 Strategic Workshop on Principles and Development of Bio-Inspired Materials.

Castellani C., R. Lindtner, V. Doblhoff-Dier, Tschegg E. K., Stanzl-Tschegg S. E., and Weinberg A.-M. Magnesium-alloy: a novel approach to biodegradable implants, 2009. Talk at the 3rd International Conference on Mechanics of Biomaterials and Tissues.

Proceedings

V. Doblhoff-Dier, G. Aschinger, L. Schmetterer, W. Vilser, and R. M. Werkmeister. Acquisition of the total retinal blood flow with a dual-beam FD-OCT system and an integrated dynamic vessel analyser. *Investigative Ophthalmology and Visual Science*, 55: E–Abstract 4320, 2014. URL `http://abstracts.iovs.org/cgi/content/abstract/55/5/4320`.

G. Aschinger, R. M. Werkmeister, V. Doblhoff-Dier, and L. Schmetterer. Blood flow profiles in vivo in retinal vessels acquired via Doppler FD-OCT. *Investigative Ophthalmology and Visual Science*, 55: E–Abstract 4327, 2014. URL `http://abstracts.iovs.org/cgi/content/abstract/55/5/4327`.

V. Doblhoff-Dier, R. M. Werkmeister, M. Gröschl, and L. Schmetterer. Dual beam Doppler FD-OCT system with integrated Dynamic Vessel Analyzer and rotatable beams to measure total retinal blood flow. In J. A. Izatt, J. G. Fujimoto, and V. V. Tuchin, editors, *Optical Coherence Tomography and Coherence Domain Optical Methods in Biomedicine XVIII*, volume 8934 of *SPIE Proceedings*, 2014. doi: 10.1117/12.2039561.

V. Doblhoff-Dier, A. Celarek, C. Castellani, E. Tschegg, S. E. Stanzl-Tschegg, and A.-M. Weinberg. Bioresorbable implants for children. In S. E. Stanzl-Tschegg and R. Seidel, editors, *Principles and Development of Bio-inspired Materials*, Proceedings of the COST Strategic Workshop, pages 112–113. University of Natural Resources and Applied Life Sciences, 2010. URL `https://www.map.boku.ac.at/fileadmin/data/H03000/H89000/H89200/Bio-Inspired_Materials/Booklet_BioInspired_Materials_BOKU.pdf`.